

ANGULAR MOMENTUM AND GALAXY FORMATION REVISITED

AARON J. ROMANOWSKY¹, S. MICHAEL FALL²

¹University of California Observatories, Santa Cruz, CA 95064, USA

²Space Telescope Science Institute, 3700 San Martin Drive, Baltimore, MD 21218, USA

The Astrophysical Journal Supplement Series, in press, 17 July 2012

ABSTRACT

Motivated by a new wave of kinematical tracers in the outer regions of early-type galaxies (ellipticals and lenticulars), we re-examine the role of angular momentum in galaxies of all types. We present new methods for quantifying the specific angular momentum j , focusing mainly on the more challenging case of early-type galaxies, in order to derive firm empirical relations between stellar j_* and mass M_* (thus extending the work by Fall 1983). We carry out detailed analyses of eight galaxies with kinematical data extending as far out as ten effective radii, and find that data at two effective radii are generally sufficient to estimate total j_* reliably. Our results contravene suggestions that ellipticals could harbor large reservoirs of hidden j_* in their outer regions owing to angular momentum transport in major mergers. We then carry out a comprehensive analysis of extended kinematic data from the literature for a sample of ~ 100 nearby bright galaxies of all types, placing them on a diagram of j_* versus M_* . The ellipticals and spirals form two parallel j_*-M_* tracks, with log-slopes of ~ 0.6 , which for the spirals is closely related to the Tully-Fisher relation, but for the ellipticals derives from a remarkable conspiracy between masses, sizes, and rotation velocities. We find that on average, the ellipticals contain roughly 3–4 times less angular momentum than spirals of equal mass. We decompose the spirals into disks and bulges and find that these subcomponents follow similar j_*-M_* trends to the overall ones for spirals and ellipticals. The lenticulars have an intermediate trend, and we propose that the morphological types of galaxies reflect disk and bulge subcomponents that follow separate, fundamental j_*-M_* scaling relations. This provides a physical motivation for characterizing galaxies most basically with two parameters: mass and bulge-to-disk ratio. Next, in an approach complementary to numerical simulations, we construct idealized models of angular momentum content in a cosmological context, using estimates of dark matter halo spin and mass from theoretical and empirical studies. We find that the width of the halo spin distribution cannot account for the differences between spiral and elliptical j_* , but that the observations are reproduced well if these galaxies simply retained different fractions of their initial j complement ($\sim 60\%$ and $\sim 10\%$, respectively). We consider various physical mechanisms for the simultaneous evolution of j_* and M_* (including outflows, stripping, collapse bias, and merging), emphasizing that the vector sum of all such processes must produce the observed j_*-M_* relations. We suggest that a combination of early collapse and multiple mergers (major or minor) may account naturally for the trend for ellipticals. More generally, the observed variations in angular momentum represent simple but fundamental constraints for any model of galaxy formation.

1. INTRODUCTION

Many schemes for classifying galaxies have been presented over the years, focusing on somewhat ephemeral properties such as morphology and color. Alternatively, one may consider three fundamental physical parameters: mass M , energy E , and angular momentum J . Qualitatively, these are related to the amount of material in a galaxy, to the linear size, and to the rotation velocity.

An important advantage of these parameters is that they may be related back to the earlier states of galaxies without having to unravel all of the messy intervening details such as baryonic dissipation, star formation, and morphological transformation. As an example, the simple assumption that J is approximately conserved during the collapse of gas within hierarchically-forming dark matter halos naturally explains the observed basic scaling relations of disk galaxies (Fall & Efstathiou 1980; Dalcanton et al. 1997; Mo et al. 1998).

Here “conserved” means that the initial J_* is retained at a factor of ~ 2 level, unlike E , which can

be readily lost by factors of ~ 10 through dissipative collapse and radiation. Note that the “weak” conservation of *total* J is less restrictive and more plausible than the “strong” conservation of the *internal* distribution of J with radius, which could be readily altered by secular processes within disks while still preserving total J (e.g., Kormendy & Kennicutt 2004; see Fall 2002 and Freeman & Bland-Hawthorn 2002 for further discussion).

In this vein, Fall (1983, hereafter F83) introduced a general diagram of j_* versus stellar mass M_* , where $j_* \equiv J_*/M_*$ is the stellar specific angular momentum. This diagram has the important advantages that it deals with conservable physical quantities, and that the axes represent independent variables. The M_* axis embodies a *mass* scale, while the j_* axis represents a *length* scale times a *rotation-velocity* scale. On the contrary, the standard relations between M_* and circular velocity v_c (e.g., Tully & Fisher 1977; Dutton et al. 2010; Trujillo-Gomez et al. 2011) involve correlated variables, since v_c may be directly connected to M_* . Another re-

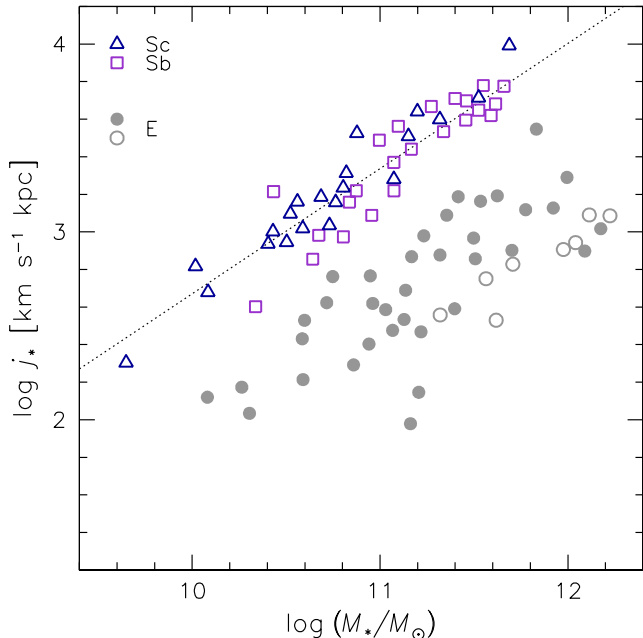


FIG. 1.— The total intrinsic stellar specific angular momentum of galaxies plotted against their total stellar mass, reproduced from Fall (1983), with corrections from a Hubble constant of $h = 0.5$ to 0.7 . The symbols show galaxy types according to the legend at the upper left; for the ellipticals (E), open circles show galaxies with an upper-limit estimate of j_* . The dotted line shows a trend of $j_* \propto M_*^{2/3}$. The logarithms plotted here and used throughout the paper are in base 10. These j_*-M_* scaling relations are the focus of this paper, and will eventually be updated in Figure 14.

lated parameter is the *spin* (λ), which is useful for characterizing dark matter halo rotation, and which we will discuss later in this paper.

The simple j_*-M_* diagram is still charged with useful information for understanding galaxies, and to orient the remainder of our discussion, we begin by reproducing the original version from F83 here in Figure 1. The only change is to rescale the data for a Hubble constant of $h = 0.7$ rather than $h = 0.5$. These data were for late-type spirals (Sb and Sc) based on extended optical rotation curves, and for elliptical galaxies based on observations from their inner half-light radii, as feasible in that era.

The first key feature to note from Figure 1 is that the spirals follow a fairly tight scaling relation of $j_* \propto M_*^\alpha$, where $\alpha \sim 0.7$ (see also Takase & Kinoshita 1967; Heidemann 1969; Freeman 1970; Nordsieck 1973), which is a phenomenology that is now understood to provide a remarkable link between visible galaxies and their invisible dark matter halos. F83 provided a simple theoretical framework in which the gaseous baryons of galaxies are initially mixed with the dark matter and share in the same j . The baryons then cool and decouple from the dark matter, collapsing into star-forming disks. If the baryonic j is approximately conserved in this process, both the *zeropoint* and the *slope* of the observed spiral-galaxy j_*-M_* relation are reproduced.

The formation of disk galaxies can thus be explained at a basic level through this long-standing picture of (weak) j conservation. To provide further understanding, hydrodynamical simulations of galaxy formation have been pursued for decades, with the j_*-M_* obser-

vational diagram from F83 as a key benchmark for the theory. Attaining that benchmark has turned out to be a major challenge, with early studies finding catastrophic j loss (e.g., Katz & Gunn 1991; Navarro & Benz 1991; Navarro et al. 1995; Navarro & Steinmetz 1997).

This angular momentum “catastrophe” can be attributed partially to numerical limitations, and partially to uncertainties in modeling baryonic processes such as feedback following star formation, as reviewed by Fall (2002). Over the years, the simulations have improved and can now come close to reproducing the j_*-M_* observations (e.g., Governato et al. 2007; Agertz et al. 2011; Guedes et al. 2011), although much work still remains in understanding both the numerics and the physics.

Besides the angular momentum benchmark from F83 which has become a standard ingredient in modeling the formation of disk galaxies, there is another aspect of the original j_*-M_* diagram that has received relatively little attention: the inclusion of elliptical galaxies along with the spirals. The diagram thereby provides a fundamental diagnostic of scaling relations for *all* galaxies, which is important because there is still not a full explanation for such a basic property as the Hubble (1926) sequence of galaxy morphologies.

Star formation considerations aside, there is an obvious *dynamical* distinction between galaxy disks and spheroids, which are characterized by cold, ordered rotation versus random motions with fairly low net rotation, respectively. Differences in the conservation and distribution of j may very well be pivotal to explaining these differences and to governing the fates of galaxies.

As shown in Figure 1, F83 found that ellipticals followed a j_*-M_* trend roughly parallel to the spirals, but lower by a factor of ~ 6 , and with more apparent scatter (see also Bertola & Capaccioli 1975). There are several potential explanations for such a difference between spirals and ellipticals, but the most plausible one is traced to a violent, clumpy genesis for spheroids. For example, mergers could naturally redistribute angular momentum from the central regions of a galaxy to its outer parts by dynamical friction (e.g., Aarseth & Fall 1980; Gerhard 1981; Barnes & Efstathiou 1987; Zurek et al. 1988; Barnes 1992; Hernquist 1992; Navarro & White 1994; Heyl et al. 1996; D’Onghia & Navarro 2007; Zavala et al. 2008). Thus, j should be basically conserved but inconveniently locked up in unobservable components such as the dark halo and the faint outer stars.

With this theoretical sketch in hand, the j_* disparity between spirals and ellipticals has received little further attention over the years. However, the scenario of angular momentum redistribution has not yet been directly tested by observations—a situation that may now finally be remedied via the advent of new techniques for optical spectroscopy in galaxy halos (with preliminary results along these lines reported in Romanowsky et al. 2004).

In this paper we re-open various questions about angular momentum in all types of bright galaxies, following and extending the treatment of F83. Are the j_*-M_* slopes, zeropoints, and scatter in Figure 1 supported upon re-examination? Does the “missing” j_* in ellipticals emerge in large-radius data? Can the j_* variations be associated with the natural dispersion in spin expected for standard dark matter halos, or is it necessary to invoke

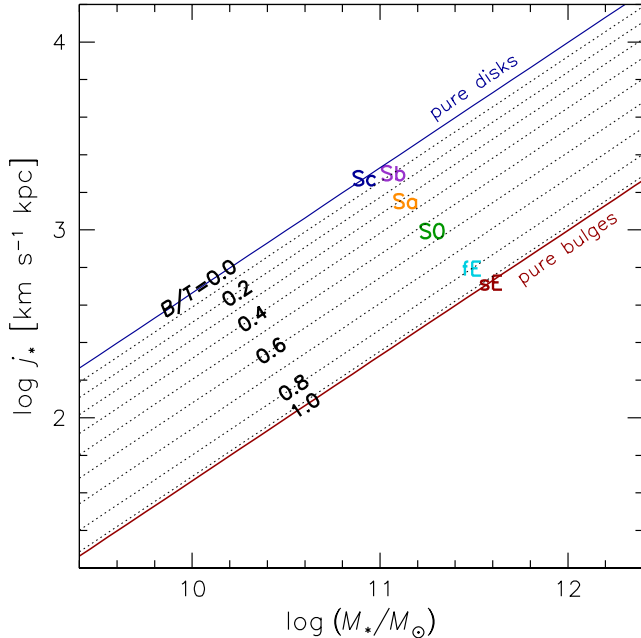


FIG. 2.— Physically-motivated classification diagram of galaxies, using the parameter space of stellar mass and specific angular momentum. The solid blue and red lines show parallel scaling relations for disks and bulges, which are based loosely on our observational results to be presented in Section 5. Approximate positions are also shown for different galaxy types: Sc, Sb, Sa, S0, fE, and sE (the latter two being fast and slow-rotating ellipticals).

additional baryonic j evolution?

F83 also proposed that the Hubble sequence may be understood as a systematic variation in j_* at a fixed M_* (or equivalently, variation in M_* at fixed j_*), but could not test this idea owing to the lack of adequate data for the crucial, intermediate cases of Sa and S0 galaxies. Here we will pursue this theme, and advance a framework where every galaxy can be considered basically as a linear combination of a disk and a bulge, with each of these components following a characteristic j_*-M_* scaling relation. In this idealized model, the j_*-M_* parameter space maps uniquely to a space of M_* and bulge fraction B/T .

Figure 2 provides a schematic overview of this framework, showing decompositions of the Hubble sequence in j_*-M_* parameter space. One of our goals in this paper will be to include observational results for Sa and S0 galaxies in this diagram for the first time, to see if such systems fill in the gap (if any) between earlier and later types, and if bulges and disks are homologous enough to explain the j_*-M_* trends as primarily reflecting a B/T sequence.

The j_*-M_* diagram does not simply provide a basic *description* of galaxies and their subcomponents, but also permits a novel approach to modeling the *evolution* of galaxies which is complementary to numerical simulations. As mentioned previously, there are simple models for the formation of disk galaxies that relate their j_* and M_* values to the initial conditions of their host halos. More generally, *any* stage in the evolution of a galaxy will involve a vector of change in the $j-M$ diagram that is not arbitrary, since in real physical processes, changes in j and M will be linked in characteristic ways. There-

fore the empirical offsets between the j_*-M_* sequences of different galaxy types, and of their subcomponents including bulges, disks, and dark matter halos, can reveal the evolutionary connections among them.

We set out to explore the preceding questions and issues as follows. In Section 2 we present a methodology for careful estimation of j_* in various types of galaxies and observations, with most of the details of its derivation given in Appendix A. Section 3 uses detailed models of a handful of real galaxies to examine a simplified procedure for j_* estimation. Our updated analysis of the observed j_* trends in a large sample of galaxies follows, with the observational ingredients and their inter-correlations described in Section 4, and the full results presented in Section 5 including a definitive confirmation of the large offset between spirals and ellipticals. These empirical j_* trends can be considered as fundamental, enduring tools for constraining theories of galaxy evolution. In Section 6 we go on to connect the observations to generalized theoretical predictions for angular momentum in a modern cosmological context. We summarize in Section 7.

In addition, Appendix A is an important part of this paper, providing an extended presentation of new content relating to the derivation of j_* , which has been split off from the main text for the sake of readability. Appendices B–D provide data tables of j_* and other properties of observed galaxies, along with detailed discussion of the observations and data analysis for a subsample of these galaxies.

The reader looking for immediate answers to the questions above may wish to skip ahead to the results of Sections 5.2 and onwards.

2. BASIC FORMULAE: DISKS AND SPHEROIDS

The foundation for this paper is a revised, general observational analysis of specific stellar angular momentum j_* for bright galaxies in the nearby universe. This quantity is most generally calculated by the following expression:

$$\mathbf{j}_t \equiv \frac{\mathbf{J}_t}{M_*} = \frac{\int_{\mathbf{r}} \mathbf{r} \times \bar{\mathbf{v}} \rho d^3\mathbf{r}}{\int_{\mathbf{r}} \rho d^3\mathbf{r}}, \quad (1)$$

where the subscript “t” denotes the “true” angular momentum in three-dimensional space, \mathbf{r} and $\bar{\mathbf{v}}(\mathbf{r})$ are the position and mean-velocity vectors (with respect to the center of mass of the galaxy), and $\rho(\mathbf{r})$ is the three-dimensional density of the population under study (generally assumed to be stars in this project).

For spiral galaxies, we approximate the density distribution as an infinitely-thin, axisymmetric disk with an exponential surface density profile. Assuming also a radially-constant rotation curve, Equation (1) yields the simple expression:

$$\dot{j}_t = 2 v_c R_d, \quad (2)$$

where v_c is the intrinsic circular rotation velocity, and R_d is the intrinsic exponential-disk scale length. These de-projected quantities are relatively easy to infer from observations because it is straightforward to estimate disk galaxy inclinations. Equation (2) is widely used in the literature (including in F83), but we will demonstrate explicitly that it provides an excellent approximation to real galaxies whose rotation curves vary with radius.

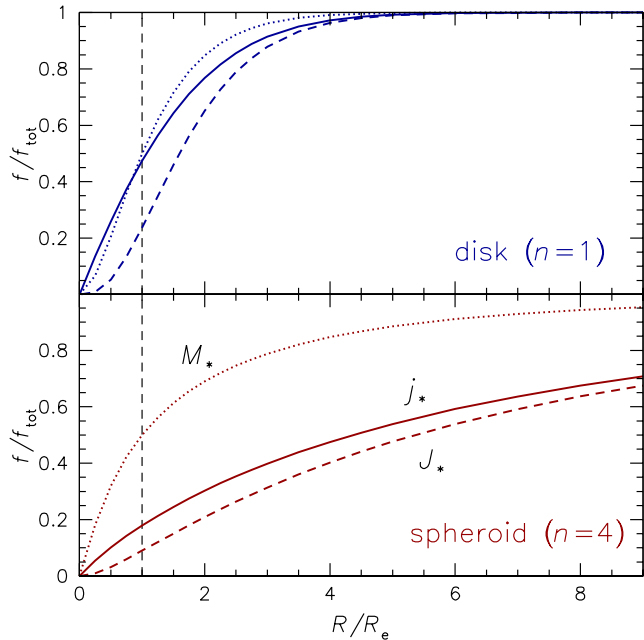


FIG. 3.— Fraction of enclosed cumulative quantities vs. cylindrical galactocentric radius (normalized by the effective radius R_e) for model galaxies with an exponential profile ($n = 1$ disk, *top*) and a de Vaucouleurs profile ($n = 4$ spheroid, *bottom*). A constant, cylindrical rotation field is assumed. The quantities are projected stellar mass M_* (*dotted curve*), angular momentum J_* (*dashed*), and specific angular momentum j_* (*solid*). The latter quantity is computed using the cumulative values of both J_* and M_* within the radius R . The vertical dashed line marks $1 R_e$. To capture half of j_* , the observations must extend to $\sim 1 R_e$ in a disk galaxy, and to $\sim (4\text{--}5) R_e$ in a spheroid.

For more general cases including elliptical galaxies,¹ there is no established recipe equivalent to Equation (2). For multiple reasons, estimating j_t for these galaxies is much harder than for spirals. Not only are their inclinations and intrinsic shapes uncertain, but large-radius rotation measurements are both more difficult and more critical.

We illustrate the last point with some basic galaxy models. Adopting the simple assumption of an axisymmetric system with cylindrical rotation that is constant with respect to the intrinsic radius R , we consider both a disk galaxy with an exponential surface density profile, and an elliptical galaxy with a standard de Vaucouleurs (1948) $R^{1/4}$ profile. Although ellipticals are in general triaxial systems, the axisymmetric model is sufficiently accurate for our purposes.

Figure 3 then shows the cumulative distribution of angular momentum (both total and specific) with radius. For the disk galaxy, the specific angular momentum reaches roughly half of its total value at the effective radius R_e that encloses half of the stellar light. This implies that observational estimates of j_t will be relatively easy

¹ We use the term “spheroid” to mean a pressure-dominated stellar system (which may also rotate). A “bulge” is the spheroidal component of a spiral galaxy. An “elliptical” is a galaxy with only a spheroidal component, although many galaxies commonly classified as ellipticals probably have embedded disklike components, similar to those in lenticulars but less obvious. We consider jointly the ellipticals and lenticulars under the general rubric of “early-type” galaxies.

for disk galaxies.

For the elliptical galaxy on the other hand, the halfway mark for j_t is reached at $4.5 R_e$. This is because ellipticals contain a fairly large fraction of their light in their outer regions where the radius lever-arm in $\mathbf{r} \times \mathbf{v}$ is large. The implication is that observations of elliptical galaxies need to extend to much larger radii than for spirals, in order to be confident of capturing the total j_t .

Typical stellar kinematics observations in 1983 extended to $\sim 1 R_e$, and even today, only a small handful of galaxies have been observed kinematically out to $\sim 5 R_e$, which means the positions of the ellipticals in the original j_* – M_* diagram (Figure 1) were highly uncertain, and continue to be challenging to determine with surety. Fortunately, after a great deal of experimentation, which we will discuss below, we find that there is a heuristic approach where observations around $\sim 2 R_e$ can be used to estimate the total j_t of ellipticals with reasonable accuracy.

Returning to a general framework for estimating j_t from observations, there is not only the challenge of extending the data to large radii, but also of having only three of the six phase-space quantities in Equation (1) accessible (i.e., the projected positions and line-of-sight velocity). Even the projection of \mathbf{j}_t on the sky involves unobservable velocity components tangential to the line of sight, and requires additional modeling assumptions.

To cope with these issues, we will model the observed rotation and luminosity profiles of galaxies and convert these to j_t estimates using approximate deprojection factors. Although these factors are based on highly simplified models, the dominant source of uncertainty is still the limited extent of the data to large radii.

We derive in Appendix A two alternative expressions for estimating j_t from observations, both of them based again on the simplifying assumption of cylindrical rotation. The first expression starts with a detailed calculation of a “projected” specific angular momentum proxy that can be estimated directly from observations:

$$j_p = \frac{\int v_{\text{rot,p}}(x) \Sigma(x) x^2 dx}{\int \Sigma(x) x dx}. \quad (3)$$

Here $v_{\text{rot,p}}(x)$ is the observed profile of rotation velocity along the projected semi-major axis x , and $\Sigma(x)$ is the surface density profile, again along the semi-major axis.

The quantity j_p is related to j_t through a “deprojection” factor C_i :

$$j_t = C_i j_p. \quad (4)$$

Therefore the problem of estimating j_t separates into two parts: the calculation of j_p from observations, and the factor C_i which can be calibrated from theoretical models.

As we describe in Appendix A, this latter factor has some dependence on the detailed density–velocity structure of the galaxy, but is primarily a function of the inclination i relative to the line of sight. For thin-disk galaxies, it is simply $C_i = (\sin i)^{-1}$. With spheroidal galaxies, there is an additional dilution effect that comes from the line-of-sight intersecting the rotation field at non-tangent points. In principle, this effect is dependent on the detailed shape of the rotation profile, but we have found with simplified test models that such variations can be neglected in practice. We also find that as long

as the major-axis radius x , rather than a circularized radius R , is used in Equation (3), then C_i is insensitive to galaxy flattening.

A general approximation to C_i as a function of inclination is provided by Equation (A29). It is normally difficult to determine i for spheroidal galaxies, and we will when needed adopt inclination-averaged values.

Equation (3) yields accurate results that are commensurate with the quality of modern observations, but involves numerical integration, and careful compilation of $\Sigma(x)$ and $v_{\text{rot,p}}(x)$ profiles along with extrapolation beyond the bounds of the data.

We could in principle simplify the problem further by using parametric models for $v_{\text{rot,p}}(x)$ and $\Sigma(x)$. Unfortunately, the diversity of observed rotation profiles (when non-spiral galaxies are considered) defies parametrization. We can at least adopt for the surface density the general Sérsic (1968) law which accurately represents a wide range of galaxy types:

$$\Sigma(x) \propto \exp \left[-b_n (x/a_e)^{1/n} \right], \quad (5)$$

where a_e is the effective radius along the *semi-major axis*, and the shape index n determines the steepness of the outer density profile (higher values are shallower: e.g., an exponential disk profile has $n = 1$ and the de Vaucouleurs law for ellipticals has $n = 4$), while b_n is a numerical function of n [Equation (A27)].

We use this $\Sigma(x)$ simplification in practice when deriving j_p from a detailed $v_{\text{rot,p}}(x)$ profile in expression (3). We also generally base our $\Sigma(x)$ profiles on observations of stellar surface brightness profiles $I(x)$, assuming for simplicity that there are no variations of stellar mass-to-light ratio with radius (e.g., due to dust).

Our second method is a quick-and-dirty shortcut for estimating j_t , as needed to generate an initial overview of the trends for a large sample of galaxies. We simply calculate the following linear scalar expression [derived in Appendix A from Equation (3)]:

$$\tilde{j}_p = k_n v_s a_e, \quad (6)$$

where \tilde{j}_p means an approximation for j_p , v_s is the *observed* rotation velocity at some arbitrary measurement location x_s , and $k_n \sim 1-5$ is a numerical coefficient that depends on the Sérsic index n of the galaxy [see Equation (A31)]. As in Equation (4), \tilde{j}_p is multiplied by C_i to provide an approximate \tilde{j}_t . Here the basic idea is that a galaxy can be represented by a characteristic observed rotation velocity scale v_s , a length scale a_e , and a factor k_n that relates to the moment of inertia (discussed further below).

The heuristic approximation that we make here is to select v_s at $x_s \sim 2 a_e$ for all galaxies. We will show in the next section that this choice allows us to estimate j_p with an accuracy of $\sim \pm 0.1$ dex, which is good enough to start making some interesting inferences about trends in j_t .

For $n = 4$ spheroids, the expression equivalent to Equation (2) for spirals is:

$$\tilde{j}_t = 3.03 v_s R_e, \quad (7)$$

for a median, unknown inclination (Equation (A32)). An important concept with the more general expression (6)

is that k_n increases strongly with n ; for fixed galaxy size and rotation velocity, a more extended luminosity profile implies a higher j_p owing to the large fraction of mass residing at large radii. This also means that a spheroidal ($n \sim 4$) galaxy with the *same* observed rotation v_s and size a_e as a spiral has a *larger* specific angular momentum. Late-type and early-type galaxies near the L^* characteristic luminosity *do* have similar sizes for the same stellar mass (e.g., Shen et al. 2003). Therefore we can already make the basic prediction that if j_p at a fixed mass is independent of morphology, then the early-types should have v_s values relative to late-types of $\sim k_1/k_4$, i.e., lower by a factor of ~ 2 .

The j_* formalism that we have outlined here represents a modest extension of the simpler methods in F83. The improvements introduced here include allowance for a range of luminosity profiles (not only $n = 1$ and $n = 4$), and better treatment of elliptical galaxies where rotation at large radii is critically important. It also becomes more straightforward to understand the interplay between observations and uncertainties in the j_* estimates, as explored in the next section.

3. OBSERVATIONS: ANALYSIS METHODS

Before we move on to j_*-M_* analyses of a large sample of galaxies, we examine a small sample in more detail. The goals here are to illustrate the nature of the available data, to demonstrate that the simplified Equations (2) and (6) are good approximations to a full treatment with Equation (3), and to understand some systematic effects in the j_* and M_* determinations.

Because this paper is concerned with the angular momentum bound up in the stellar components of galaxies, the preferred kinematic tracer comes from integrated-light absorption-line spectroscopy. In many cases, such data do not extend to large enough radii, so we make use of additional tracers as proxies for the field stars: cold and warm gas, planetary nebulae (PNe), and metal-rich globular clusters (GCs).

We consider disk- and bulge-dominated galaxies in Sections 3.1 and 3.2, respectively. We evaluate our simplified \tilde{j}_p estimate (6) in Section 3.3, describe our mass estimates in Section 3.4, and then consider systematic uncertainties in Section 3.5.

3.1. Disk-dominated galaxies

The most straightforward galaxies for estimating angular momentum are the gas-rich spirals, since the stellar rotation profile, which cannot always be measured directly, follows the gas rotation profile to a good approximation. Also, the observed rotation can easily be corrected for projection effects in order to recover the intrinsic value (see Appendix A.2). The detailed analysis below is overkill for these galaxies, whose j_t can be readily estimated through Equation (2), but we wish to illustrate how our more general treatment works for them, before moving on to the spheroids.

We consider two real galaxies: NGC 3054 and NGC 3200, which are well-studied disk-dominated spirals from the classic optical rotation curve analyses of Rubin et al. (1982). These cases are chosen to bracket the typical range of inner rotation profile shapes for spirals (slowly and rapidly rising, respectively).

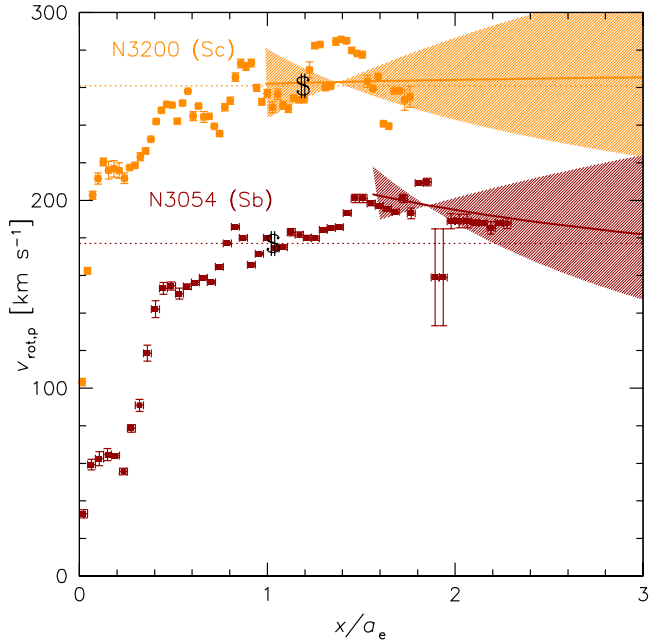


FIG. 4.— Observed rotation-velocity profiles of two spiral galaxies (NGC 3054 and NGC 3200) vs. semi-major axis radius (renormalized by the effective radius). Each galaxy is labeled with its Hubble type. The data are ionized gas velocities from Pizzella et al. (2004). The solid curves with shaded regions show power-law fits (with uncertainties) used to extrapolate the rotation velocity to larger radii. See main text and Appendices A and B for further details. Dotted horizontal lines show the characteristic rotation velocity v_s for each galaxy; the approximate intersection with the corresponding rotation-velocity profile is marked with a \$ symbol and defines the radius x_s (see Section 3.3).

We take the long-slit major-axis ionized-gas kinematics data from Pizzella et al. (2004), shown in Figure 4 after a modest amount of re-binning. These rotation profiles have high-frequency bumps and wiggles that are presumably caused by local perturbations such as spiral arms. Fortunately, these features tend to average out when calculating a cumulative j and are not important in this context.

To calculate the projected specific angular momentum j_p , we carry out a piecewise integration of Equation (3), using the major-axis rotation-velocity data $v_{\text{rot,p}}(x)$ up to $\sim 2 a_e$, along with simple power-law extrapolations at larger radii, as shown in Figure 4. For $\Sigma(x)$, we use an exponential model [$n = 1$ in Equation (5)], with the disk scale-lengths R_d taken from r -band photometry as we will discuss in the next section. Note that $a_e = 1.68 R_d$ for a pure exponential disk.

The resulting cumulative $j_p(\leq x)$ profiles with radius for these galaxies are shown in Figure 5. Here it would be trivial to convert $j_p(\leq x)$ immediately to $j_t(\leq R)$ using the known inclinations of these galaxies, but our general strategy is to focus first on the direct modeling of the observations for all galaxies, and later apply the deprojection factors C_i , which involve different systematics.

It can be seen that j_p hardly changes outside $\sim 3 a_e$, and that the large-radius extrapolations make very little difference: the regions outside ~ 2 – $2.5 a_e$ (~ 3 – $4 R_d$) contain only $\sim 8\%$ – 15% of the total luminosity, and contribute only $\sim 15\%$ – 25% of the total j_p (half of j_p is

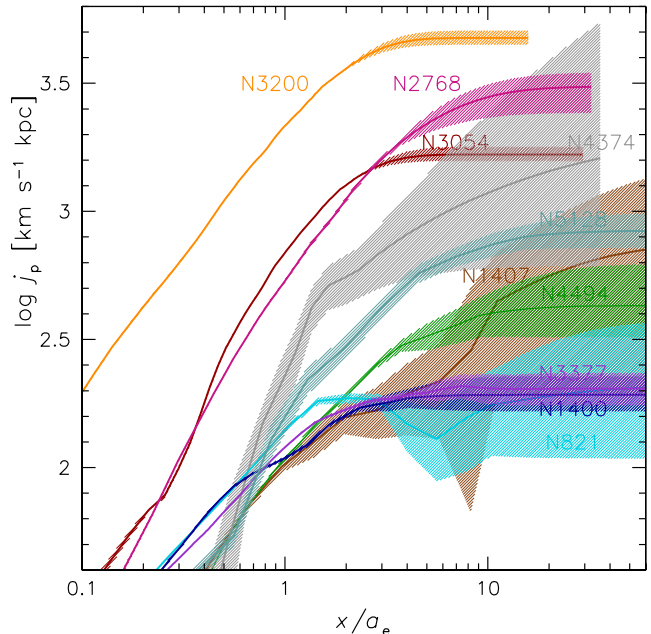


FIG. 5.— The cumulative projected specific angular momentum, $j_p(< x)$, of several nearby galaxies as a function of semi-major axis radius (with log axes), based on modeling of kinematic observations. Solid curves show the best-fit models, with shaded regions illustrating the uncertainties (including those due to extrapolations at large radii). See Table B3 for the distances and a_e values adopted. For most of the galaxies, j_p has nearly reached its asymptotic value by $x \sim 5 a_e$.

enclosed within $\sim 1.2 a_e \sim 2 R_d$; Figure 3). Given reasonable extrapolations of the data, the total j_p for these two galaxies, using our basic modeling assumptions, is constrained to $\sim 5\%$ (~ 0.02 dex).

Thus the kinematics is not a major source of uncertainty for j_t estimation in disk-dominated galaxies. Additional complications that we have not considered here are deviations of the disk surface density profile from a simple constant mass-to-light ratio exponential model, and inclusion of a bulge (to be discussed later). We will examine more general systematic uncertainties in Section 3.5.

3.2. Bulge-dominated galaxies

We now turn to the novel component of this paper, which is the careful treatment of j_t in early-type, bulge-dominated galaxies. Figure 3 demonstrated that traditional observations within $1 a_e$ provide little assurance about the total angular momentum content of these systems, while even current cutting-edge observations out to $\sim 5 a_e$ might in principle not be adequate.

Here we analyze a sample of eight real galaxies in detail in order to characterize the accuracy of j_t estimations. Seven of these galaxies were chosen because of the availability of high-quality extended kinematic data using integrated stellar light spectroscopy from two recent papers (Coccatto et al. 2009; Proctor et al. 2009). Both papers represent the first installments of systematic surveys of early-type galaxies in the local universe, and there is no obvious selection bias for the seven galaxies. Five of them are “ordinary” near- L^* early-types with central “fast-rotator” kinematics as is typical for such galaxies

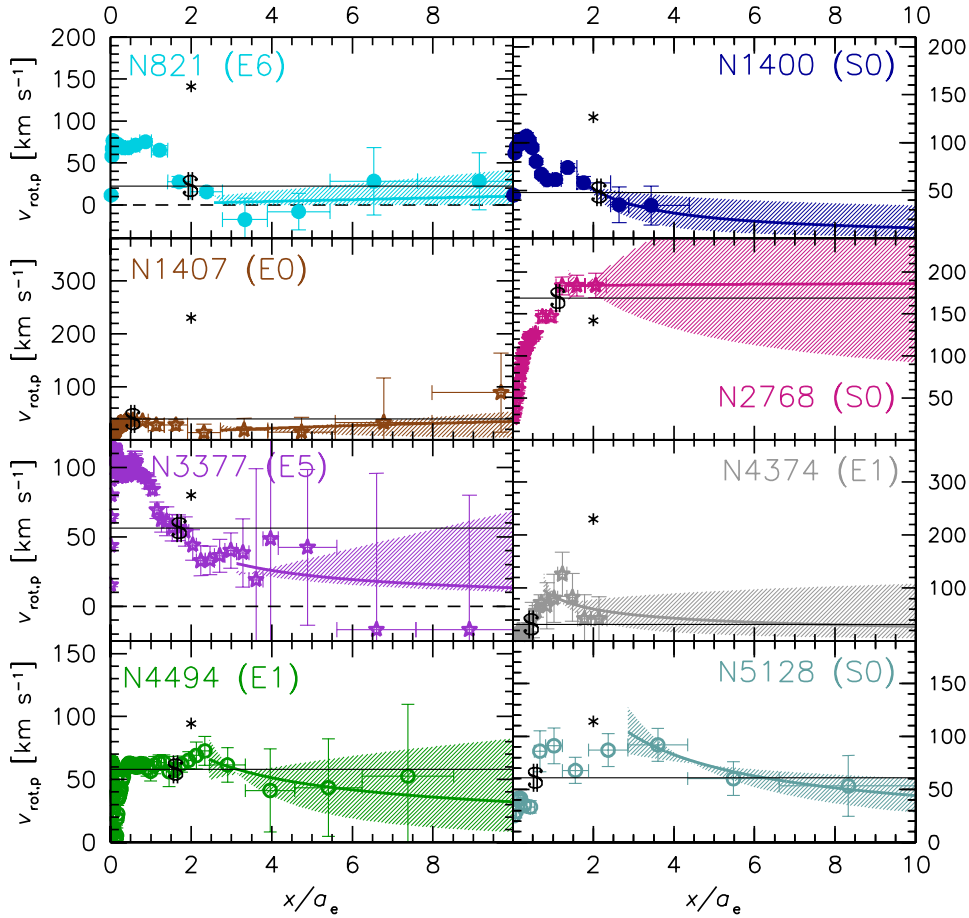


FIG. 6.— Rotation-velocity profiles for eight early-type galaxies. See Figure 4 for further details, including an explanation of the shaded uncertainty regions. For ease of inter-comparisons, the vertical axis of each panel has been scaled according to the velocity dispersion of the galaxy at $2 a_e$, which is marked in each panel by a * symbol. Note the dashed lines at zero rotation velocity in some cases. The galaxies show a diversity of rotation-velocity trends with radius.

(Kormendy & Bender 1996; Emsellem et al. 2011). The other two (NGC 1407 and NGC 4374 = M84) are examples of round, bright “slow rotators” that are common in high-density environments (Cappellari et al. 2011b).

Five of these galaxies also have PN or GC kinematics data available (Coccatto et al. 2009; Romanowsky et al. 2009), which we incorporate into our analysis in order to extend the range of galactocentric radii probed. We include an eighth galaxy in our sample, NGC 5128 (Cen A), because it has the most extended (PN) kinematics data of any early-type galaxy in the literature (Peng et al. 2004). It may also be the remnant of a recent major merger (e.g., Bekki & Peng 2006), which as discussed in Section 1 is expected to generally transfer angular momentum into the outer regions. Analysis of this galaxy thus provides a golden opportunity to search for the “missing” angular momentum, and to see if any clear j_t difference emerges with respect to the other galaxies in the sample.

The use of PNe and GCs to provide proxies for stellar kinematics may seem risky, given the considerable uncertainties that remain about the parent stellar populations of these tracers. However, in most galaxies studied to date, both the density and kinematical profiles of PN and metal-rich GC systems have been found to correspond well to those of the

full stellar population in the regions of overlap (e.g., Coccatto et al. 2009; McNeil et al. 2010; Das et al. 2011; McNeil-Moylan et al. 2012; Cortesi 2012; Pota et al. 2012). We have also verified that this is generally the case for the galaxies in our sample.

Further details of the observations as well as of the kinematical modeling are provided in Appendix B, along with the resulting rotation and angular momentum profiles. It should be emphasized that the careful, homogeneous construction of these profiles is laborious, which is why the current sample of galaxies that we consider in detail is relatively small.

The rotation-velocity profiles of these eight galaxies are summarized in Figure 6. Unlike the spirals (Figure 4), the early-types show great diversity in the characteristic shapes of their profiles. Some are fairly constant with radius, others plummet rapidly from a central high value, and one continues increasing to the limits of the data. This diversity is *not* simply a matter of inclination, as can be seen by the divergent cases of NGC 821 and NGC 2768, which are both highly flattened and probably close to edge-on. We thus find that the central rotation properties of early-type galaxies cannot be used to reliably estimate the total angular momentum content, and there is probably no simple function that universally

characterizes their full rotation-velocity profiles.

As with the spirals, we fit power laws to the outer regions of the rotation data in order to extrapolate to larger radii (see Appendix B for further details). We then use Equation (3) to calculate profiles of cumulative j_p with radius, which we plot in Figure 5. Even though the data do not reach the total asymptotic value for j_p , the requirement of a smooth power-law extrapolation for the rotation-velocity profile does in most cases strongly limit the total j_p , which is typically determined at the $\pm 15\%$ level (± 0.06 dex). The radius enclosing half of the total j_p varies from galaxy to galaxy depending on the shape of its rotation-velocity profile: 0.7–3 a_e (for the two spirals, it is 1 a_e).

The exceptions to these findings are the two bright, round ellipticals NGC 1407 and NGC 4374. Figure 5 shows that much of the angular momentum in these galaxies is found at very large radii (half of j_p within 9 a_e and 4 a_e , respectively), as expected from their fairly high Sérsic indices of $n \sim 4$ –8 (the ordinary early-types have $n \sim 2$ –4). However, beyond the usual uncertainties introduced by extrapolating the rotation velocity, there are a couple of other practical considerations.

One issue is that although these particular galaxies have relatively well studied surface brightness profiles, many such massive ellipticals do not, with their n and a_e values poorly known. This situation produces “double jeopardy” for angular momentum estimation, since both the luminosity and the rotation-velocity profiles at very large radii are important yet poorly constrained.

The other issue demonstrated with NGC 4374 is that its cumulative j_p has not yet converged at the (estimated total) virial radius of $\sim 35 a_e$, so it is not clear how its angular momentum should even be defined. This class of high- n galaxies is clearly problematic, and we will consider any j_t results on them to be tentative for now.

Figure 5 also reveals a first glimpse of the basic result of this paper. For most of the early-types in the sample, there is relatively little angular momentum hidden beyond ~ 1 –2 a_e , and their total values of j_p are lower than those of the spirals. We will make more detailed comparisons later in this paper.

3.3. Simple J/M approximations

We now arrive at a question that is critical for the wider survey of angular momentum in the rest of this paper: how accurate is the simplified Equation (6)? As a reminder, this \tilde{j}_p -estimator would replace the detailed calculations based on Equation (3) that we have carried out in the preceding subsections, but which are time-consuming to carry out for a larger sample of galaxies, and are not even possible for cases without very extended kinematic data.

In Appendix A, we have motivated the construction of Equation (6) via toy models of galaxies, and calculated the corresponding coefficient k_n . We will now apply this formula to the set of ten real galaxies just discussed (both late- and early-types), and find an optimum radial location x_s for measuring the characteristic rotation velocity v_s .

For each galaxy, it is straightforward to find the constant value of v_s which when substituted in Equation (3) yields the same j_p as with the full observed rotation-

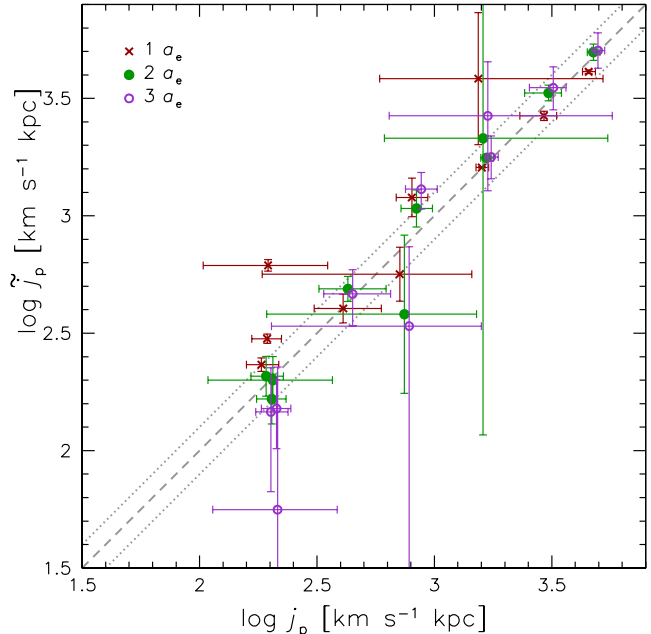


FIG. 7.— Comparison of a simple projected specific angular momentum estimate [\tilde{j}_p ; Equation (6)] with the more accurate value (j_p). Results are shown for ten different galaxies, each with a choice of three reference radii: $x_s/a_e = 1$ (red crosses), 2 (green filled circles), and 3 (purple open circles). Some of the points are given a 0.02 dex horizontal offset for visibility. The dashed and dotted lines mark the one-to-one relation with a ± 0.1 dex scatter. The optimal choice here for x_s is 2 a_e .

velocity profile. These results are listed in Table B3 and shown in Figures 4 and 6, where the intersection of v_s with the rotation-velocity profile determines the characteristic measurement radius x_s . As an example, for NGC 821, it is clear that $x_s \sim 2a_e$. For NGC 4494 on the other hand, a broad range of choices for x_s would work, owing to its nearly constant rotation-velocity profile.

Considering this issue in more detail, we calculate \tilde{j}_p using Equation (6) with an arbitrary choice for x_s (which in turn determines a guess for v_s from the observed rotation velocity at this radius). The results for $x_s/a_e = (1, 2, 3)$ are shown in Figure 7, plotted against j_p calculated in full from Equation (3). It can be seen that $x_s/a_e = 2$ provides a reasonably good match between \tilde{j}_p and j_p for all of the galaxies in this sample. The other radius choices fare worse, owing to galaxies like NGC 821 that have rotation-velocity profiles with a distinct transition between the inner and outer regions near 2 a_e , and thus v_s measurement elsewhere would be biased.

Now to home in more finely on a choice for x_s , in Figure 8 we present the ratio of estimated and “correct” j_p , as a function of the chosen x_s , for each galaxy. Some of the galaxies permit a broad range of choices for x_s , while others do not. Especially noteworthy again are the galaxies like NGC 821 and NGC 3377 which have sharp drops in their rotation-velocity profiles, so v_s measured at small radii would overestimate j_p by factors of ~ 2 –3.

We do not find a strong correlation between n and optimal x_s as expected from the simple models we constructed in Appendix A.4; the dominant effect on x_s with

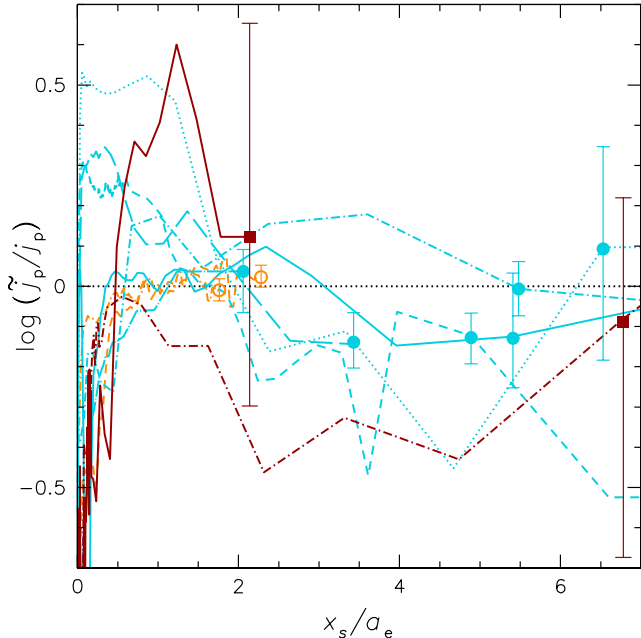


FIG. 8.— The logarithmic ratio between simple estimates of projected specific angular momentum [Equation (6)] and more accurate values [Equation (3)], vs. the rotation-measurement radius x_s in units of the effective radius. Each point indicates a sample ratio for an individual galaxy, with error bars indicating the kinematics-driven uncertainties in total j_p from the detailed models. Results are plotted for 10 galaxies: two spirals (orange profiles with open circles), six ordinary early-types (blue profiles with filled circles), and two giant ellipticals (red profiles with filled squares). As in Figure 7, $x_s \sim 2a_e$ provides a good measurement location, resulting in minimal scatter and bias for the angular momentum estimates.

the real galaxy sample is the scatter in the shapes of the rotation-velocity profiles. Future detailed analyses of a larger sample of galaxies may reveal systematic trends with n that motivate improved j_p estimation methods, but for now we stick with our simple \tilde{j}_p approach.

Because the real galaxies so far do not show strongly rising outer rotation-velocity profiles, and if anything the reverse, $x_s \sim 2 a_e$ appears to be a good overall choice for the rotation-velocity measurement radius. This minimizes the galaxy-to-galaxy scatter in the \tilde{j}_p approximation ($\sim \pm 0.1$ dex), and appears to produce little systematic bias ($< \sim 0.1$ dex). Such “errors” are comparable to the uncertainties from carrying out the full j_p calculations, and are therefore acceptable for our purposes in this paper.

One caveat here is that this sample of galaxies is still small, and we cannot yet be sure of the universal validity of our approximation, e.g., for the larger sample of galaxies that we will study in the remainder of this paper. However, we will show that there is no apparent systematic bias, i.e., the overall scientific conclusions are consistent with the subset of detailed j_p profiles.

3.4. Stellar mass estimates

So far we have focused on estimating j_* , but the other key component in constructing the j_*-M_* diagram is of course the stellar mass M_* . Assuming that we have a well-determined surface brightness profile $I(x)$ or total

luminosity, we then need to know the stellar mass-to-light ratio Υ_* . In this paper, we assume for simplicity that Υ_* is constant throughout each galaxy, which also means that its value is not relevant in our j_* calculations.

Estimating Υ_* in galaxies is a classic and not fully resolved problem. One standard approach is to use theoretical models for stellar populations in combination with observations of the stellar light (e.g., broad-band colors, or spectroscopic line indices). Although there are well-known degeneracies between the ages and metallicities inferred for the stars, fortunately Υ_* can be estimated with more certainty (e.g., Tortora et al. 2009), modulo the initial mass function (IMF) of the stellar populations.

The IMF affects the overall normalization of Υ_* via the mass contributions of late-type dwarf stars or compact stellar remnants, which are observationally difficult to tally. If all galaxies have the same IMF, then our analyses of the *relative* differences between galaxies in the j_*-M_* plane will be secure. There are also recent, indirect claims for possible galaxy-to-galaxy IMF variations (e.g., Davé 2008; Treu et al. 2010; Tortora et al. 2010; van Dokkum & Conroy 2011; Dutton et al. 2012; Ferreras et al. 2012; Smith et al. 2012). However, even in this case we do not expect a major impact on our conclusions.

As an example, the recent analysis of Cappellari et al. (2012) implies that strong IMF variations tend to occur in only the most massive, and relatively rare, early-type galaxies, which would have $\log(M_*/M_\odot) \gtrsim 11.3$ in our plots (based on a standard IMF). Such galaxies might have masses larger than our estimates by factors of ~ 2 , but given the relatively small numbers of such galaxies and the weak constraints on their j_* values, they will have little effect on our estimated j_*-M_* trends.

It is outside the scope of this paper to estimate Υ_* for each galaxy in detail. Instead, we adopt the simplification that all galaxies have $\Upsilon_{*,K} = 1.0$. The near infrared (NIR) K -band is only mildly affected by internal and foreground extinction, is thought to be fairly insensitive to variations in stellar populations, and has uniform photometry available from the 2MASS survey (Skrutskie et al. 2006). The systematic variation in $\Upsilon_{*,K}$ across our entire sample of late and early-type galaxies is conventionally expected to be no more than ~ 0.1 dex, based on $B - V$ colors (Bell et al. 2003), although there are recent suggestions of variations at the level of ~ 0.4 dex (Zibetti et al. 2009; Bershady et al. 2011). Our adopted value of $\Upsilon_{*,K} = 1.0$ is motivated by dynamical estimates in both spirals and lenticulars from Williams et al. (2009, figure 9), and corresponds to an IMF midway between Kroupa (2001) and Salpeter (1955).

Our calculations of M_* also require estimates of total luminosity, L_K . However, we do *not* simply adopt the total magnitudes provided by the 2MASS archive. These values are not reliable for early-type galaxies (e.g., Noordermeer & Verheijen 2007; Devereux et al. 2009; Williams et al. 2009; Schombert 2011), particularly the variety with extended high- n envelopes, where the 2MASS values could be too faint by as much as 1 mag.

Instead, we construct our own “aperture corrections”. We adopt the 2MASS magnitudes within the 20th-mag isophote, K_{20} , and use the best available optical photometry for each galaxy along with a Sérsic model fit to

estimate the fraction of the galaxy light residing beyond K_{20} .

This procedure neglects any bandpass-dependence in the light profiles $I(x)$, which are often more radially extended in bluer bands (e.g., de Vaucouleurs 1961; Peletier et al. 1990; Roediger et al. 2011). Such differences imply Υ_* variations with radius (Tortora et al. 2011), which is a reminder of the limitations of our constant- Υ_* approximation. Given our reliance on optical profiles $I(x)$ to derive $\Sigma(x)$ and estimate j_p , as in Equation (3), for consistency we do need to use the optical data to extrapolate the K -band photometry in estimating M_* . However, the scale-lengths a_e of the stellar mass distributions are probably smaller on average than the a_e values that we use based on optical *luminosity* distributions, leading us to overestimate both j_p and M_* . Improvement on this point could be made in the future by analysis of deep $I(x)$ data at NIR wavelengths. NIR spectroscopy would then also be needed for full consistency of both j_p and M_* estimates (e.g., Silge & Gebhardt 2003; Silva et al. 2008; Vanderbeke et al. 2011).

3.5. The j_* - M_* diagram

Here we focus on the j_* - M_* plane, our ultimate destination in this paper, but for now considering the projected specific angular momentum j_p rather than the true j_t in order to isolate various effects that are disjoint from inclination uncertainties. Figure 9 shows our detailed galaxy sample where cumulative $j_p(< R) = J_p(< R)/M_*(< R)$ is plotted not as a function of radius (as in Figure 5) but of *enclosed projected stellar mass*, M_* .

For reference, we show dashed lines corresponding to $j_p \propto M_*^\alpha$, with $\alpha = 2/3$. This value for α is motivated by previous observations (Section 1), and by theoretical predictions for j_t - M_* , given constant values of an initial halo spin parameter λ , as we will see in Section 6.1. We are most concerned with the locations of galaxies relative to these tracks, and with any systematic effects that could shift the data in a direction *perpendicular* to them.

The shaded regions of the curves in Figure 9 indicate the uncertainties due to the kinematic data, including the extrapolations to large radii. For most of the galaxies, the asymptotic position in the j_p - M_* diagram is relatively well determined. The main exceptions are NGC 1407 and NGC 4374, which as discussed before are extended giant ellipticals whose total j_p is very difficult to determine. The early-type galaxy NGC 2768 is also a concern even though the formal j_p uncertainties are small, since there are large contributions to the total j_p estimate from the region of extrapolation.

An offset in total j_p between the late-types and most of the early-types as in Figure 5 is also apparent in Figure 9. However, the mass dimension brings the relative positions into sharper focus. For example, NGC 4374 and NGC 5128 have similar j_p values to NGC 3054, but also have larger stellar masses, which means that their inferred halo spins will be *lower* (considering distances perpendicular to the dashed tracks).

We next consider some systematic uncertainties that apply even if the rotation-velocity profiles are perfectly measured. First, there is a typical distance uncertainty of $\sim 10\%$. This affects j_p linearly and M_* quadratically, moving the position of the data by a very small amount

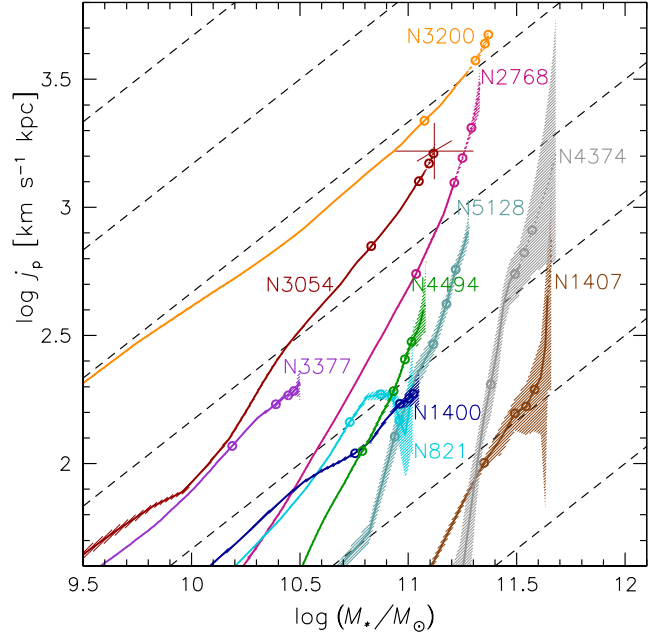


FIG. 9.— The cumulative projected specific angular momentum of nearby galaxies (as in Figure 5), now plotted vs. cumulative projected stellar mass. The curves are *solid* where constrained by the data, and *dotted* for extrapolations. Circles show intervals of $1 a_e$, up to $4 a_e$. Error bars at the end of the NGC 3054 curve illustrate the effects of systematic uncertainties (see text for details): diagonal for the distance, vertical for scale-length, and horizontal for Υ_* . Diagonal dashed lines show tracks of $j_p \propto M_*^{2/3}$, which represent constant halo spin.

nearly parallel to the λ tracks (see sample error bars marked for NGC 3054 in the Figure).

Next we consider an uncertainty of $\sim 30\%$ (~ 0.11 dex) in the scale lengths a_e , which translates into a similar uncertainty in j_p [see Equation (2)].² Also, in some cases the surface brightness profile is well constrained and the associated j_p uncertainty is very small (e.g., $\sim 5\%$ or ~ 0.02 dex in the case of the $n \sim 3$ elliptical NGC 4494).

Finally there is Υ_* , which may be uncertain by a factor of $\sim 50\%$ (~ 0.2 dex) and would affect M_* by the same amount. For spiral galaxies, this is probably the limiting factor for inferring their λ values. For the early-types, the inclination is generally unknown and may be a significant source of uncertainty for estimating j_t , even when j_p is well constrained. We will return to this theme in Section 5.1.

4. OBSERVATIONS: SCALING RELATIONS AND DERIVATIONS OF J/M FOR THE FULL SAMPLE

Having carried out detailed analyses of j_* for a handful of galaxies in the previous section, we now derive j_* for a much larger galaxy sample, using simpler methods. Besides these derivations, in this section we also examine some basic scaling relations for galaxies, in order to understand the observational underpinnings of the j_* - M_* results in the next section, and to verify that our results are consistent with some well-known properties of galaxies. We also introduce a novel, generalized version of the

² In practice, the a_e uncertainty is correlated with an uncertainty in the galaxy luminosity and thus in M_* , but this is a relatively weak effect.

Tully-Fisher relation for galaxies of all types. Those who are keen to get straight to the angular momentum results may wish to skip to Section 5.2.

In order to populate the observational j_\star - M_\star diagram, we will use the j_p approximation of Equation (6) which we have found to be generally accurate at the ~ 0.1 dex ($\sim 25\%$) level. The basic parameters that we then need for all of the galaxies are: the total stellar mass (M_\star) and its scale-length (R_d or a_e), the Sérsic index n , and the characteristic rotation velocity v_s .

The distances to the galaxies are estimated from redshifts and surface brightness fluctuations. As discussed in Section 3.4, M_\star is derived from aperture-corrected 2MASS magnitudes m_K , assuming $\Upsilon_{\star,K} = 1.0$.

The other parameters are derived differently for the late-type and early-type samples, as we will discuss in Sections 4.1 and 4.2, respectively. Section 4.3 brings the data together in an examination of basic scaling relations, before proceeding to the final j_\star - M_\star analyses of Section 5.

4.1. Late-types

Because spiral galaxies are dominated by their disk components, whose photometric and kinematic properties are relatively straightforward to measure, past studies of their angular momenta have generally treated them as pure disks, e.g., using Equation (2) to calculate j_t . However, this approximation may be inadequate for the spirals with relatively large bulges (Sa and some Sb), and it is one of the goals of this paper to consider these components.

With Equation (6) in mind, we could use values for the parameters n , a_e , and v_s that characterize the composite bulge-disk systems (e.g., with an overall n somewhat larger than 1). However, the required stellar photometry and kinematic data are not available for a large sample of galaxies. Instead, we analyze disk and bulge components separately, make some simple assumptions for the bulges to compensate for the missing data, and then combine the disks and bulges into global j_\star analyses.

We focus on the classic spiral galaxy data set assembled by Kent (1986, 1987, 1988), comprising 64 galaxies from type Sa to Sm, at distances ranging from 1 to 100 Mpc. These data include r -band CCD photometry along with bulge/disk decompositions, and inclination-corrected gas-disk rotation curves from both optical emission-lines (e.g., Rubin et al. 1980, 1982, 1985) and HI radio emission (based on various sources in the literature). Most of Kent’s sample comes from the Rubin et al. surveys, which selected for spiral galaxies with high inclinations, spanning a wide range of luminosities, scale-lengths, and Hubble types, and without strong bars. Despite advances in observational resources in the intervening decades, we know of no comparable, publicly-available sample that includes both rotation curves and photometry with detailed bulge/disk decompositions for a wide range of disk-galaxy types.

We estimate the disk and bulge scale-lengths (R_d and $a_{e,b}$) by modeling the nonparametric Kent decompositions with simple exponential and de Vaucouleurs profiles ($n = 1$ and $n = 4$, respectively). Our models thereby treat all bulges as “classical”, with $n \sim 4$, neglecting some variations in their detailed properties, such as the $n \sim 1$ -2 indices of “pseudo” bulges

(Kormendy & Kennicutt 2004). The latter bulges tend to be much less massive, and make only minor contributions to the total j_\star for spirals, which is insensitive to the details of the adopted bulge density and rotation profiles.³

For 34 of these sample galaxies (type Sb to Sc), independent decompositions were carried out on the *same data set* by Andredakis & Sanders (1994), using parametric fits to the raw surface brightness profiles. Our R_d values agree with theirs at the $\sim 10\%$ level, while the bulge results are highly variable, both between our analyses and theirs, and between different model fits by these authors. Most of these galaxies are very disk dominated ($B/T \lesssim 0.1$), so it is not surprising that the bulge parameters would be very uncertain. Fortunately the bulges in such cases turn out to be only very minor contributors to the total j_\star of their host galaxies. Other parameters and their sources are listed in Table C4.

For v_s of the stellar disk components of these galaxies, we assume that they rotate with the same velocities as their gas disks. We derive v_c based on the rotation curves over the range (2–3) R_d , re-projecting this intrinsic value to the observed v_s according to the inclination ($v_s = v_c \sin i$).

The final and most challenging parameter to estimate is the characteristic rotation velocity v_s for the bulges. Direct estimates of bulge rotation-velocity profiles over a large range in radius require extensive spectroscopic data combined with careful bulge-disk kinematic decomposition. As far as we know, this has only been done for *one* spiral galaxy to date (Dorman et al. 2012). Thus we are much worse off with estimating j_\star for spiral bulges than for early-type galaxies, and must make even stronger simplifying assumptions than in the original F83 analysis of ellipticals. Fortunately, because the spirals are disk-dominated, we will find that their total j_\star estimates are only mildly sensitive to the assumptions about bulge kinematics.

Our strategy for the bulge v_s values is to estimate these indirectly, based on other observables: the ellipticity $\epsilon \equiv 1 - q$ and the central velocity dispersion σ_0 . These three parameters may be related together through the following model:

$$v_s = \left(\frac{v}{\sigma}\right)^* \sigma_0 \left(\frac{\epsilon}{1 - \epsilon}\right)^{1/2}, \quad (8)$$

where $(v/\sigma)^*$ is a parameter describing the relative dynamical importance of rotation and pressure. In an edge-on galaxy, $(v/\sigma)^* \simeq 1$ represents an oblate isotropic system where the observed ellipticity is supported by rotation, and this model also turns out to work well at other inclinations (Kormendy 1982).

The standard lore is that spiral bulges and low-luminosity ellipticals are near oblate-isotropic, with typical $(v/\sigma)^* \sim 0.9$ (Kormendy & Illingworth 1982; Davies et al. 1983; Binney & Merrifield 1998; Binney & Tremaine 2008). However, some concerns about these conclusions were raised early on (Whitmore et al. 1984; Fillmore et al. 1986) and mod-

³ More extensive observations and modeling in the future could be used to establish the j_\star - M_\star trends for morphologically different bulges, and thereby provide physically-based information as to whether or not there are genuinely distinct subtypes.

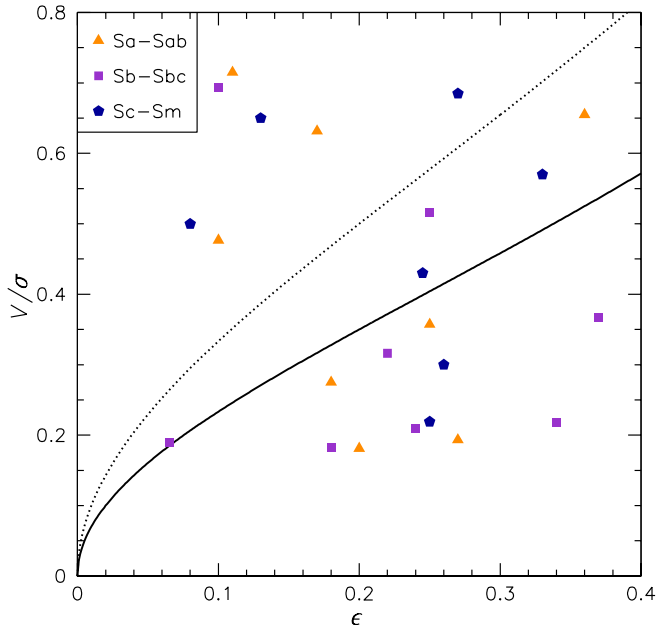


FIG. 10.— Relation between bulge rotation velocity and velocity dispersion as a function of ellipticity. The points show data for 26 spiral galaxies from the literature, with symbol shapes and colors corresponding to different Hubble types as in the legend. The curves show Equation (8) with $(v/\sigma)^* = 1$ and $(v/\sigma)^* = 0.7$ for the dotted and solid curves, respectively. We adopt $(v/\sigma)^* = 0.7$ as our default model.

ern integral-field analysis of early-types has revealed that their rotation velocities tend to be significantly *lower* than in the oblate isotropic model (Cappellari et al. 2007; Emsellem et al. 2011). The rotation of spiral bulges, on the other hand, has not seen systematic investigation in decades (some new work has just appeared in Fabricius et al. 2012), and here we attempt only a quick look at the implications of recent papers that have reported bulge kinematics for a handful of cases.

We take results on (v/σ) and ϵ from Laurikainen et al. (2007), Morelli et al. (2008), and MacArthur et al. (2009), and plot them in Figure 10. We see that the oblate isotropic model is *not* a good representation of most of the data, nor is any other simple value of $(v/\sigma)^*$. However, in order to have a simplified framework for bulge rotation, we characterize this data set as having $(v/\sigma)^* = 0.7 \pm 0.4$ (median and 68% scatter).

We therefore adopt the following procedure for estimating bulge j_* . We use the observational values for ϵ and σ_0 , and then estimate v_s using Equation (8) with $(v/\sigma)^* = 0.7$ representing a typical value for bulges. We test the impact of the latter assumption on the results by also using $(v/\sigma)^* = 0.3$ and 1.1 to bracket the possible range of average bulge rotation. We thereby explore the systematic uncertainty in bulge rotation but not the intrinsic scatter, keeping in mind also that this bulge model is based on the central regions and does not account for the uncertainties in extrapolating the rotation to large radii, as discussed in detail for the early-type galaxies.

The ϵ values are taken from the Kent derivations. We take the σ_0 measurements in most cases from HyperLeda (Paturel et al. 2003), and also from Corsini et al. (1999) and Pizzella et al. (2004). For some of the later-type

galaxies, there are no σ_0 measurements available, and for these we use an empirical relation (which we infer from other galaxies in these studies) that σ_0 is approximately equal to the gas-disk rotation velocity. Such cases all have $B/T < 0.15$, so this approximation is not of major importance for the total j_* estimates, but any inferences for these particular bulges will be relatively uncertain.

We now have enough information to proceed with the specific angular momentum calculations for the spiral galaxies. Again, our basic approach is to estimate separately the bulge and disk angular momenta j_b and j_d . Given a bulge stellar mass fraction quantified as f_b , we can then estimate the total specific angular momentum by:

$$j = f_b j_b + (1 - f_b) j_d. \quad (9)$$

In practice, we use the bulge-to-total r -band luminosity ratio B/T (from the series of Kent papers) as a proxy for f_b .

To calculate the projected values of j_b and j_d , we use Equation (6). For the intrinsic values, we assume that both the bulge and the disk in a given galaxy have the same inclination i , which is estimated from the observed disk ellipticity. We then use the deprojection factor C_i to convert projected to intrinsic values [see Equation (4)]. For the disk, this is a simple factor of $(\sin i)^{-1}$, and the calculation reduces to Equation (2). For the bulge, we calculate C_i from Equation (A29).

Using these procedures, we construct a catalog of spiral galaxies with characteristic masses, scale-lengths, and rotation velocities for both their bulge and disk components. We report these values in Table C4, along with the total galactic specific angular momenta (bulge and disk combined), both projected and intrinsic. When we vary the assumed bulge rotation systematically across the bracketing range, the total j_* is changed by no more than ~ 0.03 dex ($\sim 7\%$) for the vast majority of the galaxies, and up to ~ 0.1 dex ($\sim 25\%$) for a few of the Sa-Sab galaxies. Therefore the details of the bulge modeling are of only very mild importance to the overall j_* results for the spirals. These data will be used in later sections to examine various scaling relations for these galaxies and for their subcomponents.

4.2. Early-types

For the gas-poor early-type galaxies (lenticulars and ellipticals), the challenge is to assemble a large sample with all of the ingredients that we need to calculate j_* (i.e., v_s , a_e , n). The information is scarcest for v_s , and therefore we have scoured the literature for kinematic data sets extending to radii of at least $\sim 2 a_e$, assembling a sample that, although not exhaustive, is unprecedented in its size and scope. The sources include integrated-starlight absorption-line spectroscopy, and velocities of GCs and PNe. To estimate approximate values for v_s , we simply read off the major-axis rotation velocity at $2 a_e$ (as explained in Section 3.3). We thereby assemble a total sample of 40 early-type galaxies, including the 8 galaxies that we modeled in detail in Section 3.

Table C5 provides a summary of our sample, along with the sources of kinematic data. Given that the data are drawn from a variety of literature sources with complex selection effects, it is important to check whether or not the sample is a fair representation of early-types in

the nearby universe. We have done so in Appendix C, using the ATLAS^{3D} volume-limited sample of nearby galaxies as a reference, and focusing on the masses M_* and central rotation parameters $(v/\sigma)^*$.

We find that the distribution of our sample galaxies in the $(v/\sigma)^*-M_*$ parameter space is fairly similar to that of an unbiased sample over a similar mass range. The median galaxy mass in our sample is $\log(M_*/M_\odot) = 10.8$, which is near the characteristic mass M_*^* of nearby galaxies (Guo et al. 2010). We thus conclude that our observational results should be representative of low-redshift ordinary early-type galaxies. The only caveat here is that our sample is biased toward ellipticals at the expense of lenticulars, which we must take into account later when drawing conclusions about the overall population of early-type galaxies.

An alternative scheme for classifying early-types is as “fast rotators” (including almost all lenticulars) and “slow rotators”, based on their central kinematics (Emsellem et al. 2007). The central rotation is known to correlate with many other galaxy properties (Davies et al. 1983; Kormendy & Bender 1996), and the fast and slow rotators have been interpreted as having different formation histories. Therefore it is important that we investigate to what extent the *global* specific angular momentum j_* correlates with the central rotation classification. Our sample includes three slow-rotators, which is consistent with the fraction of such galaxies in the nearby universe (Emsellem et al. 2011), and will provide a rough initial idea of any systematic differences between fast and slow rotators.

Returning to the remaining observational parameters, for each early-type density profile, we need both the Sérsic index n and the corresponding scale-length a_e (which can differ significantly from the value obtained with a classic $n = 4$ fit, e.g., in the RC3 catalog of de Vaucouleurs et al. 1991). Unfortunately there is no comprehensive source available for such measurements, and we resort to a medley of literature data.

For 34 of the galaxies in our sample, there are published Sérsic fits, and we take the (a_e, n) values according to the following priority: detailed photometric analysis in individual galaxy papers (e.g., Napolitano et al. 2009); the Kormendy et al. (2009) tabulation for Virgo galaxies; Hopkins et al. (2009a); Hopkins et al. (2009b); D’Onofrio (2001).

For the remaining 6 galaxies, we have as a starting point the RC3 value for the effective radius. Then we use the well-established observation that there are strong correlations between early-type galaxy size and luminosity, and the Sérsic index n (e.g., Caon et al. 1993; Prugniel & Simien 1997; Graham & Guzmán 2003; Blanton et al. 2003; Kormendy et al. 2009). This allows us to estimate a most-probable n value for each galaxy (see Appendix C for details).

Note that if we were simply to approximate all of the early-types as $n = 4$ spheroids, the k_n values in Equation (6) would be too high on average by $\sim 30\%$ (~ 0.15 dex, given a median index value of $n \sim 2.5$). This would translate to an equivalent systematic error on j_* . We could adjust for this effect by adopting $n = 2.5$ in all cases, but n also has a systematic dependence on galaxy mass, and ignoring this fact would produce a spurious mass-dependent trend in j_* of $\sim 50\%$ (~ 0.2 dex) over

the full range in mass.

In Table C5, we compile the observed parameters v_s , a_e , and n for our full early-type galaxy sample. We use these to calculate j_p approximately from Equation (6), and tabulate these values as well. For some of the very extended galaxies like NGC 4374, the total luminosity and angular momentum (via the factor k_n) are integrated out only to the estimated virial radius.

In order to convert projected j_p to intrinsic j_t for analysis in later sections, we must apply a deprojection factor C_i which depends on the inclination i . Unfortunately, the individual inclinations are not generally known, but neither are they completely random, because of an inclination-bias in galaxy classification. As discussed in Appendix A.3, we therefore apply median deprojection factors of $C_{\text{med}} = 1.21$ ($+0.08$ dex) to the lenticulars, and $C_{\text{med}} = 1.65$ ($+0.22$ dex) to the ellipticals.

Since one of our eventual goals will be to quantify the intrinsic scatter in the observed j_*-M_* relations, it is important to be clear about the error budget in our analyses. Again, the basic parameters that go into our j_* calculations are C_i , a_e , n , and v_s . For early-type galaxies with an assumed $n = 4$ profile, the typical uncertainties in a_e are $\sim 25\%$ (~ 0.1 dex; Cappellari et al. 2011a). If we allow for a more general n , which for some galaxies is measured directly and in other cases is derived statistically (Appendix C), then we estimate a combined uncertainty on j_* from a_e and n of $\sim 40\%$ (~ 0.15 dex). The uncertainty on v_s from our simplified measurement and extrapolation approach is $\sim 25\%$ (~ 0.1 dex; Section 3.3).

Table 1 summarizes the uncertainties introduced by a number of different ingredients in the j_*-M_* calculations. The separate uncertainties for j_* and M_* are mapped to the direction perpendicular to a $j_* \propto M_*^{2/3}$ trend, as discussed in Section 3.5. This net uncertainty is designated $\Delta\lambda$, owing to the connection with spin-based theoretical models.

The total uncertainty in λ for late-type galaxies is typically $\sim 30\%$ (~ 0.1 dex), and is driven by the estimate of M_* (via Υ_*) rather than j_* . For the vast majority of the early-types (apart from the special class of massive, extended ellipticals), the uncertainty is $\sim 60\%$ (~ 0.2 dex), and is driven by the four parameters mentioned above that enter into the j_* calculation.

This full j_*-M_* dataset is assembled from a generally unbiased $\sim M_*^*$ galaxy sample that we can use to investigate differences in angular momentum not only between early-types and spirals, but also between ellipticals and lenticulars, and between fast and slow rotators.

4.3. Size and rotation-velocity scaling relations

Before considering specific angular momenta and their correlations in the next section, we examine some trends among the raw ingredients that go into these analyses, a_e , v_s , and M_* . Doing so provides a check that our results are consistent with the familiar size-mass and mass-rotation velocity (Tully-Fisher) relations that have been established for nearby galaxies. We also introduce novel relations involving rotation, and explore some preliminary indications about angular momentum.

We first consider the standard scaling relation of galaxy

TABLE 1
UNCERTAINTY BUDGET

Galaxy type	$\Delta\lambda$ (dex)							
	D	C_i	v_s	\tilde{v}_s	n, a_e	bulge	Υ_*	total
Sb–Sm	0.01	0.01	0.02	0.03	0.05	0.03	0.07	0.09
Sa–Sab	0.01	0.01	0.02	0.03	0.05	0.1	0.07	0.13
S0	0.01	0.05	0.06	0.1	0.15	0	0.07	0.18
fE	0.01	0.15	0.06	0.1	0.15	0	0.07	0.22
sE	0.01	0.12	0.35	0.35	0.2	0	0.2	0.40

NOTE. — The uncertainties on j_* and M_* have been converted into equivalent uncertainties on λ . The different galaxy types include fast- and slow-rotating ellipticals (fE and sE). The listed sources of potential error are distance (D), corrections for projection effects including inclination (C_i), the rotation velocity scale calculated in detail (v_s), the alternative approximate rotation velocity scale (\tilde{v}_s), the stellar density profile Sérsic index (n) and scale radius (a_e), the incorporation of bulge contributions, and the stellar mass-to-light ratio including IMF variations (Υ_*).

size versus mass, or a_e versus M_* in our notation, showing the results in Figure 11, where we again compare our results to the volume-limited ATLAS^{3D} sample as a baseline check. We find that in both samples, late- and early-type galaxies have *roughly* the same sizes at a given mass (cf. Shen et al. 2003, 2007), but there is a clear systematic trend for the more bulge-dominated galaxies to be more compact (see also de Jong et al. 2004; Gadotti 2009; Maltby et al. 2010; McDonald et al. 2011; Dutton et al. 2011). Given the many different assumptions and data sources that went into our sizes and masses, these parameters match the ATLAS^{3D} results remarkably well overall (with some nuances discussed further in Appendix C). This suggests that our size and mass data are representative and reliable at the ~ 0.1 dex level.

We can also consider separately the spiral *bulges*, plotting their sizes and masses for our sample in Figure 11. Although the full range of sizes is not visible in this plot, the bulges follow a roughly parallel size–mass relation to the elliptical galaxies, but smaller on average by a factor of ~ 4 (~ 0.6 dex) and with a great deal of scatter (possibly because of the approximate nature of these size measurements). Other studies have also found that bulges are more compact than ellipticals (Graham & Worley 2008; Gadotti 2009; Laurikainen et al. 2010; Dutton et al. 2011), but the quantitative details vary considerably, and we therefore regard our bulge scaling relations as provisional.

The next scaling relation that we consider is rotation velocity versus mass. For spiral galaxies, this is the Tully-Fisher relation, but it has to our knowledge never been constructed previously for all galaxy types. We can already generate a broad expectation for what we will find, given the observed size–mass relations along with the assumption that j_* is independent of galaxy type. As mentioned in Section 2, we can then use Equation (6) to predict the ratio of characteristic rotation velocities for ellipticals and spirals:

$$\frac{v_{s,E}}{v_{s,Sp}} \sim \frac{k_1 a_{e,Sp}}{k_4 a_{e,E}}, \quad (10)$$

where we are approximating the spiral galaxy parameters as dominated by the disk component. With $k_1/k_4 = 0.5$, and $a_{e,Sp}/a_{e,E} \sim 2$ for our sample, we therefore predict

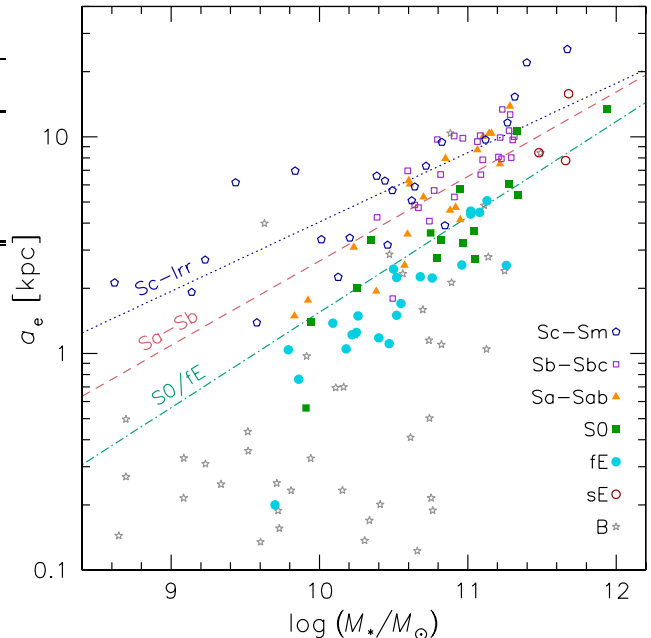


FIG. 11.— Relation between size and stellar mass for our galaxy sample. The former is the semi-major axis effective radius, and the latter is based on K -band total luminosities with an adopted mass-to-light ratio of $M_*/L_K = 1$ in solar units. Different symbols denote different galaxy types as shown in the legend; for the spirals, the disk and bulge (“B”) components are shown separately. The range of the plot is restricted in order to better see the main trends in the data; the bulge data extend to radii as small as $a_e \sim 0.01$ kpc (note also that the most compact elliptical shown is NGC 4486B, which is considered a rare, highly-stripped galaxy). For comparison, diagonal lines show power-law model fits to the data from the ATLAS^{3D} survey (i.e., *independent* from our data set): lenticulars and fast-rotator ellipticals (dot-dashed), Sa–Sb spirals (dashed), and Sc–Irr spirals (dotted). For both data sets, the late-type galaxies are systematically larger than the early-types at a given stellar mass. The absolute normalizations of the trends are similar between the ATLAS^{3D} sample and ours, with some small differences as discussed in the text.

$v_{s,E}/v_{s,Sp} \sim 1$. Thus, *ellipticals should rotate at roughly the same velocity as spirals if they have the same specific angular momenta at a given mass.*

Without proceeding any further, this scaling analysis already suggests that ellipticals have lower j_* than spirals, or else they would be extremely flattened by rotation, similarly to the spiral disks which have near-maximal rotational support (modulo possible differences in dynamical mass between spiral and elliptical galaxies at the same stellar mass). The same argument applies even more strongly to the spiral bulges, since they are far more compact than the disks at a given mass. If the bulges had the same j_* as the disks, then they would have to rotate much *faster*, which is impossible.

We now examine what our new collection of observations tells us directly about the rotation scaling relations. The left-hand panel of Figure 12 shows the characteristic rotation velocity v_s for the elliptical and lenticular galaxies, and the spiral disk and bulge subcomponents, in our sample. Here we are plotting the *intrinsic* rotation velocity, multiplying by the deprojection factor C_i , which is just $(\sin i)^{-1}$ for disks (see Appendix A.2), and Equation (A29) for bulges. For the early-type galaxies, the inclinations are unknown, and we have adopted median

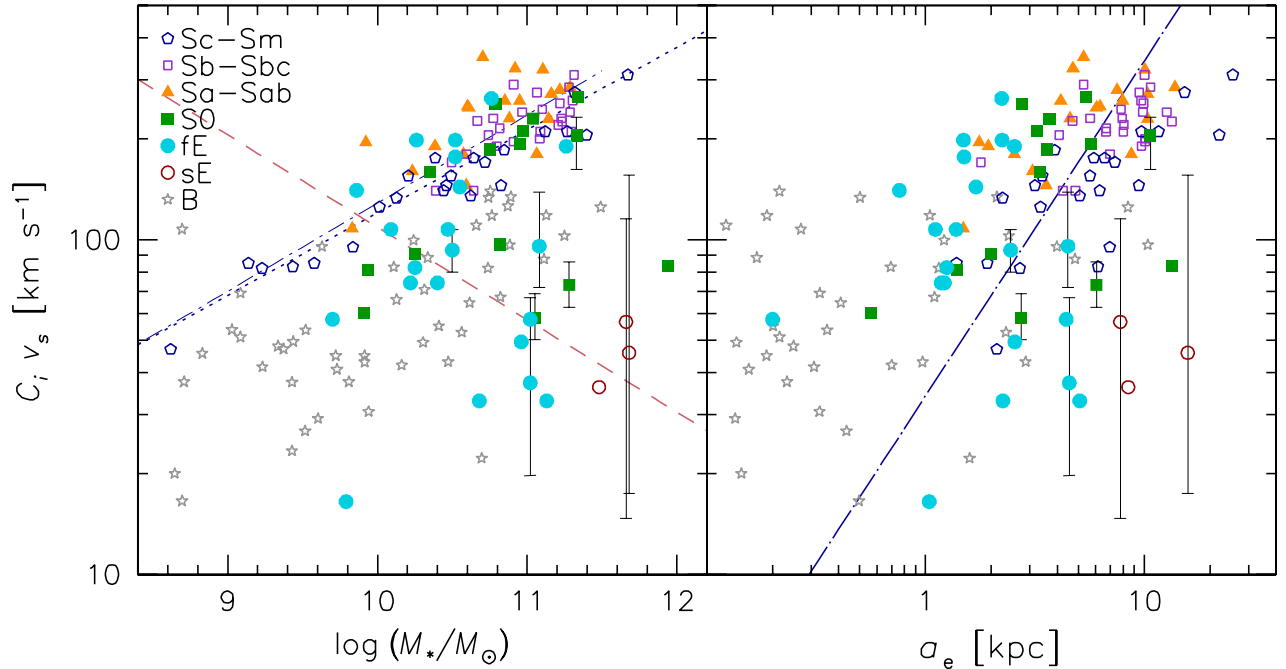


FIG. 12.— Relations between characteristic rotation velocity $C_i v_s$, stellar mass (left-hand panel), and size (right-hand panel) for our full galaxy sample, using the same data sources and symbols as in Figure 11. For the spiral disks, v_s is the outer gas-disk rotation velocity. For the lenticulars and ellipticals, v_s is the stellar rotation velocity measured along the semi-major axis at $2 a_e$, except for the points with error bars, which are the eight cases studied in detail in Section 3, with v_s derived from full modeling of the rotation-velocity profiles. For the bulges, v_s is estimated indirectly using flattening and velocity dispersion observations (Section 4.1). In all cases, the rotation velocity has been deprojected for both inclination and “dilution” effects, using the factor C_i (see text for details). In the left-hand panel, the dotted blue line shows a least-square fit to the Sb–Sc disks, a dashed red line shows a proposed inverse trend for a subset of the E/S0s, and the blue dot-dashed line shows the baryonic Tully-Fisher relation for late-type galaxies from Trujillo-Gomez et al. (2011) for comparison. In the right-hand panel, the diagonal line shows a prediction for the spiral disks based on Λ CDM models (see Section 6.2). Overall, the spiral and elliptical galaxies follow mass–rotation velocity and size–rotation velocity trends that have remarkably opposite slopes. The trends for the lenticulars are between the spirals and ellipticals.

factors for C_i as discussed in Section 4.2.

We see that the disks follow a fairly tight relation of approximately $C_i v_s \propto M_\star^{0.25}$, with a residual trend for the later-type disks to rotate more slowly. This is equivalent to the familiar Tully-Fisher relation, and in the Figure we include a recent result from the literature (Trujillo-Gomez et al. 2011), which matches our data very well (cf. the type-dependence among spirals found by Masters et al. 2008). We also show in the right-hand panel of Figure 12 the relation between size and rotation velocity, which are strongly correlated parameters for disk galaxies.

The elliptical galaxies are completely different, showing an *anti-correlation* between rotation velocity and mass,⁴ with $C_i v_s \propto M_\star^{-0.1}$. This result also contrasts markedly with standard relations for ellipticals involving the velocity dispersion σ_0 or the dynamical mass (e.g., $\sigma_0 \propto M_\star^{0.25}$; Faber & Jackson 1976; Trujillo-Gomez et al. 2011). In galaxy disks, the rotation velocity traces the dynamical mass, so the Tully-Fisher relation is a measure of both mass and angular momentum. In elliptical galaxies, on the other hand, the mass and angular momentum relations are decoupled. We also find an anti-correlation between rotation veloc-

⁴ This echoes a similar trend in the *central* rotation properties of early-type galaxies in general (shown in Figure 33). The eight galaxies studied in detail (points with error bars in Figure 12) are consistent with this trend but do not include enough lower-luminosity ellipticals to distinguish between v_s being constant or decreasing with mass.

ity and size (right-hand panel) that we will discuss later in this paper.

The behavior of the lenticulars in the mass–rotation velocity diagram is difficult to discern in detail owing to the small sample size, but in general it appears intermediate to the other galaxy types. We also notice an interesting pattern when considering the lenticulars and ellipticals together: there may be a *bimodal* mass–rotation velocity relation,⁵ with some galaxies following the trend for spirals, and others following a steep reverse relation, $C_i v_s \propto M_\star^{-0.3}$. The implication is that there may be two distinct populations of early-type galaxies, one of which is closely related to spirals, and which are not equivalent to standard E and S0 classifications.

The bulge rotation velocities appear to follow a similar trend to the spirals, at about half the amplitude. Here it should be remembered that the bulge “data” points are *indirect* estimates constructed in order to provide plausible adjustments to the total angular momenta of the spiral galaxies (Section 4.1). The results so far suggest that bulges are different from ellipticals in their mass–

⁵ This pattern may be partially an artifact of inclination effects. In particular, some of the edge-on lenticulars were observed with long-slit spectroscopy directly along their embedded disks, which may not provide an accurate measurement of the overall rotation. However, for the ellipticals we find no correlation between apparent rotation velocity and ellipticity. An additional issue is that the occasional extremely low-inclination galaxy will not be treated well by our median-deprojection method (cf. the right-hand panel of Figure 24), so in any fits to the data, we will discard outliers with very low v_s or j_\star (e.g., NGC 1419).

size–rotation velocity relations, and we will see in the next section how their angular momenta compare.

Since both the sizes and the rotation velocities of elliptical galaxies are systematically lower than for spiral disks, we can already predict that the ellipticals will on average have much lower j_* . Note that although this conclusion has already been widely adopted for decades, only now have the kinematic data reached large enough radii to confirm it with confidence.

To see that the low characteristic rotation velocities for ellipticals are not a mathematical sleight of hand, one may consider the specific cases of NGC 821 and NGC 3377 in Figure 6. The rotation-velocity profiles of these galaxies decline dramatically outside $x \sim (1-2) a_e$, which may be contrasted with the spiral galaxies in Figure 4. Preliminary analysis of additional *edge-on* cases, where the deprojection uncertainties are minimized, indicates that such declines are a *generic feature* of $\sim M^*$ early-type galaxies (A. Romanowsky et al., in preparation).

This conclusion includes NGC 2768, which from the current data appears consistent with a constant or rising outer rotation velocity, but which with more extensive new PN data may have a declining outer profile. Even the cases of strongly rising rotation-velocity profiles out to $x \sim 2 a_e$ found by Rix et al. (1999) appear upon closer inspection to turn over at larger radii. These results all contrast with early claims of high outer rotation in some early-types, which were recently overturned with improved observations (e.g., Arnaboldi et al. 1994; Kissler-Patig & Gebhardt 1998; Romanowsky 2006; McNeil et al. 2010; Strader et al. 2011).

We can also begin making some interesting inferences about the relations among other galaxy types, based on both size and rotation-velocity trends (Figures 11 and 12). As discussed, the lenticulars share similar properties to spirals in some cases, and to ellipticals in others. The distinction between “fast” and “slow” rotator ellipticals based on their inner regions does not appear to hold up when considering their global rotation properties.

This overview of the observable scaling relations between mass, size, and rotation velocity gives us a preview of some of our overall conclusions about angular momentum, and provides more confidence in the solidity of those conclusions. We construct a novel mass–rotation velocity relation for ellipticals, which is the analogue of the Tully-Fisher relation for spirals, but with the remarkable difference of having a negative slope. The data also imply that both elliptical galaxies and spiral bulges must have lower specific angular momenta than spiral disks of the same mass. We address this issue more quantitatively in the next section, incorporating the additional mass-dependent factor k_n in calculating j_* .

5. OBSERVATIONS: ANGULAR MOMENTA OF THE FULL SAMPLE

Having derived estimates of the j_* and M_* parameters for our full galaxy sample, we now examine the resulting observational trends, which constitute the key results of this paper. We begin by focusing on the late-type galaxies in Section 5.1, and combine these with the early-types in Section 5.2. We discuss our proposed replacement for the Hubble sequence in Section 5.3, which we test by

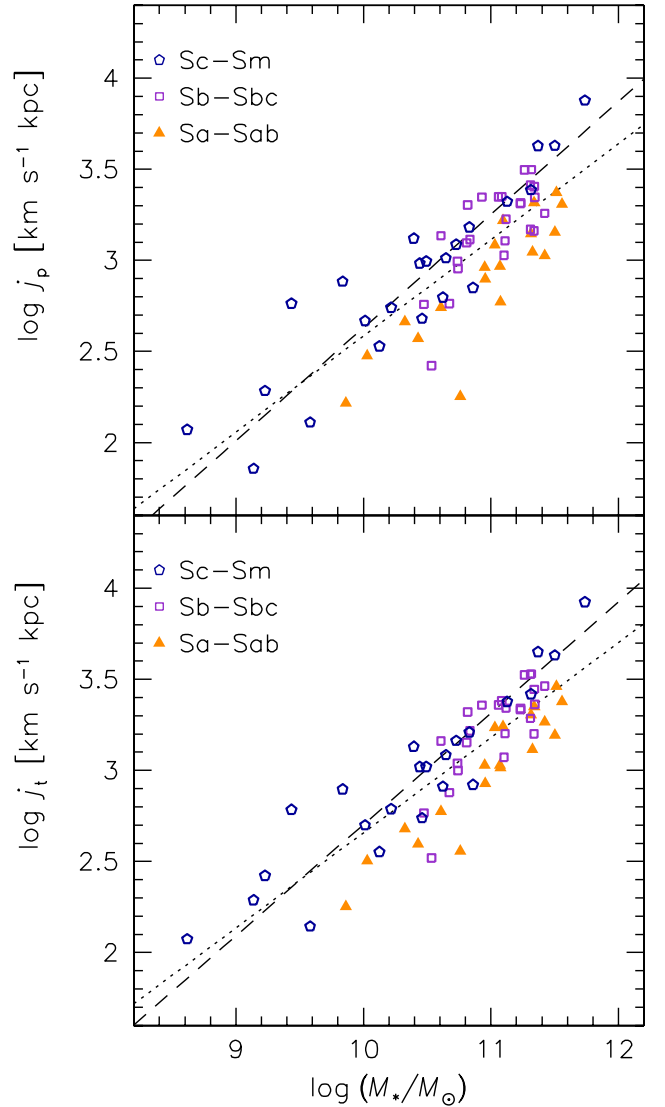


FIG. 13.— The total (disk plus bulge) stellar specific angular momentum of nearby spiral galaxies plotted against total stellar mass. The top and bottom panels show estimates of projected and intrinsic j_* , respectively; the uncertainty in j_* for each galaxy is in almost all cases smaller than the plotted symbols. Different symbols denote galaxy sub-types as specified in the legends. The dotted lines show fits to the data in each panel, while the dashed lines show fits to the disk components alone (data not shown). The spiral galaxies follow a universal j_*-M_* relation, with some dependence on Hubble type. The projected relation is very similar to the intrinsic relation, but with a small offset, and slightly increased scatter, in j_* .

examining systematic residuals from the j_*-M_* trends in Section 5.4. We further convert the j_*-M_* data into one-dimensional histograms in Section 5.5.

5.1. Lessons from spirals

Although the main novelty of this paper is our careful consideration of early type galaxies, we also include the oft-studied category of spirals in order to provide an integrated analysis of bright galaxies of all types. Furthermore, the well-constrained angular momenta of the spirals also permit us to better understand systematic issues such as inclination corrections that are trickier to handle for early-types.

We plot the total (disk+bulge) j_*-M_* data for the spi-

TABLE 2
MASS-ANGULAR MOMENTUM FITS TO DATA

Sample	$\log j_0$	α	$\sigma_{\log j_\star}$
All spirals, total, projected	3.11 ± 0.03	0.53 ± 0.05	0.22
All spirals, total, intrinsic	3.18 ± 0.03	0.52 ± 0.04	0.19
Sa–Sab, total, projected	2.93 ± 0.05	0.60 ± 0.06	0.17
Sa–Sab, total, intrinsic	3.02 ± 0.04	0.64 ± 0.07	0.12
Sb–Sbc, total, projected	3.15 ± 0.03	0.65 ± 0.14	0.16
Sb–Sbc, total, intrinsic	3.21 ± 0.03	0.68 ± 0.13	0.15
Sc–Sm, total, projected	3.25 ± 0.04	0.58 ± 0.06	0.20
Sc–Sm, total, intrinsic	3.29 ± 0.04	0.55 ± 0.05	0.18
All spirals, disks, projected	3.25 ± 0.02	0.62 ± 0.05	0.20
All spirals, disks, intrinsic	3.31 ± 0.02	0.61 ± 0.04	0.17
Sa–Sab, disks, projected	3.25 ± 0.05	0.76 ± 0.09	0.21
Sa–Sab, disks, intrinsic	3.34 ± 0.04	0.82 ± 0.08	0.17
Sb–Sbc, disks, projected	3.24 ± 0.03	0.71 ± 0.14	0.16
Sb–Sbc, disks, intrinsic	3.30 ± 0.03	0.75 ± 0.12	0.13
Sc–Sm, disks, projected	3.29 ± 0.05	0.61 ± 0.07	0.21
Sc–Sm, disks, intrinsic	3.33 ± 0.05	0.57 ± 0.05	0.19
All spirals, bulges, projected	2.20 ± 0.31	0.69 ± 0.11	0.58
All spirals, bulges, intrinsic	2.32 ± 0.31	0.69 ± 0.10	0.57
Sa–Sab, bulges, projected	2.30 ± 0.32	0.99 ± 0.15	0.47
Sa–Sab, bulges, intrinsic	2.44 ± 0.32	0.99 ± 0.15	0.46
Sb–Sbc, bulges, projected	1.89 ± 0.34	0.34 ± 0.20	0.58
Sb–Sbc, bulges, intrinsic	2.01 ± 0.33	0.34 ± 0.19	0.56
Sc–Sm, bulges, projected	2.21 ± 0.57	0.64 ± 0.27	0.60
Sc–Sm, bulges, intrinsic	2.30 ± 0.58	0.63 ± 0.28	0.60
Lenticulars, projected	2.97 ± 0.08	0.80 ± 0.14	0.29
Lenticulars, intrinsic	3.05 ± 0.08	0.80 ± 0.14	0.29
Ellipticals, projected	2.52 ± 0.05	0.60 ± 0.09	0.24
Ellipticals, intrinsic	2.73 ± 0.05	0.60 ± 0.09	0.24
Sb–Sm, intrinsic, fixed $\alpha = 2/3$	3.28 ± 0.03	0.67	0.19
Ellipticals, intrinsic, fixed $\alpha = 2/3$	2.75 ± 0.05	0.67	0.24
Λ CDM halos	2.50	0.67	0.23

als from Table C4 in Figure 13. In the top panel, we show the projected value, j_p , and in the bottom panel, the intrinsic value, j_t . These are related trivially by the disk inclination, but we wish to investigate how well the trends in projection reflect the intrinsic trends, since deprojection for the early-type galaxies will be more difficult.

Overall, the spiral galaxies appear to follow fairly tight $j_\star-M_\star$ trends, with similar slopes, regardless of Hubble sub-type. In more detail, we carry out least-square fits to j_\star as a function of M_\star in log-log space:

$$\log j_{\text{mod}} = \log j_0 + \alpha [\log(M_\star/M_\odot) - 11], \quad (11)$$

with a residual rms scatter that we parameterize as $\sigma_{\log j_\star}$. The uncertainties in the fit parameters j_0 and α are estimated by bootstrap resampling.

Our fitting results for various spiral subsamples are reported in Table 2. For total j_\star , the systematic uncertainties from the bulge rotation (see Section 4.1) turn out to be smaller than or equal to the statistical fitting uncertainties, even for the Sa–Sab galaxies, and in the Table we have combined both uncertainties in quadrature.

The data are basically consistent with a universal $j_\star-M_\star$ slope for spiral galaxies of all types, with $\alpha \sim 0.6$ and an rms scatter of $\sigma_{\log j} \sim 0.2$ dex. There is also a clear residual trend with Hubble type: the Sa–Sab galaxies have systematically lower j_\star than the Sb–Sm galaxies. These conclusions hold for both j_p and j_t , although the uncertainties and the scatter are smaller for j_t , as

expected if there are genuine, underlying physical correlations that become clearer after deprojection.

The multi-component nature of our model galaxies allows us to look further at disk and bulge properties separately. We will take up this issue in Section 5.2, and for now provide the fits to the j_d-M_d and j_b-M_b relations in Table 2. It should be remembered that the bulge results depend on model assumptions, although as discussed, we have plausibly bracketed their upper and lower limits for j_\star .

As anticipated, the bulges turn out to have little impact on the total j_\star trends for the Sb–Sm galaxies, which are dominated by the disk components. For the Sa–Sab galaxies, the bulges are responsible for the systematic offset with respect to the later types; this offset changes slightly but persists when adopting the upper or lower limits to the bulge rotation. The *disks* of all the galaxy types turn out to follow nearly the same $j_\star-M_\star$ relations.

This analysis demonstrates that inclination effects are not expected to have a major impact on our overall results, since for both disks and bulges, the intrinsic and projected $j_\star-M_\star$ trends as well as their scatter are very similar. There is an overall offset between disk j_t and j_p of ~ 0.07 dex, which is comparable to the range of 0.04–0.06 dex that we would expect, given the median inclination $i = 67^\circ$ of our sample, and depending on whether the $j_\star-M_\star$ trend represents a median or an average fit (see Appendix A.2 for further discussion).

For our ensuing study of early-type galaxies, we will therefore simply adopt median deprojection values for all of the galaxies, which we estimated in Section 4.2 to mean adding offsets of 0.08 dex and 0.22 dex to j_p to derive j_t , for lenticulars and ellipticals, respectively. We can also in general drop the usage of j_p in the rest of this paper, in favor of the more physically meaningful j_t which we now adopt as our estimate for j_\star .

5.2. Combined observational results

We are now ready to include the early-type galaxies in our analysis, and thereby address most of the key science questions raised in Section 1. As a reminder, our starting point is the $j_\star-M_\star$ diagram from F83 that we have reproduced in Figure 1. Do we find the same $j_\star-M_\star$ trends with an updated and expanded dataset, and more detailed analysis? Do ellipticals still appear to have systematically low j_\star relative to spirals, or do we discover large reservoirs of additional j_\star at large galactocentric radii, using modern data? Do Sa and S0 galaxies fill in any “gap” between spirals and ellipticals, and can we then connect the Hubble sequence to a sequence in j_\star ? Can we characterize all galaxies as combinations of disks and bulges that follow universal scaling relations? (The main remaining question that connects to galaxy formation theory will be pursued in the next section.)

Taking our early-type galaxy j_\star and M_\star estimates from Table C5 (after statistically correcting projected to intrinsic quantities; see Table 1 for an error analysis), we plot them in Figure 14 (left), along with the spirals results discussed in Section 5.1. This new Figure is the centerpiece of our paper. *Focusing first on the elliptical galaxies, our basic finding is that they follow a $j_\star-M_\star$ trend which is roughly parallel to the spirals but with a large systematic offset to lower j_\star .*

We thereby confirm the conclusions of F83, finding

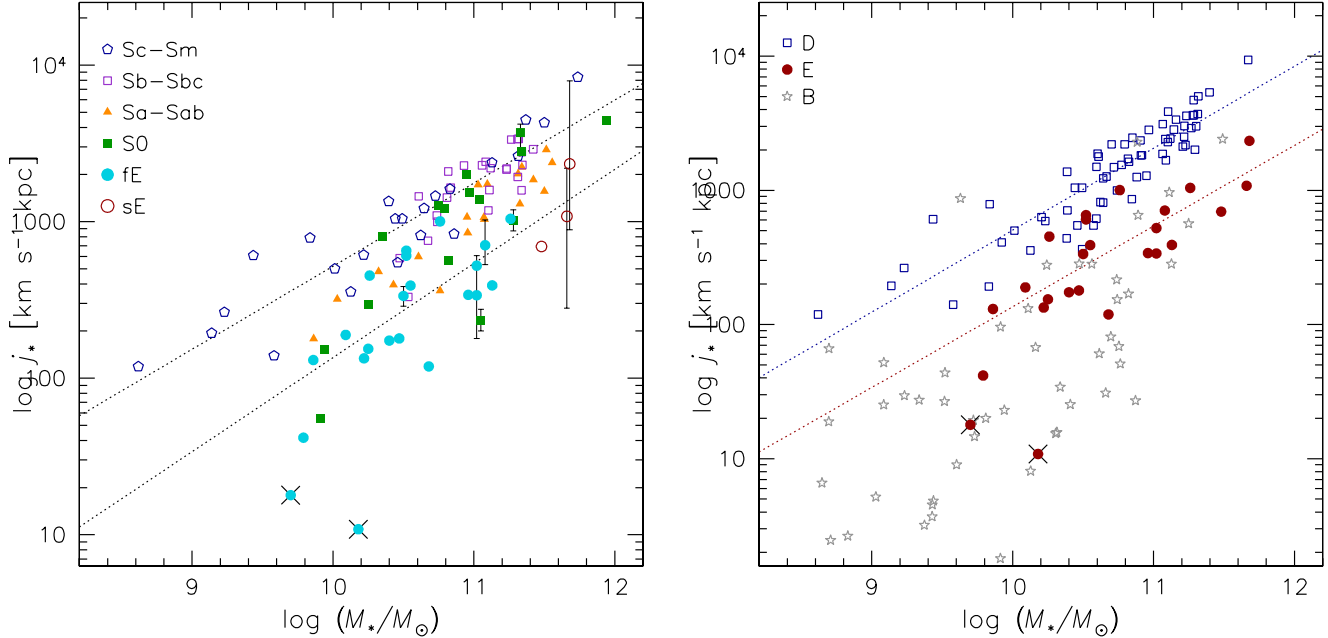


FIG. 14.— *Left-hand panel:* The total intrinsic specific angular momentum of galaxies plotted against their total stellar mass. Symbols show galaxy types according to the legend at the upper left. The points with error bars shown are based on the more detailed j_* estimator [Equation (3)]; for the remainder of the galaxies, the approximate j_* estimator [Equation (6)] was used. The uncertainties are similar in both cases. The deprojection from observed j_p to intrinsic j_t was accomplished using individual inclinations for the spirals, and median deprojection factors for the lenticulars and ellipticals (see main text). The least massive early-type galaxy in the sample is the compact elliptical NGC 4486B, which is probably in the process of being tidally stripped by the giant galaxy M87; the other low- j_* outlier is NGC 1419. Both are marked with black \times symbols and excluded from all fits in this paper. Dotted lines show the best fits for the Sb–Sm and elliptical galaxies: these two galaxy types follow j_* – M_* trends that are parallel but separated in j_* by ~ 0.5 dex. *Right-hand panel:* As left-hand panel, but now plotting spiral disks and bulges alone, along with elliptical galaxies, as indicated by the legend. The upper line is now the fit to the disks (for all spiral types) rather than to the whole galaxies. Note that the slopes of the lines in this panel and the left-hand one should not be compared by eye, owing to the different axis ranges. The uncertainties in j_* for the disks are typically ~ 0.04 dex, and for the bulges at least ~ 0.2 dex; the M_* uncertainties are systematic (see main text). Many of the most massive spiral bulges appear to follow a similar j_* – M_* relation to the ellipticals.

from a new synthesis of modern photometric and kinematic data that the “missing” angular momentum in ellipticals does *not* emerge at large radii, as had been expected from some theoretical studies. As discussed in Section 4.3, the new observations tend to show outer rotation profiles that *decline* rather than rise. Even the nearby galaxy NGC 5128 (Cen A), which is often considered to be an elliptical formed through a recent major merger, shows a relatively low j_* when compared to spirals of the same stellar mass. Whether or not these observations pose a genuine problem to major-merger explanations for forming ellipticals will require renewed theoretical analysis, but as discussed in Section 4.3, there seems to be a pattern in the literature of misdiagnoses of high outer rotation from early, sparse data – which led to premature claims of evidence for major mergers.⁶

The specific angular momentum difference between spirals and ellipticals is also apparent from a simple, direct consideration of the data in Section 4.3, where the smaller sizes and rotation velocities for ellipticals sug-

gested that they have lower j_* . As an arbitrary benchmark, we use the median j_* at the L^* characteristic luminosity, which is $\log(L_K^*/L_{K,\odot}) \sim 11$, corresponding to $\log(M_*/M_\odot) \sim 11$. For ellipticals and Sb–Sm spirals, we find projected values of $j_p \sim 330$ km s^{−1} kpc and ~ 1600 km s^{−1} kpc, respectively, and true values of $j_* = j_t \sim 540$ km s^{−1} kpc and ~ 1800 km s^{−1} kpc.

In more detail, we report fits to the j_* – M_* data toward the end of Table 2. The fitted slope for the ellipticals is consistent with that for the Sb–Sm spirals, but is significantly offset to lower j_* by a factor of ~ 3.4 (~ 0.5 dex). These findings are consistent with F83, except that the gap has narrowed from a factor of ~ 6 (~ 0.8 dex).⁷ Note that if the K -band Υ_* for the ellipticals were systematically higher than for the spirals by a factor of ~ 2 (perhaps owing to age or IMF differences; cf. Section 3.4), then the j_* offset would increase to a

⁶ Norris et al. (2012) also recently noted an emerging trend for low rotation in elliptical-galaxy halos, at odds with major-merger expectations. One possible counter-example is the S0 galaxy NGC 1316, which is generally thought to be a major-merger remnant. Based on the new PN kinematics results from McNeil-Moylan et al. (2012), we confirm the finding of Arnaboldi et al. (1998) that the j_* – M_* values for this galaxy are close to the mean trend for spirals. However, we caution that our photometric parameters and Υ_* value are particularly insecure for this galaxy.

⁷ Our revised Sb–Sm relation is ~ 0.1 dex lower than in F83, partly owing to the inclusion of bulges, and partly to new estimates for disk sizes and mass-to-light ratios. Our revised ellipticals relation is ~ 0.2 dex higher than in F83; this difference appears to arise not so much from the rotation data (the extrapolations to large radius by F83 turn out very good on average), but from a refined treatment of the total angular momentum calculation for spheroids. Our slopes of $\alpha = 0.53 \pm 0.04$ and 0.60 ± 0.09 for the Sb–Sm and elliptical galaxies are shallower than the $\alpha = 0.75$ slope suggested by F83; for the Sb–Sm galaxies, this difference is driven mostly by our inclusion of bulges and of lower-mass galaxies [$\log(M_*/M_\odot) \sim 9$]; while for the ellipticals, a shallower slope was already apparent in F83.

factor of ~ 5 (~ 0.7 dex).

The scatter of $\sigma_{\log j_\star} = 0.24$ dex for the ellipticals is similar to the j_p scatter for the spirals. We also note that the general trends for the ellipticals are supported by the small sample of galaxies that we modeled in detail (see points with error bars in Figure 14, left). Although one might still have concerns that large formal uncertainties in j_\star remain for most of the sample after extrapolating their rotation-velocity profiles beyond $2 R_e$, in order to close the j_\star gap between spirals and ellipticals, the rotation velocity would have to rise rapidly by a factor of ~ 4 outside these radii, which seems implausible (cf. Figure 6).

The parallel nature of the spiral and elliptical trends is an interesting and non-trivial result, since Figure 12 showed that the slopes of the rotation-velocity scaling relations for these galaxies have opposite signs. Some mass-dependent conspiracy of size, rotation velocity, and Sérsic index must be at work in order for the j_\star - M_\star slopes to turn out the same.

The few “slow rotator” ellipticals in our sample show no indication of deviating systematically from the overall j_\star - M_\star trend for ellipticals, which disagrees with earlier findings of much lower j_\star for such galaxies (Bender & Nieto 1990). Although their outer regions, like their central parts, rotate slowly relative to most of the fast rotators (Figure 12), we find that this is compensated for by their larger scale radii and Sérsic indices (keeping in mind that the results for these galaxies are the most uncertain). Thus the global j_\star measurements suggest that the slow and fast rotators may have more in common than was previously suspected.

Having confirmed the basic observational findings of F83, we now move on to fresh territory, beginning with the inclusion of Sa and S0 galaxies in Figure 14 (left). F83 suggested that these would fill the gap in j_\star - M_\star space between ellipticals and late-type spirals, which is confirmed by our sample. Both of these galaxy types are on average offset to lower j_\star from the Sb–Sm spirals trend by a factor of ~ 1.8 (~ 0.25 dex; we will discuss variations about the average in Section 5.4).

One natural interpretation of this new finding is that the Hubble classifications are related to an underlying physical structure, where all galaxies are composed of some combination of two basic components: a disk and a spheroid (as illustrated schematically in Figure 2 of Section 1). These components would define two distinct sequences in the j_\star - M_\star plane, which in combination would move the total values of galaxies to intermediate regions in this plane, depending on the bulge-to-total mass ratios, B/T .

To explore this idea, we plot the j_\star - M_\star data separately for elliptical galaxies, and for spiral disk and bulge subcomponents, in the right-hand panel of Figure 14. The disks follow a similar relation to spiral galaxies overall, since these are dominated by their disks. More remarkably, the j_\star - M_\star trend for *bulges* is fairly similar to the trend for ellipticals over the mass range where they overlap.⁸ This is a surprising result, because as shown in Fig-

⁸ At lower bulge masses, the apparent tendency to relatively low j_\star values should be viewed as speculative, since it is based on classical bulges rather than the pseudo-bulges that may predominate in this regime.

ure 11, the bulge *sizes* are systematically smaller than the ellipticals, and thus their rotation velocities (Figure 12) must be higher, in an apparent conspiracy to produce roughly the same j_\star .

A similar analysis could in principle be carried out for the fast-rotator ellipticals, since they are widely considered to host hidden, embedded disk-like components. Do the disk and bulge subcomponents of ellipticals follow the same j_\star - M_\star relations as those of the spirals? We have investigated this question in Appendix D using decompositions from the literature, but the results are somewhat ambiguous. Thus, although we have been able to address all of the major questions raised initially about empirical j_\star - M_\star trends, we flag the trends for the subcomponents in ellipticals (and lenticulars) as an important aspect remaining in need of clarification.

5.3. Replacing the Hubble diagram

The foregoing discussion brings us to the diagram that we have already introduced schematically with Figure 2, which constitutes our own, physically-motivated, substitute for the classic Hubble tuning fork, and which could provide the underlying explanation for the observational trends found in Figure 14. In this scheme, all galaxies are composed of a disk and a bulge, each adhering to a distinct and parallel j_\star - M_\star scaling relation. If the disk and bulge relations are universal (which we will further test in Section 5.4), then the location of a galaxy in j_\star - M_\star space can immediately be used to infer its B/T value uniquely, and vice-versa (i.e., there is a coordinate transformation between the two parameter spaces). Elliptical galaxies would then be the cases with $B/T \sim 1$, and bulges could be thought of as mini-ellipticals.

As with the original Hubble diagram, our j_\star - M_\star diagram provides a simple *description* of galaxies, along with the temptation to interpret it as some kind of *evolutionary sequence*. However, our diagram differs, since the parameters used are physical quantities that may in principle be conserved, and thus it is actually justified to begin using the diagram directly as a tool to motivate and test some evolutionary scenarios for galaxies. This will be the objective of Section 6.

A key feature of our diagram is that it views galaxies as fundamentally populating a space of *two parameters*, angular momentum and mass, which are nearly equivalent to the more observationally accessible properties of bulge fraction and luminosity. In this framework, galaxies *cannot* be fruitfully reduced to a one-dimensional family controlled by a single parameter (e.g., Disney et al. 2008).

Our diagram may also be contrasted with another currently fashionable way to understand galaxies: as color-magnitude sequences that are generally related to star formation histories (e.g., Baldry et al. 2004; Faber et al. 2007). These properties are loosely related to j_\star - M_\star space if star formation generally occurs in high- j_\star disks. However, our framework is less astronomical and more astrophysical in nature, and we expect it to provide novel insights to galaxy formation that are complementary to other classifications, and perhaps more fundamental.

Another recently-introduced classification for galaxies is also based loosely on specific angular momentum concepts: λ_R (Emsellem et al. 2007), which measures the rotational dominance in the central regions (typically inside $\sim R_e/2$) and is similar to a v/σ metric. Applied

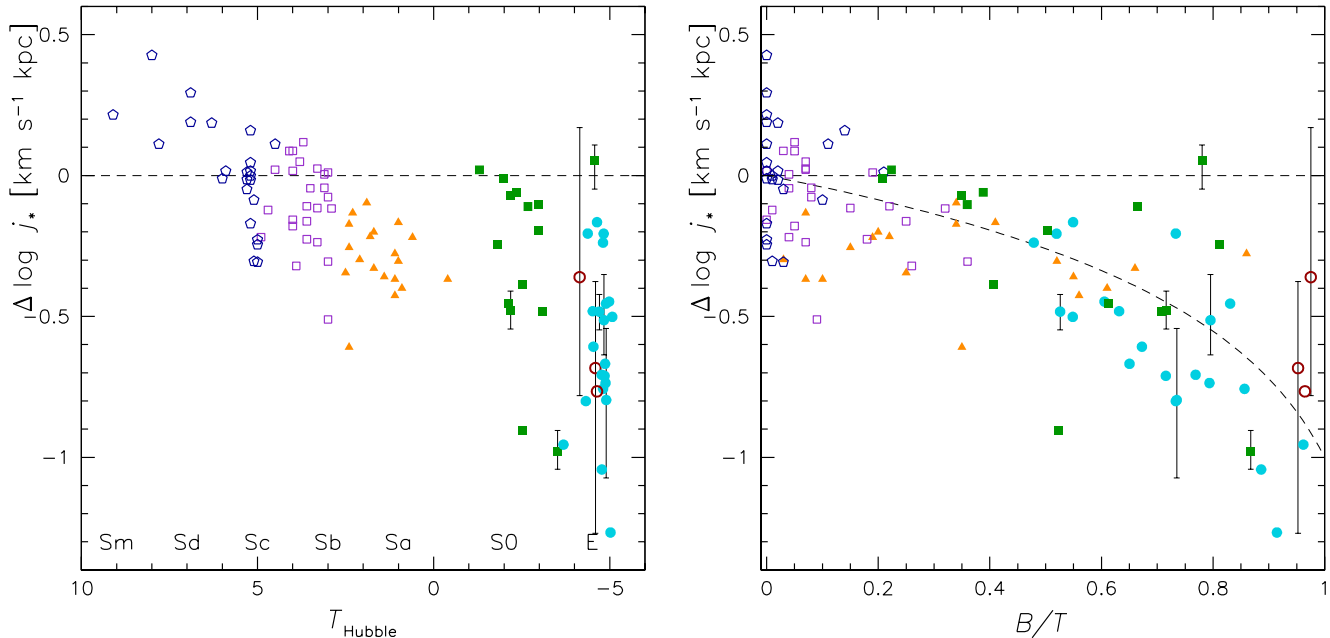


FIG. 15.— Specific angular momentum relative to the best-fitted trend for spiral disks. In the *left-hand panel*, these residuals are plotted vs. Hubble stage. For clarity, small random offsets have been added in the horizontal direction for the early-type galaxies. In the *right-hand panel*, the residuals are plotted vs. bulge-to-total mass ratio. The curved line shows a sample model prediction (not a fit to the data; see text for details). There are strong systematic trends of the j_* residuals with respect to both Hubble type and to bulge-fraction, and the relative smoothness of this trend (particularly for the E/S0s) suggests that bulge-fraction is the more fundamental driving parameter.

to early-type galaxies, a host of interesting patterns and correlations have emerged (Emsellem et al. 2011). However, this metric in practice is not only very scale dependent, but also misses exactly those scales that are most important for measuring true, physical angular momentum (recall Figure 3). In fact, we have seen evidence that j_* and the central λ_R are disjoint properties: the slow rotators (low- λ_R galaxies) do not appear to deviate from the j_*-M_* trend for fast rotators.

A final related diagram to mention is j_*-v_c , where v_c is the circular velocity, tracing the dynamical mass of a galaxy within some characteristic radius (e.g., Navarro & Steinmetz 2000; Kassin et al. 2012). There are complications with using this parameter space, since for spiral galaxies both j_* and v_c are normally based on the same rotation-velocity measurements, which causes a built-in correlation. Unlike M_* , v_c is not a physical quantity subject to straightforward conservation laws. In addition, a critical point for our goal of analyzing all types of galaxies in a unified manner is that it is very hard to estimate v_c for a large sample of early-types since they rarely host extended gas disks. Instead, extensive data are required from other tracers such as stellar kinematics (as needed for j_* estimation), as well as grueling dynamical modeling which even with the state-of-the-art techniques can still leave considerable uncertainties (de Lorenzi et al. 2009). Similar problems apply to a j_*-M_{vir} (virial mass) diagram, where the masses can be estimated only on a statistical rather than on an individual basis (e.g., Dutton & van den Bosch 2012).

5.4. Examining the residuals

Our bulge-disk framework, although rather compelling, is not a unique explanation for the systematic trends in the left-hand panel of Figure 14. It is possi-

ble that the vertical displacements of j_* in this diagram are somehow more directly related to Hubble morphology than to B/T (although one should keep in mind that B/T is one of the main factors in the morphological classifications, along with spiral arm winding and clumpiness).

To consider this point more clearly, and to better see the relative trends in the data, we flatten the j_*-M_* relations into one dimension, dividing by the mean trend for the spiral disks and thus generating the quantity:

$$\Delta \log j_* \equiv \log j_* - \log j_{\text{mod}}(M_*), \quad (12)$$

where j_{mod} is given by Equation (11). We plot $\Delta \log j_*$ versus the Hubble stage parameter T_{Hubble} in Figure 15 (left-hand panel). There is clearly a strong positive correlation between T_{Hubble} and the j_*-M_* residuals. Among the spirals, this trend is clearest when considering the Sa-Sab versus Sb-Sc galaxies. The Scd-Sm galaxies appear to continue the trend, but they inhabit the lowest-mass area of the j_*-M_* diagram, where the mean relation is not defined well enough to be certain of the residuals.

The S0s break the smooth trend of $\Delta \log j_*$ decreasing for smaller T_{Hubble} . Many of them appear to have comparable specific angular momenta to typical Sb-Sc galaxies, which was foreshadowed by the rotation scaling relations of Figure 12. The implication is that lenticulars and spirals are overall dynamically similar, differing more in their finer morphological features which may be related to star formation activity. We can thus think of these lenticulars as faded spirals, or of the spirals as rejuvenated lenticulars, although they differ in average B/T values, and more nuanced comparisons will require analysis of Υ_* (cf. Williams et al. 2010). As for the subset of lenticulars with low $\Delta \log j_*$, they may either be very close to face-on, or else belong to a different family of

objects that are related to the ellipticals.

Returning to our original hypothesis that B/T is the key parameter affecting the $j_\star-M_\star$ trends, we consider its correlation with the residuals $\Delta \log j_\star$. Since we do not actually have bulge/disk decompositions for the early-type galaxies in our sample, we introduce a novel technique that uses the degree of central rotational support as a rough proxy for B/T . The idea here is that the bulge is to a first approximation non-rotating, so any observed rotation is from the disk: objects with higher (v/σ) imply higher disk fractions and lower B/T . Appendix D describes our methods for early-type B/T estimation in more detail. For the late-types, we already have B/T estimates based on decompositions in the literature, as discussed earlier.

We show the results in the right-hand panel of Figure 15. The residuals *do* correlate clearly with B/T , in a fairly smooth trend that is followed equally well by all of the galaxy types, and which contrasts with the T_{Hubble} trend. We have marked a simple expectation for the B/T trend with the curved line, given the summation of Equation (9), along with an arbitrarily assumed $j_b = 0.1 \times j_d$. This model mimics the data remarkably well, although it should be remembered that the agreement is somewhat built-in already, since correlated rotational properties were used both to estimate B/T and to calculate j_\star .

Recalling that we also had to make strong modeling assumptions for the spiral bulges when calculating j_\star , the better connection of the residuals to B/T rather than T_{Hubble} should be considered preliminary. It is also difficult to tell how much of the scatter in j_\star at fixed B/T is due to observational error, and how much is due to intrinsic variations, i.e., with bulges and/or disks not following perfectly standardized $j_\star-M_\star$ relations. Definitive resolution of these issues will require more detailed bulge-disk decompositions of all types of galaxies, including spectroscopic information (cf. Cortesi et al. 2011; Johnston et al. 2012; Dorman et al. 2012; Forbes et al. 2012), and allowances for Υ_\star variations.

We would however like to advance the proposition that bulge fraction is the fundamental driving parameter behind j_\star variations, and is responsible for many of the observed variations in galaxy properties (see discussion in previous subsection). Not only does this make sense from a physical standpoint, but the agreements between ellipticals and spiral bulges in Figure 14 (right), and between model and data in Figure 15 (right), provide provisional but strongly suggestive observational support. The radially-declining rotation-velocity profiles of galaxies like NGC 821 and NGC 3377 in Figure 6 could also be naturally explained by central disk components embedded in non-rotating bulges. Furthermore, we will see from consideration of a cosmological context in Section 6.2 that the distribution of j_\star is more naturally reconciled with distinct disk and spheroid subpopulations than with a simple continuum of galaxy j_\star .

5.5. Histograms of stellar j residuals

Before moving on to theoretical analyses, we construct one more representation of the data whose relevance will become particularly clear in the next section. We compress the preceding $j_\star-M_\star$ information into a histogram of residuals from the spiral disk relation, showing the

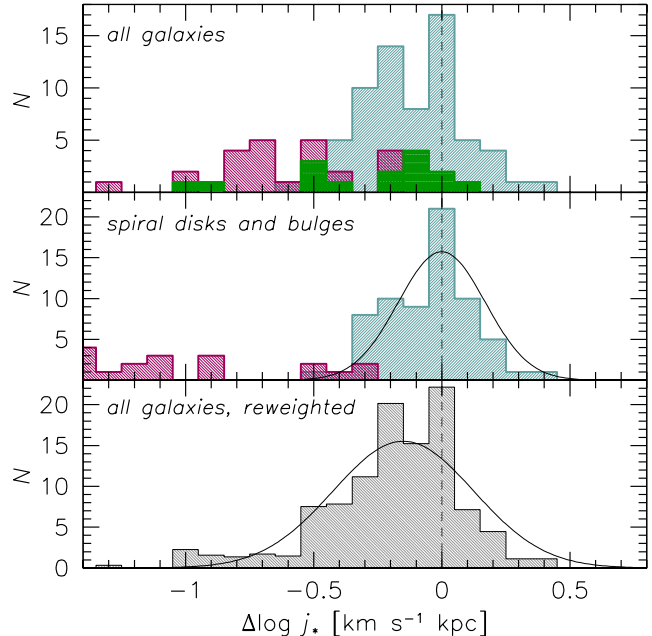


FIG. 16.— Histogram of specific angular momentum relative to the mean observed trend for spiral disks. In two of the panels, curves show example lognormal distributions for comparison to the data. In the upper panel, the red, green, and blue histograms show data from Figure 15 for spirals, lenticulars, and ellipticals, respectively. The middle panel shows the bulge and disk subcomponents of spiral galaxies, with red and blue histograms, respectively. The lower panel is a summation of the data from the upper panel, after renormalizing each galaxy sub-type by its frequency in the nearby universe (see main text). The specific angular momentum does not appear to have a simple lognormal distribution, and may even be bimodal.

results in Figure 16 (upper panel). Here it is apparent that the spiral galaxy data comprise a roughly lognormal distribution in $\Delta \log j_\star$, with an rms dispersion of ~ 0.2 dex. The ellipticals have a less well-defined distribution that partially overlaps the spirals but is offset ~ 0.5 dex lower, while the small sample of lenticulars spans almost the full range of residuals.

In the middle panel of Figure 16, we look instead at the disk and bulge subcomponents of the spiral galaxies, where we have also overplotted a Gaussian with a width of $\sigma_{\log j_\star} = 0.17$ dex for reference. Given the uncertainties and possible selection bias in our analysis, we consider the disks to be reasonably consistent with a lognormal distribution.

The $\Delta \log j_\star$ distribution for the spiral bulges resembles that of the ellipticals in the sense that both are systematically offset to lower values, as we have previously seen. The bulges apparently extend to much lower $\Delta \log j_\star$ than the ellipticals, but as discussed in Section 5.2, this is not a secure result, given the uncertainties in the bulge calculations.

Returning to the overall results, we would like to know whether or not galaxies follow a bimodal distribution in $\Delta \log j_\star$ as the top panel of Figure 16 suggests. The complication here is possible bias in the galaxy sample: if we were to study *all* bright galaxies in a volume-limited sample, the $\Delta \log j_\star$ distribution might look very different. To investigate this issue, we must re-weight the distribution of j_\star in our sample by galaxy type.

The simplest approach is to renormalize by frequency or number density. We use the ATLAS^{3D} results that 70%, 22%, and 8% of the galaxies in the nearby universe are spirals, lenticulars, and ellipticals (over a stellar mass range similar to our observational sample; Cappellari et al. 2011a). The fractions in our sample are 63%, 14%, and 23%, demonstrating a strong bias toward ellipticals at the expense of lenticulars.

We plot the re-weighted results in the lower panel of Figure 16, showing also for reference a lognormal curve with $\sigma_{\log j_\star} = 0.27$ dex (a width that will be motivated in Section 6.2). The total distribution of $\log j_\star$ residuals appears slightly non-Gaussian, with a tail extending to low values. This feature may not be significant if one allows for systematic uncertainties in the selection effects, but the skewness will become clearer when compared to theory in Section 6.2.

An alternative scheme would be to re-weight by the stellar mass density of the different galaxy types. This would bring us closer to a total distribution function for stellar j in the universe, rather than a distribution of galaxies with given j_\star . It is beyond the scope of this paper to carry out such an exercise in detail, but the basic outcome is clear. The high end of the mass distribution is dominated by early-types (cf. lower panel of Figure 33), which means that the mass weighting would enhance the contributions of these galaxies relative to number weighting. The universal distribution of j_\star would then appear *more non-Gaussian* than in the lower panel of Figure 16.

We therefore find evidence that the residuals of the specific angular momenta of galaxies from the mean relation are not simply lognormal. The best match to a lognormal model is provided by the disk components of spirals, while the bulges and the ellipticals may comprise a distinct second population.⁹ Again, a natural interpretation of this finding is that all galaxies are composed of some combination of high- and low- j_\star material, which may be identified with disks and bulges, respectively.

Some implications of these results for galaxy formation in a modern cosmological context will be discussed in the next section. It should be remembered, however, that our empirical findings—of specific, strong correlations between galactic angular momentum, mass, morphology, and bulge fraction—stand on their own and must be explicable by any successful theory of galaxy formation, whether now or in the future.

6. CONNECTING TO THEORY

We are now ready to present a fresh theoretical way of looking at galaxies, using the j_\star - M_\star diagram, which was introduced in F83, and which may now be reinvigorated by populating it with observational data for galaxies of all types. Our general approach is to take a step back from galactic *details*, whether these be spiral arms and dust lanes in observations, or unresolved gas physics and star formation recipes in simulations, and return to some simple physical parameters and conservation rules that may provide robust constraints and insights to galaxy formation.

⁹ Hernandez et al. (2007) used a large photometric survey to estimate j_\star indirectly, with results that are less accurate than those presented here, but which similarly imply a bimodal distribution for ellipticals and spirals.

We have shown in Sections 5.2 and 5.4 that the specific stellar angular momenta of observed galaxies follow remarkably tight correlations with their masses and bulge fractions. Such patterns in Nature demand theoretical explanations, as they could be tracing fundamental physical processes. Indeed, the j_\star - M_\star relation for spiral galaxies is well known in some circles, and provides a crucial benchmark for models of galaxy formation. However, the correlation for elliptical galaxies (already shown in a preliminary version by F83) is less well known and addressed with theoretical models. Our goal is to advance a general, physical framework for integrating these observational constraints into models of galaxy formation and evolution.

Our approach here is different from, and complementary to, the active field of hydrodynamical simulations of galaxy formation. Although such simulations have made notable progress toward the ultimate goal of reproducing realistic galaxies, they still have a long way to go, with recent work highlighting large differences in the basic properties of simulated galaxies, depending on what code, resolution, and physical recipes are used (Scannapieco et al. 2012; Torrey et al. 2012).

Historically, such methods missed reproducing observed j_\star trends by factors of up to ~ 30 , and even the most recent work shows variations at the factor of ~ 2 level. The general concern is that many of the large-scale properties of galaxies could well depend strongly on transport processes at the scales of molecular clouds, which are not yet modeled satisfactorily in cosmological simulations. Therefore some caution is still needed in assuming that the simulations are providing an adequate representation of reality.

In this context, simplified “toy” models continue to play a key role in defining the broad but solid outlines of the galaxy formation theory that is required to match the observational constraints. These models may also prove useful in physical understanding of the output of numerical hydrodynamical simulations.

We frame our analysis in the context of the current standard cosmological model for structure formation: cold dark matter with a cosmological constant (Λ CDM; Komatsu et al. 2011). This model makes specific, robust predictions for the angular momenta of DM halos. Because the visible galaxies, consisting of stars and gas, are presumed to reside in these DM halos, we may then ask whether or not the observed stellar angular momenta bear any resemblance to the predictions for DM halos.

We begin with the properties of Λ CDM halos as our “initial conditions” for galaxy formation, which we map to our observable space: j_\star - M_\star for the stellar components of galaxies. We do this by parameterizing the retention of mass and angular momentum during galaxy formation, and then by introducing a menu of j_\star - M_\star vectors of change that correspond to plausible physical processes (outflows, mergers, etc.).

We emphasize that the primary aim of this paper is *not* to concoct a new theory of galaxy formation, nor to weigh in on competing models by vetting specific simulation outputs against the j_\star - M_\star diagram. Instead, we wish to lay out a generalized framework that can both constrain and explain the models. The methodology and merits of this approach should become clearer as we develop the ideas throughout this section, and as we eventually work

through some practical examples.

We develop general theoretical predictions and make basic inferences about j retention in Section 6.1. In Section 6.2 we investigate two possible explanations for the observed j_* dichotomy between spirals and ellipticals. In Section 6.3 we consider coupling between changes in mass and angular momentum, and connect these to evolutionary scenarios for galaxies.

6.1. Basic constraints

The overdense regions in an expanding universe are not spherically symmetric and exert tidal torques on each other, inducing a net angular momentum in each collapsing galaxy (Hoyle 1951). This rotational behavior is usually specified in terms of a dimensionless spin parameter that quantifies the dynamical importance of rotation, and is a combination of fundamental physical quantities:

$$\lambda \equiv \frac{J|E|^{1/2}}{GM^{5/2}}, \quad (13)$$

where J is the angular momentum, E is the energy (kinetic and potential), G is the gravitational constant, and M is the mass (Peebles 1969).¹⁰ Whether analyzed through linear tidal torque theory, or through N -body simulations of galaxy assembly, λ is predicted to follow an almost lognormal distribution that is relatively insensitive to cosmological parameters, time, galaxy mass, and environment (e.g., Barnes & Efstathiou 1987; Zurek et al. 1988; Steinmetz & Bartelmann 1995; Cole & Lacey 1996; Macciò et al. 2007).

The spin parameter provides a convenient way to characterize DM halos, but it is not straightforward to connect λ to baryonic galaxies because it is not a physically conserved quantity (as energy is dissipated). We instead conduct our theoretical analysis in terms of the specific angular momentum parameter j , as we have done with the observations. Along with the mass M , j is a quantity that is potentially conserved at some approximate level during the evolutionary history of a galaxy.

To re-cast λ to j , we adopt a Λ CDM-based spherically-symmetric halo profile from Navarro et al. (1996), truncated at the virial radius.¹¹ We then obtain:

$$j_{\text{vir}} = 4.23 \times 10^4 \lambda \left(\frac{M_{\text{vir}}}{10^{12} M_{\odot}} \right)^{2/3} \text{ km s}^{-1} \text{ kpc}. \quad (14)$$

We adopt a characteristic value¹² of $\langle \lambda \rangle = 0.035$, along with a 1σ log dispersion of 0.23 dex, based on a study of relaxed halos in a cosmological simulation with WMAP5

¹⁰ Recall that the parameters (J, E, M) can be translated roughly into a more observationally oriented basis set of rotation velocity, effective radius, and luminosity (v_{rot}, R_e, L), where in approximate terms: $M \propto L$, $E \propto L^2 R_e^{-1}$, and $J \propto v_{\text{rot}} L R_e$.

¹¹ The virial radius is defined as bounding a region inside which the mean halo density is a factor of Δ_{vir} times the critical density $\rho_{\text{crit}} \equiv 3H^2/(8\pi G)$. We adopt a WMAP5 cosmology, with $H = 72 \text{ km s}^{-1} \text{ Mpc}^{-1}$ and $\Delta_{\text{vir}} = 95.3$ at $z = 0$ (Macciò et al. 2008). To calculate E for this halo, we use an expression from Mo et al. (1998) with a fixed concentration of $c_{\text{vir}} = 9.7$; and we ignore variations due to concentration which affect λ at the $\sim 5\%$ level. A related spin-proxy parameter, λ' , is based on a singular isothermal sphere (Bullock et al. 2001), and is $\simeq 11\%$ smaller than λ .

¹² This is based on the average value of $\log \lambda$, but throughout this paper we use shorthand such as $\langle \lambda \rangle$ and $\langle j \rangle$ for log-averages.

parameters, by Macciò et al. (2008). The log-averaged numerical coefficient in Equation (14) then becomes $1460 \text{ km s}^{-1} \text{ kpc}$. Other recent studies are generally consistent with these results at the level of $\sim 10\%$. The $\alpha = 2/3$ exponent is also an explicit prediction of tidal torque theory (Shaya & Tully 1984; Heavens & Peacock 1988), and provides a reasonable approximation to the trends from *direct* calculations of j_{vir} and M_{vir} in N -body simulations (Antonuccio-Delogu et al. 2010).

Equation (14) can be considered as setting firm “initial conditions” for galaxies, characterizing their angular momenta near the time of virialization. This is shown schematically in panel (a) of Figure 17, which we have populated with toy-model “galaxies” consisting of primordial halos of gas and DM. Their masses are drawn from a uniform logarithmic distribution, and their angular momenta from a lognormal distribution using $\langle j_{\text{vir}} \rangle$ and $\sigma_{\log j_{\text{vir}}}$ as above.

We next consider a series of idealized evolutionary steps that allow us to parameterize evolution in the j - M diagram. We assume that the baryons consist initially of gas that is well mixed with the dark matter of its parent halo, and that does not collapse within the halo until after the linear and translinear regimes of tidal torque when most of the angular momentum is acquired. The gas may then be assumed to have the same value of j as the halo, which we show in panel (b) as a simple shift of the points to the left, according to a cosmological baryon fraction of $f_b = 0.17$ (Komatsu et al. 2011).

In panel (c) we show what happens in a simple case where a fraction of the baryons form into stars, with a particular value of $\langle f_* \rangle = 0.1$, and a dispersion of $\sigma_{\log f_*} = 0.15$ dex. Again, j is assumed to be conserved, and the galaxies shift to the left. It is also usually assumed, though not required by the diagram, that this process involves the formation of a thin stellar disk whose collapse was halted by the balance between gravity and centrifugal force.

Our analysis does however assume that the baryon collapse extends all the way out to the halo virial radius. This conventional assumption is at some level implausible since DM collapse and gas cooling are governed by different physical scales in space and time. A more generalized approach where the baryon collapse radius is allowed to vary will be considered in Section 6.3.2.

Note that the f_* parameter can take on a more general meaning of *net* stellar mass fraction relative to initial gas mass, which allows for stars that are accreted by or ejected from the galaxy. We will shortly discuss a more refined model where f_* varies systematically with mass, but for now we continue with our very simplified constant- f_* model in order to consider its basic implications.

Our next model ingredient is an idealized process of angular momentum loss, with no concomitant change in mass, which we quantify by a fractional j net retention factor of f_j . An example of such a process would be internal j transfer from the stars to the DM halo. Given the parameters f_* and f_j , we may then translate the j - M relation (14) for DM halos to an equivalent one for

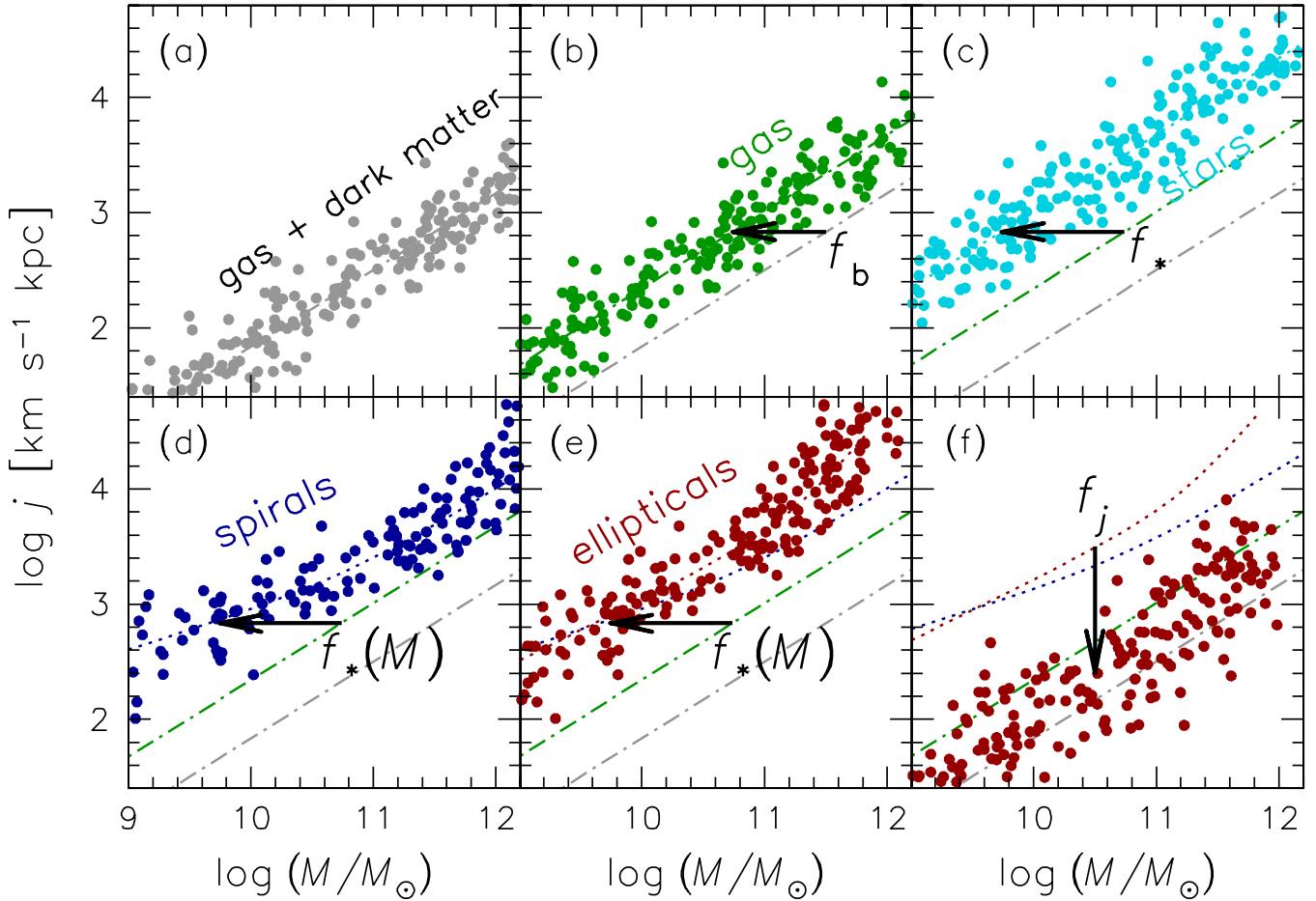


FIG. 17.— Schematic evolution of galaxies in the space of specific angular momentum and mass. Each point shows a galaxy randomly selected from a simple model (see main text). Panel (a) shows the initial galactic halos of gas and DM. Panel (b) shows the gas component only, adopting a baryon fraction of $f_b = 0.17$, with an arrow illustrating the direction that a single galaxy takes in this diagram. Panel (c) shows the stellar component after forming from the gas with an average relative fraction of $\langle f_* \rangle = 0.1$. Panels (d) and (e) show the stars of spiral and elliptical galaxies, respectively, after adopting more realistic variations of $\langle f_* \rangle$ with mass. Panel (f) shows the effect of angular momentum loss, with a factor of $\langle f_j \rangle = 0.1$. Note that these are simple, idealized models, and not every aspect should be taken literally; e.g., spiral galaxies probably do not exist at masses of $M_* \gtrsim 10^{12} M_\odot$.

the stellar components of galaxies:

$$j_* = 2.92 \times 10^4 f_j f_*^{-2/3} \lambda \left(\frac{M_*}{10^{11} M_\odot} \right)^{2/3} \text{ km s}^{-1} \text{ kpc}, \quad (15)$$

where again using the prediction for $\langle \lambda \rangle$, the numerical coefficient for $\langle j_* \rangle$ becomes $1010 \text{ km s}^{-1} \text{ kpc}$.

This relation is identical to our parameterized fit to the observational data with Equation (11), modulo the numerical factors and the value for the exponent α . Since the observed $j_* - M_*$ relation can be approximated with $\alpha = 2/3$ and a normalization j_0 , then we can express the difference between observation and theory through a simple combination of the parameters f_j and f_* :

$$j_0 = 1010 \langle f_j f_*^{-2/3} \rangle \text{ km s}^{-1} \text{ kpc}. \quad (16)$$

Equations (14)–(16) are simple but powerful, allowing us to connect the visible properties of galaxies to their invisible DM halos, using some simple parameters and assumptions. They also provide robust observational constraints on some basic characteristics of galaxy formation that are still far beyond the ability of raw theory to predict reliably. *The average value of $f_j f_*^{-2/3}$ for a pop-*

ulation of galaxies can be determined by observations as a strict constraint on theory.

We can immediately use Equation (16) in combination with the observational results for j_0 from Table 2 for fixed $\alpha = 2/3$. We find that $\langle f_j f_*^{-2/3} \rangle \simeq 1.9$ for Sb–Sm spirals and $\simeq 0.5$ for ellipticals. For example, if we assumed an arbitrary $\langle f_* \rangle = 0.2$ for both types of galaxies, then we would infer $\langle f_j \rangle \simeq 0.65$ for spirals and $\simeq 0.1$ for ellipticals. This means a systematic difference in net angular momentum retention between the two galaxy types which, although there are many further details to work through below, will hold up as a basic result of this paper.

To derive firmer constraints on f_j , we need to break the $f_* - f_j$ degeneracy by introducing well-motivated values for f_* , for both spirals and ellipticals. We also need to consider the complication that f_* cannot in reality have a simple, constant value, even on average. This is because the observed luminosity function of galaxies has a dramatically different shape from the predicted mass function of DM halos (e.g., White & Rees 1978; White & Frenk 1991; Marinoni & Hudson 2002; Yang et al. 2003; Moster et al. 2010). Below the characteristic “knee” luminosity L^* , the galaxies are observed

to follow a shallower slope than the DM mass function $dN/dM \propto M^{-2}$, while at higher luminosities, the observations are *steeper* than the predictions. The implication is that the fraction of luminous-to-dark matter declines rapidly for galaxies fainter and brighter than L^* ; i.e., assuming a constant f_b , the function $\langle f_\star \rangle(M_{\text{vir}})$ has a characteristic inverted U shape.

This empirical trend is thought to be caused physically by various feedback effects that inhibit star formation and become increasingly important in the low- and high-mass regimes (such as stellar and supermassive black hole feedback, respectively; e.g., Lacey et al. 1993; Cole et al. 1994; Somerville & Primack 1999; Bower et al. 2006; Croton et al. 2006). Regardless of the explanation, any self-consistent Λ CDM-based model must incorporate a strong, systematic mass dependence on star formation efficiency, $\langle f_\star \rangle(M_{\text{vir}})$.

One might be concerned that such a mass dependence would transform an underlying $j \propto M^{2/3}$ relation for DM halos into something very different for the stellar components of galaxies, and quite unlike our observational results. To check this, we will modify our simple model above to allow for a varying function $\langle f_\star \rangle(M_{\text{vir}})$. Since this function is a tracer of undetermined baryonic physics during galaxy evolution, there is not yet any robust theoretical prediction for it, but fortunately it can be estimated empirically. This is done in an *average* sense through various techniques such as weak gravitational lensing, stacked satellite kinematics, and matching up the mass and luminosity functions mentioned above.

There have been many studies that estimated $\langle f_\star \rangle(M_{\text{vir}})$, but few that did so separately for different galaxy types, which is important for our analysis. We therefore adopt the relations for $\langle f_\star \rangle(M_\star)$ derived by Dutton et al. (2010). For the spiral galaxies, we use their relation for “late-type” galaxies:

$$\langle f_\star \rangle(M_\star) = \frac{f_0 (M_\star/M_0)^{1/2}}{[1 + (M_\star/M_0)]^{1/2}}. \quad (17)$$

Below a characteristic mass $\log(M_0/M_\odot) \simeq 10.8$, this relation has a dependence $\langle f_\star \rangle \propto M_\star^{1/2}$. At higher masses, it approaches a constant, $f_0 \simeq 0.33$. Here we have converted the Dutton et al. results to our definition of the virial mass and to our adopted stellar IMF, while using $h = 0.72$.

For elliptical galaxies, we adopt the Dutton et al. relation for “early-type” galaxies:¹³

$$\langle f_\star \rangle(M_\star) = \frac{f_0 (M_\star/M_0)^{0.15}}{[1 + (M_\star/M_0)^2]^{1/2}}, \quad (18)$$

where $\log(M_0/M_\odot) \simeq 11.2$, $f_0 \simeq 0.14$, and the asymptotic behaviors at low and high masses are $\langle f_\star \rangle \sim M_\star^{0.15}$ and $\langle f_\star \rangle \sim M_\star^{-0.85}$, respectively. One of the key features to notice here is that an elliptical galaxy typically has

¹³ There has been very little work along these lines for elliptical and lenticular galaxies separately, but there is some recent evidence that the halo masses for these types are the same (Trujillo-Gomez et al. 2011). Note also that the Dutton et al. relations were derived for somewhat smaller mass ranges than covered by our data, and that their stellar mass determinations may not be fully consistent with our methods.

a much lower value of f_\star than a spiral with the same stellar mass: i.e., ellipticals inhabit systematically more massive DM halos, which in many cases extend up to “group” masses of $M_{\text{vir}} \sim 10^{13} M_\odot$ and beyond (see also van Uiter et al. 2011).

These $\langle f_\star \rangle(M_\star)$ relations can be uniquely transformed to $\langle f_\star \rangle(M_{\text{vir}})$, and taken together define an inverted U-shaped trend as discussed above. The relations were constructed using a compilation of different literature results, which showed an encouraging degree of mutual consistency, so we conclude that the average trends above are probably reliable at the $\sim 50\%$ (~ 0.2 dex) level. There may also be non-zero galaxy-to-galaxy variations in f_\star at a fixed mass and type; the value of this scatter is less well established, but recent analyses suggest that it may be ~ 0.15 dex (Behroozi et al. 2010; More et al. 2011). We adopt this as our default value, which fortunately is smaller than the expected dispersion in halo spin of $\simeq 0.23$ dex and so will not have much impact on our conclusions.

Using these variable $\langle f_\star \rangle(M_{\text{vir}})$ relations to construct mock j_\star - M_\star data sets as before, we plot the results in panels (d) and (e) of Figure 17. For both spirals and ellipticals, we can see that the curvature in $\langle f_\star \rangle(M_{\text{vir}})$ translates to systematic deviations in the j_\star - M_\star relation from a simple $\alpha = 2/3$ power-law. We will investigate how these deviations compare to real observations in the next subsection.

Panels (d) and (e) of Figure 17 also demonstrate that at masses of $M_\star \gtrsim 10^{11} M_\odot$, the ellipticals are predicted to have *higher* j_\star than the spirals of the same mass, owing to their differences in f_\star . The more massive DM halos of ellipticals ought to provide larger virial-radius lever arms that lead to larger j_{vir} , and therefore larger j_\star —if they retain as much fractional angular momentum as spiral galaxies do. Therefore the observed offset in j_\star - M_\star between spirals and ellipticals implies an even larger difference in $\langle f_j \rangle$ than in the simple example above with fixed $\langle f_\star \rangle = 0.2$. We will examine this apparent f_j dichotomy further in the next subsection.

As a final illustrative exercise, we generate a mock data set for elliptical galaxies as in panel (e), then adopt $\langle f_j \rangle = 0.1$, with an assumed dispersion of $\sigma_{\log f_j} = 0.15$ dex. The results are plotted in panel (f), where we see that the galaxies have coincidentally returned to nearly the original j - M sequence for halos, modulo a little curvature and increased scatter.

Figure 17 thus shows how one could map the observed j_\star - M_\star properties of a population of galaxies (panel f) to a theoretical prediction for their halos (panel a), and recover some basic parameters describing galaxy formation (see Equation (16)). This formulation is closely related to a classic theoretical framework for the formation of spiral galaxy disks, whose observed sizes and rotation velocities are generally consistent with the approximate conservation of primordial specific angular momentum ($f_j \sim 1$; e.g., Fall & Efstathiou 1980; Dalcanton et al. 1997; Mo et al. 1998). However, our formulation is more general by including also the early-type galaxies, as well as the bulge components within spiral galaxies (which we will discuss below).

6.2. Investigating the spread in j_\star

As just discussed, the observed dichotomy between the j_\star - M_\star relations of spirals and ellipticals may imply differences in their specific angular momentum retention, expressed here by the factor f_j . This interpretation is based on an implicit assumption that the parent halos of both galaxy types had the same average λ . However, a natural halo-to-halo scatter in λ is expected, and one could instead imagine the other extreme case, in which f_j is the same for the two galaxy types, while their halo λ values are systematically different (e.g., Kashlinsky 1982; Blumenthal et al. 1984; Catelan & Theuns 1996). In other words, spirals and ellipticals are drawn from the high- and low-spin tails of the λ distribution, respectively.

We call these two alternatives the “variable f_j ” and “spin bias” scenarios. In reality, a mixture of both scenarios may be present, which would be difficult to disentangle, but we can begin by investigating these two limiting cases in detail. Thus the aim of this section is to test how consistent each of these cases is with the data.

The reason we can make headway on this issue is that there are predictions from Λ CDM not only for the average value of λ , but also for its probability distribution, i.e., a lognormal with a characteristic dispersion as discussed in Section 6.1. We continue to focus on the spirals and ellipticals as the two interesting extremes of the observed j_\star range (at fixed M_\star), and consider the lenticulars as intermediate either in f_j or in λ .

We begin with the spin-bias scenario. If correct, adopting a constant f_j value for a complete, unbiased galaxy sample would allow us to work backwards to infer the underlying λ distribution, which could then be compared to the theoretical prediction. One might think that we have already implicitly carried out this test by examining the residuals from the observed j_\star - M_\star relation in Section 5.5 and Figure 16. However, that analysis did not account for the differences in f_\star between different galaxy types.

We therefore proceed with a more direct comparison to theory by generating j_\star - M_\star model predictions for each galaxy type, and calculating the observed residuals with respect to these models. We use Equation (15) with $\lambda = \langle \lambda \rangle = 0.035$, along with the empirical $\langle f_\star \rangle(M_\star)$ relations (17) and (18), and an ad-hoc $\langle f_j \rangle = 0.55$, to predict a mean j_\star - M_\star relation for each galaxy type. We then derive the residuals $\Delta \log j_\star$ by subtracting the model from the observations as in Equation (12). If the spin bias scenario is correct, then the properly reweighted distribution of these residuals ought to follow a lognormal with dispersion $\sigma_{\log j_\star} \simeq 0.27$ (which accounts for observational errors and the intrinsic scatter in f_\star).

Figure 18 presents histograms of these residuals, both by separate galaxy types (top panel), and in combination (bottom panel), which uses a renormalization by frequency of galaxy types from the ATLAS^{3D} survey, as in Section 5.5. We find that overall, the total distribution of Δj_\star has approximately the predicted width. However, the distribution in detail appears significantly different from a lognormal: there is an excess of low- Δj_\star galaxies, and a missing tail at high- Δj_\star . In particular, there are too many elliptical galaxies in the nearby universe to be explained by the tail of low-spin halos.¹⁴

¹⁴ Hernandez et al. (2007) also found in attempting to infer halo λ values for spirals and ellipticals that an ad-hoc rescaling of the

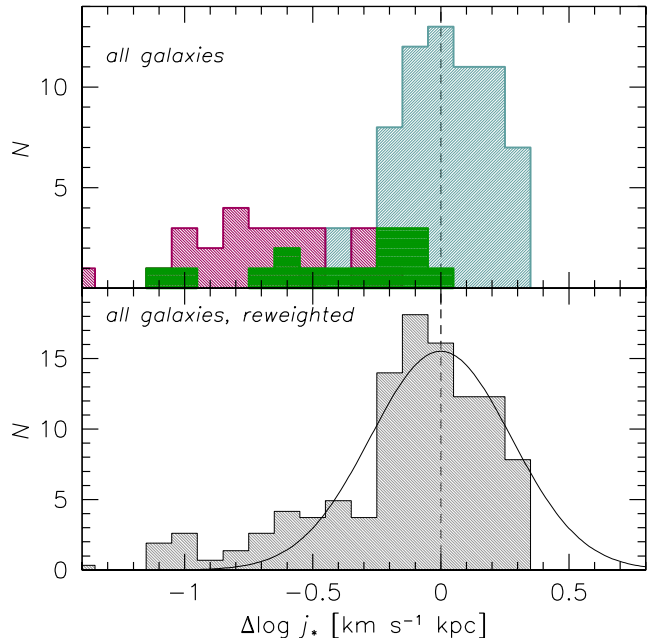


FIG. 18.— Distributions of residuals in the observed stellar specific angular momentum, with respect to the mean theoretical prediction for Λ CDM halos, after assuming a fixed j -retention parameter, $f_j = 0.55$. As in Figure 16, red, green, and blue histograms in the top panels show the residuals for elliptical, lenticular, and spiral galaxies, respectively. The bottom panel shows the same distribution, renormalized for the relative frequencies of galaxies in the nearby universe. The curve shows a predicted lognormal distribution for comparison. The distribution of residuals for spiral galaxies is narrower than expected from the distribution of halo spins, while the overall galaxy distribution shows clear departures from the lognormal model (with an excess at low j_\star and a deficit at high j_\star).

This histogram analysis appears to exclude a simple spin-bias scenario, but there are some caveats, such as small sample sizes and the assumption of perfect lognormality for the distribution of halo spins. We can make further progress by recognizing that the scenario makes predictions for the j_\star residuals not only for all galaxies combined, but also as a function of mass. This is because λ is not predicted to depend on halo mass, while the relative frequencies of different galaxy types are observed to vary strongly. One can then immediately see a serious problem with the spin-bias scenario: at high masses, almost all of the galaxies are ellipticals, which should thus be an unbiased population representing the full range of halo spins (Dutton & van den Bosch 2012 made a similar point for low-mass disk galaxies).

We investigate this issue in more detail by constructing a mock data set as in Figure 17, while this time incorporating a schematic model for spin bias. We now assume that all galaxies have $f_j = 0.45$, with the late-types inhabiting the high-spin halos, and the early-types the low-spin ones. Using the number densities of early- and late-types as a function of M_\star from ATLAS^{3D}, we use the $\langle f_\star \rangle(M_\star)$ relations to translate this to the relative fractions at fixed halo mass (which can be quite different from the fractions at fixed M_\star). We then randomly draw

elliptical values was required in order to avoid a double-peaked λ distribution.

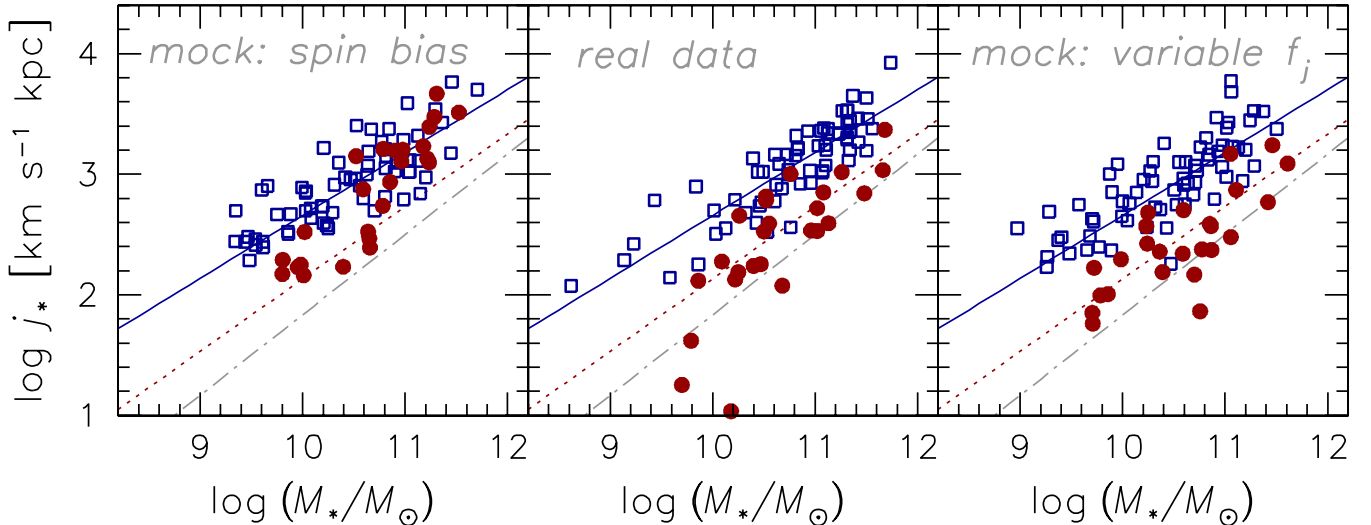


FIG. 19.— Stellar specific angular momentum vs. stellar mass, comparing mock data generated from Λ CDM-based models (left- and right-hand panels) to real data (middle panel). The model on the left includes halo spin bias, while the model on the right assumes systematic differences in angular momentum retention between spirals and ellipticals. Blue open squares and red filled circles show spirals and ellipticals, respectively, with the solid blue and dotted red lines showing the best-fit power-laws for the real data. The relation for halos is also shown for reference as a gray dot-dashed line. The mock data sets include intrinsic scatter in the parameters λ and f_* at a given mass, but *not* observational errors. The simple variable- f_j mock data on the right resemble the real data, while the spin-biased model does not.

a distribution of biased spin parameters for each galaxy type; e.g., if spirals comprise 25% of galaxies at a given mass, we draw mock spirals from the top quarter of the spin distribution. We also adopt a similar mass range and total number of galaxies as in our real data sets.

We show the resulting j_*-M_* mock data set in the left-hand panel of Figure 19, which can be compared to the real data in the middle panel. We see that the low-mass ellipticals could indeed be drawn from only the low-spin tail because of their rarity. However, at high masses the ellipticals are common and their predicted j_* values are similar to the spirals. To salvage the spin-bias scenario would thus seem to require a mass-dependent bias, which seems epicyclic and therefore not appealing.¹⁵

The biasing idea can also be discredited by environmental considerations: there are strong observational correlations between environmental density and galaxy morphology, but as mentioned earlier, halo spins in theory depend only weakly on environment (which has some observational support in the case of disk galaxies; Cervantes-Sodi et al. 2008; Berta et al. 2008). In addition, if we consider disks and bulges to be manifestations of the same j_*-M_* trends as spiral and elliptical galaxies, then the coexistence of these subcomponents within the same galaxies provides a clear argument against halo spin bias.

We next turn to the variable- f_j scenario, where spirals and ellipticals are drawn from the same underlying distribution of halo spins, but their baryonic components have systematic differences in retaining j . Given that we know $\langle f_* \rangle$ for each galaxy type, Equation (16) suggests that we can immediately use the observed j_0 normalization to infer $\langle f_j \rangle$. However, the situation is more complicated since $\langle f_* \rangle$ varies with mass and therefore one does not expect

¹⁵ There may be reasons of stability for ellipticals to be dominant at high masses (e.g., Dalcanton et al. 1997; van den Bosch 1998; Dutton & van den Bosch 2012), but this ostensibly changes the *morphology* and not j_* .

an exact $\alpha = 2/3$ for fixed f_j (recall Figure 17(d,e)).

As we did for the spin-bias scenario, we again construct mean j_*-M_* relations for each galaxy type, while now leaving f_j as a free parameter. Carrying out least-square fits to the data, we find values of $\langle f_j \rangle = 0.56 \pm 0.03$ and $\langle f_j \rangle = 0.12 \pm 0.01$ for the spiral and elliptical galaxies, respectively. The difference in $\langle f_j \rangle$ of a factor of 4.7 ± 0.8 is slightly larger than the observed j_*-M_* relative offset, as anticipated in the previous section because of the differences in $\langle f_* \rangle$ (e.g., Equation (16)).¹⁶

The next step is to verify that these best-fit models provide reasonable representations of the data. We again construct mock data sets, using the new f_j models (with 0.15 dex of scatter in f_*), and show the results in the right-hand panel of Figure 19. Here we see that, unlike the spin bias model, these variable- f_j models provide a remarkably good match to the data. The curvature of the predicted j_*-M_* relation turns out to be imperceptible, once we account for observational errors, small-number statistics, and a limited mass range.¹⁷ Furthermore, the observed slope for the spirals is shallower than $\alpha = 2/3$, which is predicted by the model.

This comparison does not entirely succeed in accounting for the *scatter* about the j_*-M_* relations. As can be seen in Figure 19, the real observations appear to follow *tighter* trends than predicted by our simple model, for both spirals and ellipticals. The model fits give rms scatters of $\sigma_{\log f_j} = 0.18$ dex and 0.25 dex for the spirals and ellipticals, which is already *less* than the expected

¹⁶ Given the degeneracy between f_j and f_* , in principle the inferred f_j dichotomy could be an artifact of errors in our adopted values for $\langle f_* \rangle$. However, these errors would have to amount to a combined factor of ~ 5 : e.g., with true $\langle f_* \rangle \sim 0.1$ for the spirals along with ~ 0.2 for the ellipticals, rather than ~ 0.25 and ~ 0.1 .

¹⁷ Future empirical estimates of j_* and M_* over a larger dynamic range could provide a strong test of constant- f_j scenarios. Given the observational difficulty of measuring j_* at high masses where the underlying halos pertain to entire galaxy groups and clusters, the best prospect for improvement would be to study lower-mass galaxies, with $\log(M_*/M_\odot) \lesssim 9$.

scatter of 0.27 dex from λ and f_* , even without allowing for measurement errors, and scatter in f_j (see also the histogram of spirals in the top panel of Figure 18, compared to the curve in the lower panel).

One possible explanation for this reduced scatter is that the baryonic processes responsible for j -loss could act as some kind of “attractor” to specific values of f_j (cf. de Jong & Lacey 2000). Alternatively, halo spin bias could be at work in a secondary role, even while f_j variation is the primary effect.¹⁸

Our overall conclusion is that the variable- f_j model reproduces the j_*-M_* observations well in general, is fairly insensitive to the exact trend of $\langle f_* \rangle$ with mass, and does not require any additional variation of $\langle f_j \rangle$ with mass. The spirals appear to have been fairly efficient in preserving the specific angular momentum imprints of their parent halos, while ellipticals have lost the vast majority of theirs.

This is a plausible scenario from a physical standpoint if we return to our proposed framework where all galaxies are composed of bulges and disks (Figure 2 and Section 5.3). Unfortunately, we do not have $\langle f_* \rangle(M_*)$ relations for the bulges and disks themselves in order to directly derive their $\langle f_j \rangle$ trends. However, given the similarities in j_*-M_* that we found between these subcomponents and the galaxies overall, it seems reasonable to suppose that bulges and disks have $\langle f_j \rangle \sim 0.1$ and ~ 0.6 , respectively, and that these values are characteristic of two distinct modes of galaxy evolution.¹⁹ We will return to this topic in the next section.

Our conclusions about *spiral* galaxies echo similar findings in the literature, which have typically inferred $\langle f_j \rangle \sim 0.5-0.6$ overall (e.g., Navarro & Steinmetz 2000; Dutton et al. 2007; Burkert 2009; Dutton & van den Bosch 2012; Kassir et al. 2012). In particular, Dutton & van den Bosch (2012) used a model parametrization similar to our (f_*, f_j) , and found that $\langle f_j \rangle$ is fairly constant over a wide mass range. Note that these authors used a parametrized mass model to fit the Tully-Fisher relation, which was then converted to an average $j_{\text{vir}}-M_{\text{vir}}$ relation. Our approach works instead in the space of observables, j_*-M_* , which is more direct and transparent while also allowing us to analyze galaxy-to-galaxy variations.²⁰

Our finding for the *ellipticals* is novel, as neither the predictions for j_*-M_* of ellipticals, nor their subsequent f_j inferences, have been well-studied before now. We

have not carried out a comparable analysis on *lenticulars* since the constraints on them are less certain. Qualitatively speaking, their observed $\log j_*$ normalization is between the other two galaxy types, which for plausible values of $\langle f_* \rangle$ implies $\langle f_j \rangle$ values that are intermediate to those for the spirals and ellipticals. In addition, there may be two subpopulations of lenticulars as discussed in Section 5.4, with low and high $\langle f_j \rangle$.

There are two interesting implications about these findings. One is that that we now have a remarkably simple and successful framework for describing and connecting some of the most fundamental properties of galaxies. The observable galaxies may be connected to their unobservable host halos using j_* and M_* along with some relatively basic parameters f_j and f_* . Such a model may appear implausibly oversimplified in the light of our ever-expanding awareness of the complexities of galaxy formation physics, but for some reason it seems to work.

The other implication is that these parameters may give us insight into the formation of disks and bulges, and into the origins of the Hubble sequence. To illustrate this point, we use our modeling procedures as described above to work backwards and estimate f_* and f_j values for *individual* galaxies. The outcome is shown in Figure 20, where one should focus on the *average* results for each galaxy type, since no attempt was made to model the scatter in f_* and λ .

The general picture that we obtain is that spiral and elliptical galaxies are clumped around two regions of parameter space: $(f_*, f_j) \sim (0.25, 0.55)$, and $\sim (0.1, 0.1)$, respectively. *Whatever processes formed and shaped these galaxies were efficient at both forming stars and retaining total specific angular momentum for the spirals, and inefficient for the ellipticals.*

As discussed in Section 1, early cosmologically-based simulations struggled to reproduce such high f_j values for spirals, finding typically $f_j \sim 0.01-0.1$, which was later realized to be due in part to numerical artifacts, and in part to inadequate feedback recipes. Feedback could be particularly important for slowing down gas collapse and star formation so that the baryons are not affected by torque-driven j transfer during early mergers (Weil et al. 1998; Sommer-Larsen et al. 2003; Hummels & Bryan 2012; Scannapieco et al. 2012). However, whatever physical processes are now invoked to explain the f_j values of spirals must simultaneously allow for much lower f_j in ellipticals (e.g., by having less efficient feedback; Zavala et al. 2008; Scannapieco et al. 2008).

6.3. Physically-motivated models for galaxy evolution

Now that we have derived a comprehensive framework for connecting j_*-M_* observations with simulated Λ CDM halos, and thereby derived generic constraints on specific angular momentum retention, f_j (Figure 20), we will work through some case studies of plausible physical processes in galaxy formation and evolution. These cases are not meant to be exhaustive, nor to provide immediate ammunition for current debates about galaxy formation, but to serve as practical examples of how the $j-M$ diagram can be used as a tool to furnish physical insight. The models involved will treat f_j and f_* as covariant parameters, unlike in the previous sections where for simplicity they were independent.

¹⁸ It has been suggested that later type galaxies are biased to lower spin halos (D’Onghia & Burkert 2004). If correct, the net impact on the j_* scatter is unclear, but one implication is that the f_j dichotomy between spirals and ellipticals would be even larger than in our no-bias scenario.

¹⁹ One concern here is that for more bulge-dominated galaxies, one might expect the disk-only $\langle f_* \rangle$ to be relatively low, and thus the disk j_* to appear relatively high. However, the observations are somewhat suggestive of the *opposite* trend, i.e., disk j_* anti-correlating with B/T .

²⁰ As a consistency check, we also take a slightly different approach and make a model prediction for the mean relation between size and rotation velocity for spirals (cf. Mo et al. 1998; Burkert & D’Onghia 2004). We adopt a value of $\langle f_* \rangle = 0.56$, and rather than assuming some function $\langle f_* \rangle(M_*)$, we relate the disk rotation and the virial circular velocity by $v_s \simeq 1.2v_{\text{vir}}$. Given $\langle \lambda \rangle = 0.035$, there is a linear relation predicted between v_s and a_e , which we show in the right-hand panel of Figure 12. To zeroth order, this prediction agrees well with the spiral data.

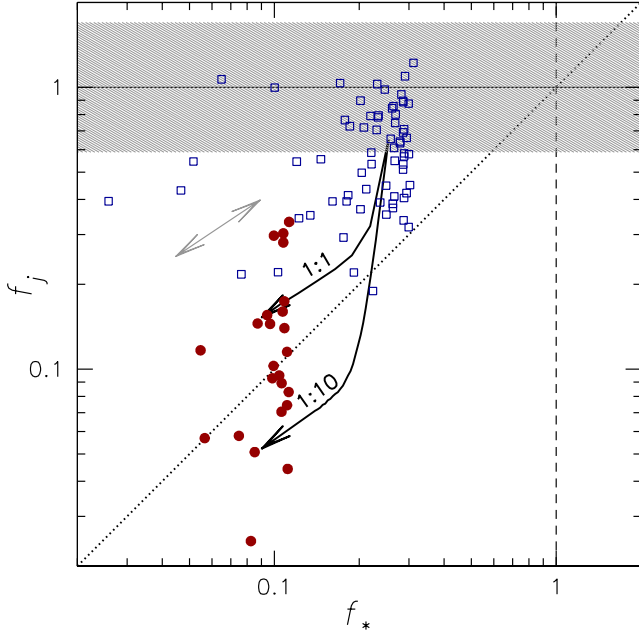


FIG. 20.— Specific angular momentum retention fraction plotted against stellar mass fraction, as inferred for individual galaxies, with symbols as in Figure 19. The dotted diagonal line is the one-to-one relation, and the gray double-arrow shows the direction of the uncertainties as driven by the $f_j \propto f_*^{2/3}$ degeneracy. The width of the shaded region around $f_j = 1$ corresponds to the scatter in spin expected for Λ CDM halos. The black arrows show schematic vectors from 1:1 and 1:10 mergers, as discussed in Section 6.3. The spiral and elliptical galaxies occupy distinct regions of the diagram, while a simple model implies that converting spirals into ellipticals would require a very large amount of growth through $\sim 1:3$ mergers.

A general constraint to keep in mind is that for each galaxy type, f_j is approximately constant as a function of mass, including little additional scatter, which accounts for the observed j – M relations appearing so similar to those for theoretical DM halos. *Any model for angular momentum evolution should explain why galaxies appear to remember so faithfully the overall initial conditions of their parent halos.*

The challenge of this f_j constancy has been recognized previously for disk galaxies. There are a variety of physical mechanisms during galaxy evolution that could involve j transfer (e.g., gas cooling and feedback), but unlike gravitational clustering, these baryonic processes (and the resulting f_j values) are expected to depend strongly on mass, which appears to require some degree of fine-tuning to reconcile with the observations (e.g., Dutton & van den Bosch 2012). Our inclusion of early-type galaxies in this framework, with near-constant f_j , deepens the mystery: there are now *two* fine-tuning conspiracies to explain.

Here we emphasize again a distinction from comparisons between *internal* distributions with radius of j for stars and DM halos (e.g., Bullock et al. 2001; van den Bosch et al. 2001; Maller et al. 2002; Sharma & Steinmetz 2005). As mentioned in Section 1, there is ample reason to expect redistribution of j_* to occur within the baryonic component of a galaxy and thereby violate strong j conservation. However, this does not affect our examination of weak conservation,

where the overall value of j may remain roughly the same (assuming negligible transfer of j between baryons and DM).

We may reduce the potential explanations for the systematic difference in f_j between spirals and ellipticals into two basic scenarios, which we will examine before summarizing the overall picture. One general scenario is an *internal* angular momentum bias, where high- and low- j_* galaxies were formed from parts of their available gas supply that had preferentially high or low j . The other is that these galaxies experienced systematic differences in angular momentum transport *after* star formation, and during subsequent galaxy assembly phases.

Below, Section 6.3.1 discusses outflow and stripping scenarios, Section 6.3.2 considers biased collapse, and Section 6.3.3 examines mergers. Section 6.3.4 surveys the plausibility of these evolutionary modes in the light of the j_* – M_* observations.

6.3.1. Outflows and stripping

One example of the first scenario involves *gas outflows*, whether caused by galactic winds or by some other mechanism. Let us assume that the baryons in a galaxy collapse into a thin disk while preserving the total specific angular momentum, i.e., $f_j = 1$ (recall Figure 17(b)). The local specific angular momentum within the disk, $j_g(R) \propto R v_{\text{rot}}(R)$, is assumed to increase monotonically with galactocentric radius, which is unavoidable if the gas follows co-rotating circular orbits (the rotation-velocity profile cannot decrease any more rapidly than Keplerian, while the lever arm R in the j calculation increases linearly).

Before many stars form, an outflow begins which we parameterize by a mass loss that is proportional to the gas surface density to some unknown power β :

$$\Delta M_g \propto \Sigma_g^\beta. \quad (19)$$

Because the gas is presumed to settle into a configuration where the density increases toward the center (e.g., an exponential profile), the parameter β translates into a biased removal of gas from different disk radii, which in turn means depletion of gas parcels with systematically different j_g .

To analyze this scenario further, we now introduce Figure 21, which like Figure 17 illustrates schematic vectors of mass and angular momentum evolution, but now extends to more specific, physically-motivated processes. In Figure 21(a), the horizontal arrow to the left illustrates an outflow with $\beta = 0$: the gas everywhere in the disk is depleted by an equal fraction, and its initial specific angular momentum is preserved, while its mass decreases. If $\beta > 0$, then the outflows occur preferentially in the high-density, central regions that have relatively low j_g , and so the overall j_g for the galaxy increases (diagonal arrow toward upper left; cf. Binney et al. 2001; Sharma et al. 2012). If $\beta < 0$, then the mass loss is preferentially from the outer regions, and the overall j_g decreases (diagonal arrows toward lower left). Thus, outflows could in principle produce either a net increase or decrease in f_j .

It should be kept in mind that these outflows represent only material that is launched completely out of the galaxy, never to return. Other types of outflows may

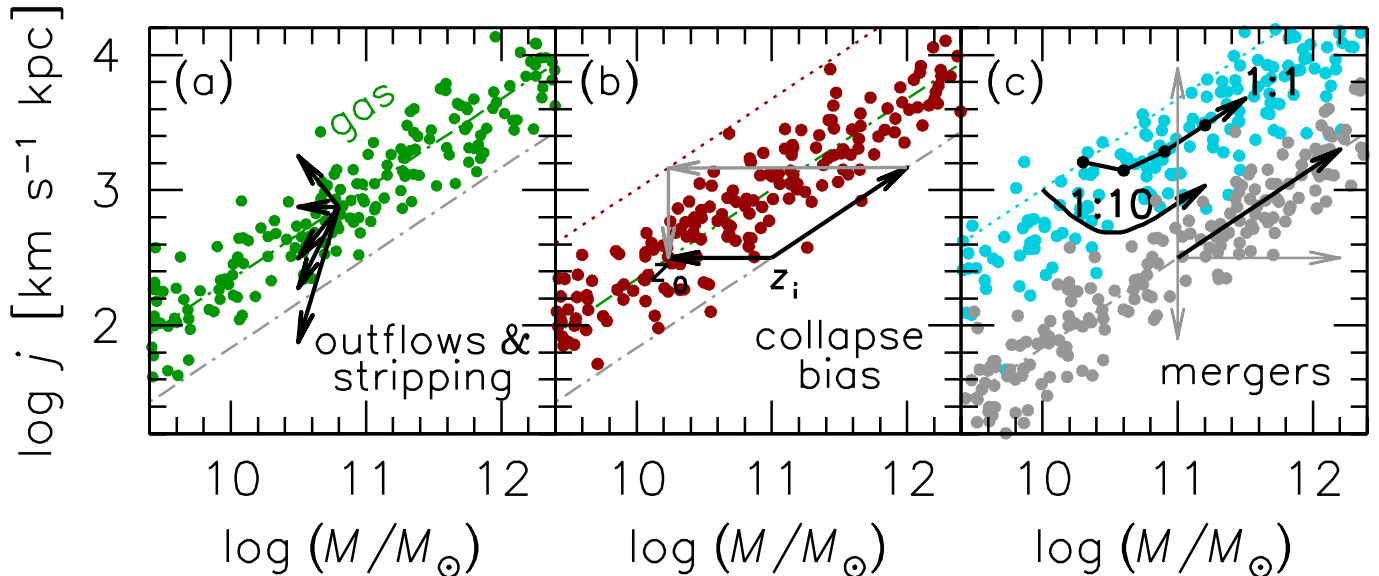


FIG. 21.— Schematic evolution of galaxies in specific angular momentum and mass, as in Figure 17, but now considering evolution through gas outflows, stripping, and biased baryon collapse, and galaxy mergers. Panel (a) show initial conditions for pre-collapse gas (dots), and possible evolutionary vectors from outflows and stripping (arrows; see text for details). Panel (b) shows the collapse of gas and formation of stars at some initial redshift z_i , preserving the j_* - M_* values until a final redshift z_0 (black arrow to the left, with dots illustrating a population of galaxies). The halo grows until redshift z_0 with no further star formation (black arrow to upper right). At z_0 , the expected trend with perfect j conservation is the dotted line, and net values for f_* and f_j would be inferred using the leftward and downward gray arrows, respectively. Panel (c) shows initial conditions for DM halos as gray dots, and schematic vectors of evolution through mergers (gray arrows): mass growth (to the right), specific angular momentum decrease through cancellation of the spin components (downwards), and increase through the orbital component (upwards). The net evolution is a black diagonal arrow to the upper right. The upper dotted track marks the initial conditions for stellar disks, and the blue dots show disks after having undergone four 1:1 mergers each. The upper black curved vector illustrates the typical evolution of a galaxy, with each black dot marking the beginning of a discrete merger event. The lower black curved vector shows the same for a series of 1:10 mergers (note that for clarity, the curved vectors are arbitrarily shifted relative to the $f_j = 1$ starting point for the DM vector). In both cases, after the mass has grown by a factor of ~ 2 , the orbital j_* dominates the evolution, moving merger remnants along a j_* - M_* track parallel to, but lower than, the initial disk trend.

also occur, where gas is expelled outward but remains bound and falls inward again, as in a galactic fountain (e.g., Brook et al. 2012). However, such internal processes might alter only the detailed distribution with radius of j , and not affect the overall value which concerns us here (see the discussion above of weak and strong j conservation). More complex scenarios could also be considered, where fountain material interacts with halo gas and exchanges angular momentum (e.g., Melioli et al. 2009; Marinacci et al. 2011), leading to shifts in j_* for the stellar disk that eventually forms.

A mechanism related to gas outflows is galaxy *stripping* through gravitational interactions with other galaxies in a dense environment. Here the effects on j_* and M_* depend on whether the tidal stripping occurs before or after the gas collapses. If a galactic halo is tidally stripped *before* the gas collapses (e.g., Larson et al. 1980), then the reservoir of M_g and j_g available for collapse is depleted in a manner that depends on the internal distribution of these quantities. F83 adopted some plausible distributions and worked out the resulting j - M changes: we will not repeat the analysis here, but merely show the equivalent evolutionary vectors as the three arrows in Figure 21(a) pointing downwards to the left.

There are two key features to notice with the gaseous stripping arrows. One is that unlike outflows, this stripping can only *decrease* f_j ($\beta < 0$) since it acts solely on the outer regions. The second is that plausible j -loss vectors are accompanied by substantial mass loss, which means that it is fairly difficult to move galaxies

away from the initial j - M sequence. This conclusion is supported by N -body simulations of Λ CDM halos, which find that the environmental dependencies of halo λ are fairly weak (Zurek et al. 1988; Lemson & Kauffmann 1999; Reed et al. 2005).

If instead the stripping occurs *after* the gas collapse, then j and M decrease for the DM but not for the baryons. This leads to elevated values of f_j and f_* , which could be investigated through observational constraints on M_{vir} for field galaxies in comparison to satellite galaxies in massive groups.

6.3.2. Biased collapse

There is another scenario that is functionally equivalent in the j - M diagram to outflow or stripping, but which merits special attention. Here we consider a *spatially-biased* subcomponent of the initial gas which collapses and forms stars. Rather than our default assumption of uniform efficiencies f_* and f_j throughout the virial region, we assume that stars form preferentially in the *inner regions* of the halo, while the outer regions remain largely gaseous and form relatively few stars.

This scenario was introduced by Fall (2002) and is motivated by the higher densities, and thus overall gas dissipation rates (through cooling and cloud collisions), in the inner regions. The consequent spatial bias in star formation can also be understood as a *temporal* bias, if one considers an idealized onion-shell model wherein galaxies form by inside-out collapse, with virialization

and star formation occurring first in the central regions (cf. van den Bosch 1998; Kepner 1999). Even in more realistic, hierarchical galaxy models, it is uncontroversial that a large fraction of the baryons within a galaxy halo at any given time will not yet have formed stars, and are located preferentially at larger radii. The stars observed in a galaxy at $z = 0$ will have formed on average at higher redshifts, and from gas that was more centrally confined than the $z = 0$ virial volume.

Because j for a Λ CDM halo is expected to increase systematically with both internal radius and time, the above biasing scenario implies that j_* for a galaxy will be lower than its total j (including DM). Such a biasing framework was used by Kassin et al. (2012) to connect observed disk galaxies with simulated Λ CDM halos, and thereby infer a radius of baryonic collapse. Here we outline a generic toy model of collapse bias, to understand its implications in the context of j - M evolution vectors.

For simplicity, we adopt a step-function model where at an initial redshift z_i , all of the gas within the virial radius instantaneously collapses and forms stars with perfect efficiency and angular momentum conservation ($f_* = f_j = 1$), and subsequently no star formation occurs ($f_* = 0$). This scenario is illustrated by Figure 21(b), where z_i marks the initial halo parameters. The leftward arrow shows the formation of the stars, with j_* - M_* parameters that are preserved until $z_0 = 0$. The diagonal arrow to the upper-right shows the subsequent evolution of the halo. Because the halo continues to grow in M and j , the net values of f_* and f_j for the stars will decrease with time, which is illustrated by the gray arrows which are the inferences made by connecting the final conditions of the halo and stars.

This biasing scenario might seem to provide a tidy alternative for understanding galaxies that have *apparently* experienced baryonic angular momentum loss. However, it is important to realize that such biasing cannot explain just any arbitrary set of j_* - M_* observations. For example, the vectors in Figure 21(b) were constructed to represent a typical early-type galaxy with a net $f_* = 0.1$ at $z = 0$, which turns out to have a net $f_j = 0.22$, i.e., not reproducing the apparent $\langle f_j \rangle \sim 0.1$ from observations. Note that this model had an initial $f_* = 1$, but in reality, we expect an initial $f_* < 1$, which would increase the discrepancy. We will discuss this scenario further in Section 6.3.4; for now, it serves as an important illustration of how constructing physically-motivated vectors in the j_* - M_* diagram can provide tight constraints on possible evolutionary scenarios.

6.3.3. Mergers

We next consider galaxy *merging* following star formation, which is likely to be more important for ellipticals than for spirals. The mass of a galaxy increases through a merger, while its final j is determined by the vector sum of three initial j components (the internal j for the two progenitor galaxies, and their relative orbital j), as well as by any exchange of j with the environment (e.g., between the stars and their surrounding DM halos). The random relative orientations of the first two components will cause them to partially cancel out, which contributes a net *decrease* to j . That is, after N equal-mass mergers, there will be average trends for the remnant of $J \propto N^{1/2}$ and $M \propto N$, and therefore $j \propto N^{-1/2}$ (Fall

1979; Aarseth & Fall 1980). The orbital j and the j exchange processes are more difficult to model a priori.

The effects of mergers on DM halos have been studied extensively through numerical simulations, resulting in a general picture where major mergers tend to “spin up” the halos, while minor mergers and smooth accretion tend to spin them down (e.g., Gardner 2001; Maller et al. 2002; Vitvitska et al. 2002; Peirani et al. 2004; D’Onghia & Burkert 2004; Hetznecker & Burkert 2006). Given that the j_{vir} - M_{vir} relation is scale-free and has a normalization that is expected to change only gradually, if at all, with time (e.g., Navarro & Steinmetz 1997), we conclude that for individual halos, the co-addition of the above processes must amount to a random-walk that takes them on average *along* the j_{vir} - M_{vir} sequence.

We illustrate this process in Figure 21(c) with a schematic evolutionary vector for galaxy halos, broken down into subcomponents of j_{vir} and M_{vir} changes.²¹ Doubling the mass should typically increase j_{vir} by a factor of $2^{2/3} = 1.6$.

The effects of mergers on the stellar components of galaxies, which have collapsed by large factors within their DM halos, are somewhat different. Qualitatively speaking, it is a generic dynamical requirement that the stars shed some of their orbital angular momentum, via tidal torques or dynamical friction, in order to coalesce into a bound merger remnant (e.g., Frenk et al. 1985; Zurek et al. 1988; Barnes 1988; D’Onghia et al. 2006).

More quantitatively, we may make an initial, plausible guess that the “final pass” of the merger before coalescence involves an impact parameter and relative velocity that are similar to the stellar scalelength and circular velocity of the larger progenitor. This would mean that the smaller progenitor would bring in an orbital $j_{*,2}$ of a similar magnitude to internal $j_{*,1}$ of the larger progenitor (i.e., $\Delta J_* = j_{*,2} M_{*,2} \sim j_{*,1} M_{*,2}$).

We sketch out some implications of this kind of merger evolution in Figure 21(c). Starting with galaxy disks randomly selected along the median j_* - M_* trend as in Figure 17(c) (adopting a simple $f_* = 0.1$ model with scatter included for halo λ), we apply a sequence of four mergers to each disk. Each merger has a 1:1 mass ratio, and the relative vectors of internal j_* and orbital j_* are selected randomly (this is similar in spirit to the orbital-merger model of Maller et al. 2002). The blue dots show the end result after the merger sequence, and the upper arrow shows the median trend for a single galaxy, with black dots marking the discrete merger events. Note that at this point, the series of four 1:1 events is meant as a thought experiment and not necessarily as a likely merger history.

After an initial decrease of j_* in the first merger from cancellation of the internal spin vectors, the orbital j_* dominates the evolution of the merger remnant (e.g., Aarseth & Fall 1980; Hetznecker & Burkert 2006; this

²¹ In the merging of DM halos, the resulting angular momentum and mass are *not* the simple sum of those properties from the progenitors. The combination of the two virial regions in a merger increases the *density* within a fixed physical radius, but also increases the *volume* of the virial region, so that more of the surrounding material falls under the gravitational sway of the two galaxies together. A 1:1 merger typically increases M_{vir} by a factor of ~ 2.3 ; similar effects apply to j_{vir} .

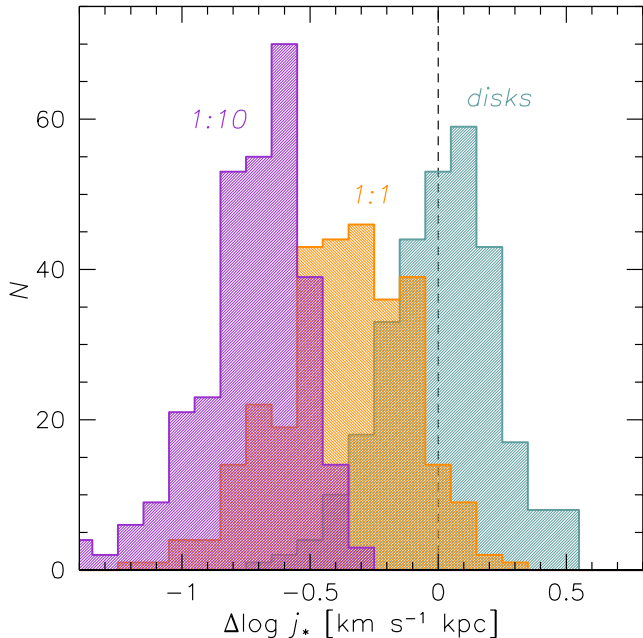


FIG. 22.— Distributions of specific angular momentum residuals, relative to the mean trend for spiral disks, using the same analysis as in Figure 21(c). The right histogram shows the disk initial conditions. The middle and left histograms show merger remnants after having grown by a factor of 16 in mass, for 1:1 and 1:10 mergers, respectively. The j_* distribution has a smaller mean and dispersion for the 1:10 mergers than for the 1:1 mergers.

also means that the results hardly change if the “accreted” galaxies are low- j_* spheroids rather than disks as we have assumed here). Because the orbital j_* term is assumed to be similar to the disk j_*-M_* trend, the final trend for the merger remnants parallels the disk trend, while being offset to lower j_* by a factor of ~ 2 (~ -0.3 dex). Referring back to Figure 17, this corresponds to an effective angular momentum loss term of $f_j \sim 0.5$. The distribution of the offset is also shown by a histogram in Figure 22.

We have carried out the same exercise for a series of 1:10 mergers, with a median trend shown by the lower vector in Figure 21(c). The result is similar to the 1:1 case, with orbital j_* dominating the evolution after the galaxy grows in mass by a factor of ~ 2 . However, the final j_* trend is now lower than the disks by a factor of ~ 6 (~ -0.8 dex; $f_j \sim 0.15$), with less scatter than in the 1:1 case (see Figure 22 again). These differences arise because there is less stochasticity with the 1:10 mergers, where random walk effects tend both to wash out variations and to dilute the orbital contributions to j_* .²² A more realistic mixture of multiple mergers with varying mass ratios would presumably produce a j_* distribution with a peak intermediate to our 1:1 and 1:10 scenarios, and with a larger scatter.

²² This scenario has some parallels to discussions in the literature about the systematic relations between angular momentum and merger histories, and the implications for the observed properties of galaxies (e.g., D’Onghia & Burkert 2004; Vitvitska et al. 2002; Primack 2005; D’Onghia & Navarro 2007; Sharma et al. 2012). However, those studies did not always make a clear distinction between the differing merger dynamics of DM halos and of their embedded stellar components.

These calculations are laden with simplifying assumptions and could easily be wrong by a factor of 2 in j_* . However, they are meant to illustrate some possible implications of merger activity in a hierarchical context. First of all, it is plausible that spheroids with a merger origin would follow a j_*-M_* relation that is parallel to that of spiral disks, but offset to lower j_* by a factor of a few.²³ Second, the scatter in j_* introduced by random merging may be relatively small.

These two results in our toy model are both driven by the dominant contributions of orbital j_* . Similar points were made by Fall (1979) and by Zurek et al. (1988), in the latter case based on the prediction that λ would be fairly constant with radius inside DM halos. The stars that condense at the center of a halo, and then participate collisionlessly in its merger history, would naturally follow the same $j-M$ scaling relations as the overall halos, modulo a smaller scale-length in converting from λ to j (in Equation (13), $|E|$ is inversely proportional to the radius).

6.3.4. Evaluating the possibilities

We now step back and consider how well the preceding evolutionary scenarios (outflows, stripping, collapse bias, and mergers) mesh with the observational constraints (Figures 14 and 20). The idea is to find a vector (or combination of vectors) that connects up the well-established endpoints in the $j-M$ diagram: the Λ CDM halo initial conditions and the $z = 0$ galaxy observations. It should however be remembered that the focus of this paper is not to solve long-standing questions about galaxy evolution which may require a detailed understanding of the physics involved. Instead, our more modest goals are to illustrate how the $j-M$ diagram can be used in practical terms as a constraint on theory, while looking for any hints as to the viability of various scenarios.

Recent work in numerical simulations of *disk* galaxy formation has emphasized how outflows might remove low- j_g material, which counteracts j -loss through tidal torques during galaxy collapse, and maintains a high net level of f_j (e.g., Brook et al. 2011; Guedes et al. 2011). We could then imagine that the differences between spiral and elliptical galaxies originate from the spirals having much stronger outflows at early times.

This outflow scenario implies more mass loss in spirals and so would initially seem to work the wrong way in explaining the f_* differences—but there could be other factors besides gas-depletion that affect f_* . It is beyond the scope of this paper to explore this scenario in detail, but we emphasize that the focus on reproducing f_j and f_* for spirals needs to expand to include simultaneously the constraints from ellipticals, beyond these being nuisance factors that represent failed disks.

We have already discussed how stripping before baryonic collapse is not expected to produce large changes in the observable j_*-M_* relations, which may indeed be part of the reason that there is not more scatter in these relations.²⁴ There is also a more obvious constraint that

²³ More generally, a similar slope would presumably be driven by any merger history that involves a scale-free mass spectrum of progenitors. This is a basic property of Λ CDM halos, but is incorrect at some level for stellar galaxies, owing to the strong break in their luminosity function.

²⁴ There is one case where severe stripping has apparently led

both spirals and ellipticals exist in the field and in clusters, so present-day environment cannot be the unique driver of morphology and j evolution.

Collapse bias is an appealing possibility because it would provide a natural explanation for the positive correlation between f_* and f_j as in Figure 20. In this scenario, elliptical galaxies would cease to build up both M_* and j_* at relatively early times, with the remaining baryonic M and j at late times either residing in a hot gas halo or having been blown out into intergalactic space. Spiral galaxies would have more protracted star formation histories that increase M_* and j_* monotonically with time.

Besides explaining the relative positions of ellipticals and spirals in the j_*-M_* diagram, this scenario also fits in naturally with the observation that the stars in spirals are on average much younger than those in ellipticals. There may be additional implications if one connects the *baryon* collapse to the *overall halo* collapse, which has a well-understood theoretical underpinning. At a given $z = 0$ mass, some halos should have collapsed earlier than others, leading to their DM distributions being more centrally concentrated. Given a fixed λ , the central DM and associated stars would then have relatively low j values. Since halo collapse time is correlated strongly with environmental density, one would then expect the low- j_* galaxies to reside preferentially in high-density environments – which is indeed what is found observationally (through the traditional morphology-density relation).

A potential problem with this scenario is that it does not appear by itself to be capable of explaining the apparent deficit of j_* in ellipticals, as discussed in Section 6.3.2. More detailed analysis would be needed to see if halo concentration makes a difference, and to understand the baryonic physics of why early-collapsing galaxies would also shut down their star formation more drastically than late collapsers. In addition to collapse bias, other effects may also need to be involved, such as a bias to low spin for their halos, or a component of real j loss.

The merger scenario is a common explanation for ellipticals, since it accounts for spheroidal morphologies through violent relaxation (Toomre 1977), and because there is strong observational evidence for some elliptical galaxies actively forming through mergers (e.g., Rothberg & Joseph 2006). Our toy model analysis suggests that the overall effect of mergers is to *reduce* the j_* of the remnant relative to an initial j_*-M_* trend for disks, while the combination of *multiple* mergers may move the remnants parallel to that trend (Figure 21(c)). This might provide a natural explanation for the observed j_*-M_* trend for ellipticals: the slope, scatter, and offset relative to disks. Note that it is not entirely clear in this context why the spiral bulges and the ellipticals would follow the same j_*-M_* trends.

A more quantitative comparison of our model to the observations allows us not only to constrain the typical mass ratios in mergers (as Figure 22), but also to infer the amount of mass growth in ellipticals since their assumed primordial disk phase. We do so by mapping our toy model vectors for mergers in the key f_j-f_* diagram

(Figure 20), starting from initial conditions similar to present-day spirals ($f_* = 0.25, f_j = 0.6$), and requiring that they terminate at ($f_* = 0.1, f_j = 0.1$).

Recalling that M_{vir} growth slightly outpaces M_* growth we find that reducing f_* by a factor of 2.5 requires a very long series of mergers, with a final growth factor of ~ 100 in M_* and ~ 300 in M_{vir} . Consideration of the f_j constraint then suggests a typical merger mass ratio of $\sim 1:3$. Such “major mergers” seem like a reasonable pathway to forming elliptical galaxies, although recent work suggests a more dominant role for *minor* mergers (e.g., $\sim 1:10$; Naab et al. 2009; Bezanson et al. 2009; Khochfar et al. 2011; Oser et al. 2012; Johansson et al. 2012), which is motivated in part by explaining trends in size evolution, and is also supported by the observed *shapes* of rotation-velocity profiles (see Section 5.2 and Arnold et al. 2011).²⁵ This apparent tension is not of great concern since our current results involve significant observational uncertainties and a crude model for the merging vectors in Figure 21(c), while not taking proper account of the redshift-dependence of virial quantities. However, they are intended to illustrate conceptually the kinds of constraints that are possible with more careful modeling.

A merger scenario may successfully explain the j_*-M_* properties of ellipticals, but it should be remembered that in a cosmological context, all galaxies including spirals should experience a continuous rain of accreting objects. Even if spiral galaxies have systematically avoided the most extreme merger events, they will have still experienced events in the $\sim 1:10$ range (e.g., Kauffmann & White 1993; Stewart et al. 2008; Fakhouri et al. 2010), which as shown in our toy models could significantly reduce j_* . A more detailed analysis of j_*-M_* evolution within a cosmological framework is needed in order to investigate the quantitative differences that might arise between spirals and ellipticals owing to varying merger histories. In particular, an explanation for the observed bulge-disk j_* bimodality is needed, since a spectrum of merger histories is more suggestive of a smooth distribution of j_* . It should also be kept in mind that $\langle f_*(M_*) \rangle$ is observationally constrained not only for present-day galaxies, but also at earlier times (e.g., Conroy & Wechsler 2009; Moster et al. 2012), which introduces additional “boundary conditions” to $j-M$ evolution.

Synthesizing the scenarios above, it seems plausible that ellipticals might be explained through a combination of collapse bias and multiple mergers—which bears a notable resemblance to recent discussions of two-phase galaxy formation (Oser et al. 2010). In this context, an early burst of star formation would both imprint a relatively low initial j_* , and allow more opportunity for subsequent mergers to reduce j_* further. Spirals would be

to a large reduction in j_* : NGC 4486B, which is a low- j_* outlier in Figure 14, and is discussed in Romanowsky et al. (2012). This “compact elliptical” is a fairly rare type of galaxy.

²⁵ In more detail, the fast- and slow-rotator subcategories of ellipticals (Section 4.2) are often thought to originate in different merger histories, such as binary versus multiple mergers (e.g., Burkert et al. 2008; Bois et al. 2011). Our discussion concerns primarily the fast-rotators, since these represent the vast majority of ellipticals, and in addition, our j_* constraints for the slow-rotators are less certain. However, as discussed in Sections 5.2 and 5.3, we detect no systematic difference in j_*-M_* space between the two galaxy types, suggesting that they may have relatively similar merger histories after all.

those systems where late gas infall both brings in higher j , and avoids the most active merging period.

There are of course other considerations besides angular momentum when constructing models of galaxy evolution, which are beyond the scope of this paper to evaluate. We have also been able to cover only a subset of possible scenarios.

One significant omission is the disk-instability pathway for bulge formation (e.g., Toomre 1964; Dalcanton et al. 1997; van den Bosch 1998; Parry et al. 2009), which is an internal process where the bulge and disk either form from high- and low- j material, or else exchange j through gravitational torques. While this pathway is usually considered in connection with pseudo-bulges, there are recent proposals that the special conditions in high-redshift galaxy disks can lead to the massive, classical bulges of present-day spirals, lenticulars, and ellipticals (e.g., Noguchi 1999; Immeli et al. 2004; Elmegreen et al. 2008; Dekel et al. 2009a,b; Ceverino et al. 2010). The filamentary nature of mass and j inflows at high redshift may also require significant revisions to standard spherical models (Danovich et al. 2012; Sales et al. 2012; Dubois et al. 2012; Kimm et al. 2011).

Our overarching emphasis here is that whatever the mechanisms for galaxy formation, they must reproduce the basic j_\star - M_\star scaling relations *observed for both spiral and elliptical galaxies*. A combination of all the processes mentioned above, and more, could be operational in real galaxies, where each process must be associated with a vector of j_\star - M_\star evolution that is not arbitrary but physically-motivated, as we have sketched in Figures 20 and 17. The sum of these vectors over the lifetime of the galaxy must preserve the halo-like scaling relations, *along with a relatively small scatter*. These may be very challenging constraints to match in practice, particularly if one includes boundary conditions on $f_\star(M_\star)$ evolution with redshift, and requires that the j_\star - M_\star relations hold for both bulge and disk components simultaneously within the same galaxies.

Thus, a fresh approach to j - M analysis appears to hold promise for providing new, powerful constraints on galaxy evolution. We would encourage numerical simulators to keep this approach in mind as part of their toolkit, tracking the evolution of their simulated galaxies in the j - M diagram, while refining our schematic estimates of Δj - ΔM vectors, and thereby gaining more insights into the underlying physical processes in the simulations.

7. SUMMARY AND CONCLUSIONS

We have revisited the pioneering study of F83 which derived observational estimates for the fundamental quantities M_\star and j_\star (stellar mass and specific angular momentum) of spiral and elliptical galaxies, and compared these to theoretical expectations based on hierarchical assembly. Although the amount and distribution of j_\star in late-type galaxies has been an intensively-studied topic in the intervening years, even the most basic trends for early-types have not been satisfactorily established. We have capitalized on the advent of radially-extended kinematic data for a large sample of early-type galaxies, to update and extend the analyses of F83.

We focus first on detailed analysis of a small sample of galaxies with data extending to typically five effective radii, which is the distance one must reach for a high de-

gree of confidence in the j_\star estimates. We derive various formulae for use in quantifying j_\star for pressure supported systems, including deprojection effects. In order to estimate j_\star for a larger sample of galaxies without requiring detailed modeling and data to very large radii, we test a simple, heuristic j_\star -estimator.

Based on the shapes of observed rotation-velocity profiles for the detailed sample of galaxies, we find that a convenient metric for the characteristic rotation velocity v_s of a galaxy is provided by the observed rotation at a semi-major-axis distance of two effective radii. This approximation is accurate at the level of ~ 0.1 dex, which is suitable for studying galaxy-to-galaxy variations in j_\star .

We next assemble a large sample of galaxies in the nearby universe with adequate photometric and kinematic data for estimating j_\star and M_\star . This sample covers the full spectrum of bright galaxy types from bulgeless spiral to diskless elliptical, as well as a wide range in M_\star , centered approximately at the characteristic mass M_\star^* . We use our simple formula for estimating j_\star , while adopting simple bulge+disk models for the spiral galaxies.

Along the way, we also introduce an important new observational scaling relation for galaxies of all types: v_s versus M_\star . This relation is analogous to the well-known Tully-Fisher relation for disk galaxies, but is more closely related to angular momentum than to dynamical mass. Unlike the generalized Tully-Fisher relation, the mass-rotation velocity relation shows *near-perpendicular* rather than parallel trends for spiral and elliptical galaxies. These rotation-velocity trends combine with size-mass trends to trace the more fundamental j_\star - M_\star trends.

Our combined j_\star - M_\star estimates confirm the basic result of F83 that late-type spiral and elliptical galaxies follow parallel sequences of roughly $\alpha \sim 2/3$ log-slope, but with a large zeropoint difference (in our analysis, the ellipticals have a factor of ~ 3 -4 lower j_\star at a fixed M_\star). Although this conclusion has already been used in some theoretical analyses, now it has a much firmer observational basis. In particular, the data do not support previous suggestions that major mergers have transported large amounts of angular momentum into the outer regions of ellipticals.

We confirm for the first time that lenticular galaxies on average lie intermediate to ellipticals and late-type spirals in the j_\star - M_\star plane, with tentative indications for two families of lenticulars characterized by low and high j_\star . We see no indication of systematic, overall differences between centrally fast- and slow-rotator ellipticals. We also find that spiral bulges are consistent with following the j_\star - M_\star sequence for ellipticals, despite having very different relations between mass, size, and rotation. Thus, as far as the fundamental parameters j_\star and M_\star are concerned, spiral bulges are essentially like mini-ellipticals.

We examine the residuals of the combined galaxy j_\star - M_\star data with respect to the disk-only trend, and find that these correlate better with disk-to-bulge ratio than with Hubble type. They also deviate from a lognormal distribution, possibly suggesting instead a bimodality in j_\star . Considering all of these results together, we propose an alternative framework to the Hubble sequence, based on more physically motivated parameters. In this picture, all galaxies are a combination of a bulge and a disk, which are distinct subcomponents with different characteristic amounts of j_\star . Galaxy morphology may

then be seen as a secondary manifestation of the mix of high- and low- j material, or equivalently, the position of a galaxy in j_\star - M_\star parameter space is a reflection of its bulge-to-disk ratio.

We next connect our observational results to a theoretical framework based on the hierarchical assembly of galaxy halos in a Λ CDM cosmology. We use numerically-informed analytic methods that are much simpler than hydrodynamical simulations, but less susceptible to the large, lingering uncertainties about baryonic recipes, resolution effects, and other numerical issues. We find that the predictions for universal mean values of halo spin translate into $j_{\text{vir}}-M_{\text{vir}}$ relations with an $\alpha = 2/3$ log-slope, which is remarkably similar to the observed $j_\star-M_\star$ relations. The zeropoint differences among these relations provide valuable clues to the formation processes of different galaxy types.

Mapping between halo and stellar quantities involves two basic parameters: the net fraction of baryons turned into stars, f_\star , and the fraction of specific j retained, f_j . We find that realistic variations of f_\star with mass produce surprisingly mild deviations of the $j_\star-M_\star$ relation from a simple $\alpha = 2/3$ power-law. The most noticeable correction is a slightly shallower predicted slope for the spirals, which turns out to agree well with the observations.

We explore two simplified alternative scenarios for explaining the spiral-elliptical dichotomy in the $j_\star-M_\star$ plane: the formation of spiral and elliptical galaxies in low- and high-spin halos, respectively (spin-bias scenario); and a difference in j retention (variable- f_j scenario). We find that spin-bias does not explain the tails of the observed j_\star distribution, nor does it agree with the observed trend as a function of mass for the elliptical galaxies. The variable- f_j scenario, on the other hand, matches the data well and suggests universal values of $f_j \sim 0.55$ and $f_j \sim 0.1$ for spirals and ellipticals, or for disks and bulges, respectively. The near-constancy of these values is intriguing, and means that all the complexities of galaxy evolution somehow effectively reduce to a simple model, where galactic stars have preserved the “initial” conditions of their host halos, including the $j_{\text{vir}}-M_{\text{vir}}$ slope and scatter. This interpretation may be useful for semi-analytically populating DM halos with both spiral and elliptical galaxies (cf. Mo et al. 1998).

Our f_j result for spirals confirms similar conclusions going back decades, that these galaxies have retained most of their primordial specific angular momentum. This is an unavoidable conclusion from basic comparisons between observational constraints and theoretical expectations, which for many years presented a major challenge to numerical simulations of galaxy formation, as these apparently predicted very low values for f_j . It has gradually been realized that such simulations overpredicted angular momentum transport (e.g., Keres et al. 2012), with major uncertainties still lingering in the baryonic physics included in the simulations.

Our consolidation of the f_j result for elliptical galaxies provides a new benchmark for models of galaxy evolution, which to be fully credible must reproduce the observed f_j (and f_\star) trends for both spirals and ellipticals *in the same simulation*. For example, any feedback processes that are invoked to prevent overcooling and j loss in spirals should be much less effective for ellipticals.

We have explored a few toy models for galaxy evolu-

tion that exploit the basic constraints provided by the parameter space of j_\star and M_\star , or equivalently of f_j and f_\star . Galaxies cannot evolve arbitrarily in this parameter space, requiring physically-motivated diagonal vectors of change ($\Delta j_\star, \Delta M_\star$). Thus we suggest the j - M diagram as a key tool for assessing and interpreting any model of galaxy formation.

Our simplified models suggest that a combination of early baryonic collapse and repeated galaxy merging (major or minor) might account for the parallel-but-offset trend of ellipticals relative to spirals. We have provided illustrative constraints on the numbers and mass-ratios of the mergers, which after refinement with more detailed modeling could be compared with cosmologically-based predictions for mass growth and merging.

In summary, we have established a new synthesis of $j_\star-M_\star$ trends from observations, whose general resemblance to halos in Λ CDM cosmology provides important support for that theory, and in turn furnishes a valuable framework for constraining baryonic processes as discussed above. Our course, the observations presented here must be relevant to any model of galaxy formation, even if Λ CDM theory eventually needs revision. More generally, we propose that the morphologies of galaxies are closely tied to the evolution of angular momentum during their assembly, with late-types being very efficient at retaining j , and early-types proficient at shedding j .

In this context, there are several areas ripe for additional progress. First, clear predictions from high-resolution cosmological simulations are needed for j_\star versus M_\star as a function of galaxy type, to explore whether the dichotomy between spirals and ellipticals, or disks and bulges, can be explained by differences in their assembly histories. Second, the observational work on nearby galaxies should be extended to the next level, via a volume-limited, homogeneous survey of all types of galaxies including full two-dimensional, wide-field photometric-kinematic bulge-disk decompositions, with attention to stellar mass-to-light ratio variations. This would allow for more robust analysis of the deviations of the j_\star residuals from lognormality, and for more secure treatments of S0/Sa galaxies and of bulge and disk subcomponents. Third, the extensions of our study to lower-mass (e.g., Kormendy & Bender 2012) as well as to higher-redshift galaxies (cf. Puech et al. 2007; Burkert et al. 2010), to freshly accreted material within galaxies (cf. Stewart et al. 2011), and to the orientations of the \mathbf{j}_\star vectors (e.g., Codis et al. 2012; Tempel et al. 2012), would provide additional, valuable diagnostics.

We thank Brad Whitmore for assistance with the spiral galaxy data compilation, and the referee for a constructive review. We thank Frank van den Bosch, Andi Burkert, Roger Davies, Aaron Dutton, George Efstathiou, Eric Emsellem, Ken Freeman, Marcel Haas, Phil Hopkins, Koen Kuijken, Surhud More, Joel Primack, and Mike Williams for helpful comments and discussions. This research was supported in part by the National Science Foundation under Grants No. AST-0507729, AST-0808099, AST-0909237, and PHY05-51164. This research has made use of the NASA/IPAC Extragalactic

Database (NED) which is operated by the Jet Propulsion Laboratory, California Institute of Technology, under contract with the National Aeronautics and Space Administration. This publication makes use of data products from the Two Micron All Sky Survey, which is a joint project of the University of Massachusetts and

the Infrared Processing and Analysis Center/California Institute of Technology, funded by the National Aeronautics and Space Administration and the National Science Foundation.

REFERENCES

- Aarseth, S. J., & Fall, S. M. 1980, *ApJ*, 236, 43
- Agertz, O., Teyssier, R., & Moore, B. 2011, *MNRAS*, 410, 1391
- Andreadakis, Y. C., & Sanders, R. H. 1994, *MNRAS*, 267, 283
- Antonuccio-Delogu, V., Dobrotka, A., Becciani, U., et al. 2010, *MNRAS*, 407, 1338
- Arnaboldi, M., Freeman, K. C., Gerhard, O., et al. 1998, *ApJ*, 507, 759
- Arnaboldi, M., Freeman, K. C., Hui, X., Capaccioli, M., & Ford, H. 1994, *The Messenger*, 76, 40
- Arnold, J. A., Romanowsky, A. J., Brodie, J. P., et al. 2011, *ApJ*, 736, L26
- Baldry, I. K., Glazebrook, K., Brinkmann, J., et al. 2004, *ApJ*, 600, 681
- Barnes, J., & Efstathiou, G. 1987, *ApJ*, 319, 575
- Barnes, J. E. 1988, *ApJ*, 331, 699
- . 1992, *ApJ*, 393, 484
- Bedregal, A. G., Aragón-Salamanca, A., Merrifield, M. R., & Milvang-Jensen, B. 2006, *MNRAS*, 371, 1912
- Begeman, K. G. 1989, *A&A*, 223, 47
- Behroozi, P. S., Conroy, C., & Wechsler, R. H. 2010, *ApJ*, 717, 379
- Bekki, K., & Peng, E. W. 2006, *MNRAS*, 370, 1737
- Bell, E. F., McIntosh, D. H., Katz, N., & Weinberg, M. D. 2003, *ApJS*, 149, 289
- Bender, R., & Nieto, J.-L. 1990, *A&A*, 239, 97
- Bershady, M. A., Martinsson, T. P. K., Verheijen, M. A. W., et al. 2011, *ApJ*, 739, L47
- Berta, Z. K., Jimenez, R., Heavens, A. F., & Panter, B. 2008, *MNRAS*, 391, 197
- Bertola, F., & Capaccioli, M. 1975, *ApJ*, 200, 439
- Bezanson, R., van Dokkum, P. G., Tal, T., et al. 2009, *ApJ*, 697, 1290
- Binney, J. 1978, *MNRAS*, 183, 501
- Binney, J., & Merrifield, M. 1998, *Galactic astronomy* (Princeton, NJ : Princeton University Press)
- Binney, J., Gerhard, O., & Silk, J. 2001, *MNRAS*, 321, 471
- Binney, J., & Tremaine, S. 2008, *Galactic Dynamics: Second Edition*, ed. Binney, J. & Tremaine, S. (Princeton Univ. Press)
- Blakeslee, J. P., Jordán, A., Mei, S., et al. 2009, *ApJ*, 694, 556
- Blanton, M. R., Hogg, D. W., Bahcall, N. A., et al. 2003, *ApJ*, 594, 186
- Blumenthal, G. R., Faber, S. M., Primack, J. R., & Rees, M. J. 1984, *Nature*, 311, 517
- Bois, M., Emsellem, E., Bournaud, F., et al. 2011, *MNRAS*, 416, 1654
- Bower, R. G., Benson, A. J., Malbon, R., et al. 2006, *MNRAS*, 370, 645
- Brodie, J. P., Romanowsky, A. J., Strader, J., & Forbes, D. A. 2011, *AJ*, 142, 199
- Brook, C. B., Governato, F., Roskar, R., et al. 2011, *MNRAS*, 415, 1051
- Brook, C. B., Stinson, G., Gibson, B. K., et al. 2012, *MNRAS*, 419, 771
- Bullock, J. S., Dekel, A., Kolatt, T. S., et al. 2001, *ApJ*, 555, 240
- Burkert, A. 2009, in *Astronomical Society of the Pacific Conference Series*, Vol. 419, *Galaxy Evolution: Emerging Insights and Future Challenges*, ed. S. Jogee, et al., 3
- Burkert, A., Naab, T., Johansson, P. H., & Jesseit, R. 2008, *ApJ*, 685, 897
- Burkert, A., Genzel, R., Bouché, N., et al. 2010, *ApJ*, 725, 2324
- Burkert, A. M., & D’Onghia, E. 2004, in *Astrophysics and Space Science Library*, Vol. 319, *Penetrating Bars Through Masks of Cosmic Dust*, ed. D. L. Block, et al., 341
- Caon, N., Capaccioli, M., & D’Onofrio, M. 1993, *MNRAS*, 265, 1013
- Cappellari, M., Emsellem, E., Bacon, R., et al. 2007, *MNRAS*, 379, 418
- Cappellari, M., Emsellem, E., Krajnović, D., et al. 2011a, *MNRAS*, 413, 813
- . 2011b, *MNRAS*, 416, 1680
- Cappellari, M., McDermid, R. M., Alatalo, K., et al. 2012, *Nature*, 484, 485
- Catelan, P., & Theuns, T. 1996, *MNRAS*, 282, 436
- Cervantes-Sodi, B., Hernandez, X., Park, C., & Kim, J. 2008, *MNRAS*, 388, 863
- Ceverino, D., Dekel, A., & Bournaud, F. 2010, *MNRAS*, 404, 2151
- Coccatto, L., Gerhard, O., Arnaboldi, M., et al. 2009, *MNRAS*, 394, 1249
- Codis, S., Pichon, C., Devriendt, J., et al. 2012, *MNRAS*, in press, arXiv:1201.5794
- Cohen, J. G., & Ryzhov, A. 1997, *ApJ*, 486, 230
- Cole, S., Aragón-Salamanca, A., Frenk, C. S., Navarro, J. F., & Zepf, S. E. 1994, *MNRAS*, 271, 781
- Cole, S., & Lacey, C. 1996, *MNRAS*, 281, 716
- Conroy, C., & Wechsler, R. H. 2009, *ApJ*, 696, 620
- Corsini, E. M., Pizzella, A., Sarzi, M., et al. 1999, *A&A*, 342, 671
- Cortesi, A. 2012, PhD thesis, Univ. Nottingham
- Cortesi, A., Merrifield, M. R., Arnaboldi, M., et al. 2011, *MNRAS*, 414, 642
- Croton, D. J., Springel, V., White, S. D. M., et al. 2006, *MNRAS*, 365, 11
- Cumming, A., Butler, R. P., Marcy, G. W., et al. 2008, *PASP*, 120, 531
- Dalcanton, J. J., Spergel, D. N., & Summers, F. J. 1997, *ApJ*, 482, 659
- Danovich, M., Dekel, A., Hahn, O., & Teyssier, R. 2012, *MNRAS*, 422, 1732
- Das, P., Gerhard, O., Mendez, R. H., Teodorescu, A. M., & de Lorenzi, F. 2011, *MNRAS*, 415, 1244
- Davé, R. 2008, *MNRAS*, 385, 147
- Davies, R. L., Efstathiou, G., Fall, S. M., Illingworth, G., & Schechter, P. L. 1983, *ApJ*, 266, 41
- de Jong, R. S., & Lacey, C. 2000, *ApJ*, 545, 781
- de Jong, R. S., Simard, L., Davies, R. L., et al. 2004, *MNRAS*, 355, 1155
- de Lorenzi, F., Gerhard, O., Coccatto, L., et al. 2009, *MNRAS*, 395, 76
- de Vaucouleurs, G. 1948, *Annales d’Astrophysique*, 11, 247
- de Vaucouleurs, G. 1961, *ApJS*, 5, 233
- de Vaucouleurs, G., de Vaucouleurs, A., Corwin, H. G., Jr., et al. 1991, Volume 1-3, XII, 2069 pp. 7 figs.. Springer-Verlag
- Dekel, A., Birnboim, Y., Engel, G., et al. 2009a, *Nature*, 457, 451
- Dekel, A., Sari, R., & Ceverino, D. 2009b, *ApJ*, 703, 785
- Devereux, N., Willner, S. P., Ashby, M. L. N., Willmer, C. N. A., & Hriljac, P. 2009, *ApJ*, 702, 955
- Disney, M. J., Romano, J. D., Garcia-Appadoo, D. A., et al. 2008, *Nature*, 455, 1082
- D’Onghia, E., & Burkert, A. 2004, *ApJ*, 612, L13
- D’Onghia, E., Burkert, A., Murante, G., & Khochfar, S. 2006, *MNRAS*, 372, 1525
- D’Onghia, E., & Navarro, J. F. 2007, *MNRAS*, 380, L58
- D’Onofrio, M. 2001, *MNRAS*, 326, 1517
- Dorman, C. E., Guhathakurta, P., Fardal, M. A., et al. 2012, *ApJ*, 752, 147
- Douglas, N. G., Napolitano, N. R., Romanowsky, A. J., et al. 2007, *ApJ*, 664, 257

- Dubois, Y., Pichon, C., Haehnelt, M., et al. 2012, *MNRAS*, 423, 3616
- Dutton, A. A., Conroy, C., van den Bosch, F. C., Prada, F., & More, S. 2010, *MNRAS*, 407, 2
- Dutton, A. A., Conroy, C., van den Bosch, F. C., et al. 2011, *MNRAS*, 416, 322
- Dutton, A. A., Mendel, J. T., & Simard, L. 2012, *MNRAS*, 422, L33
- Dutton, A. A., & van den Bosch, F. C. 2012, *MNRAS*, 421, 608
- Dutton, A. A., van den Bosch, F. C., Dekel, A., & Courteau, S. 2007, *ApJ*, 654, 27
- Elmegreen, B. G., Bournaud, F., & Elmegreen, D. M. 2008, *ApJ*, 688, 67
- Emsellem, E., Cappellari, M., Krajnović, D., et al. 2007, *MNRAS*, 379, 401
- . 2011, *MNRAS*, 414, 888
- Emsellem, E., Cappellari, M., Peletier, R. F., et al. 2004, *MNRAS*, 352, 721
- Erb, D. K., Steidel, C. C., Shapley, A. E., et al. 2006, *ApJ*, 646, 107
- Faber, S. M., & Jackson, R. E. 1976, *ApJ*, 204, 668
- Faber, S. M., Willmer, C. N. A., Wolf, C., et al. 2007, *ApJ*, 665, 265
- Fabricius, M. H., Saglia, R. P., Fisher, D. B., et al. 2012, *ApJ*, 754, 67
- Fakhouri, O., Ma, C.-P., & Boylan-Kolchin, M. 2010, *MNRAS*, 406, 2267
- Fall, S. M. 1979, *Nature*, 281, 200
- Fall, S. M. 1983, in *IAU Symposium*, Vol. 100, Internal Kinematics and Dynamics of Galaxies, ed. E. Athanassoula, 391 (F83)
- Fall, S. M. 2002, in *Astronomical Society of the Pacific Conference Series*, Vol. 275, Disks of Galaxies: Kinematics, Dynamics and Perturbations, ed. E. Athanassoula, A. Bosma, & R. Mujica, 389
- Fall, S. M., & Efstathiou, G. 1980, *MNRAS*, 193, 189
- Ferreras, I., La Barbera, F., de Carvalho, R. R., et al. 2012, *ApJ*, submitted, arXiv:1206.1594
- Fillmore, J. A., Boroson, T. A., & Dressler, A. 1986, *ApJ*, 302, 208
- Forbes, D. A., Cortesi, A., Pota, V., et al. 2012, *MNRAS*, submitted
- Forestell, A. D., & Gebhardt, K. 2010, *ApJ*, 716, 370
- Foster, C., Spitler, L. R., Romanowsky, A. J., et al. 2011, *MNRAS*, 415, 3393
- Franx, M. 1988, Ph.D. thesis, Univ. Leiden
- Freeman, K. C. 1970, *ApJ*, 160, 811
- Freeman, K., & Bland-Hawthorn, J. 2002, *ARA&A*, 40, 487
- Frenk, C. S., White, S. D. M., Efstathiou, G., & Davis, M. 1985, *Nature*, 317, 595
- Gadotti, D. A. 2009, *MNRAS*, 393, 1531
- Gardner, J. P. 2001, *ApJ*, 557, 616
- Gerhard, O. E. 1981, *MNRAS*, 197, 179
- Governato, F., Willman, B., Mayer, L., et al. 2007, *MNRAS*, 374, 1479
- Graham, A. W., Colless, M. M., Busarello, G., Zaggia, S., & Longo, G. 1998, *A&AS*, 133, 325
- Graham, A. W., & Guzmán, R. 2003, *AJ*, 125, 2936
- Graham, A. W., & Worley, C. C. 2008, *MNRAS*, 388, 1708
- Guedes, J., Callegari, S., Madau, P., & Mayer, L. 2011, *ApJ*, 742, 76
- Guhathakurta, P., van Gorkom, J. H., Kotanyi, C. G., & Balkowski, C. 1988, *AJ*, 96, 851
- Guo, Q., White, S., Li, C., & Boylan-Kolchin, M. 2010, *MNRAS*, 404, 1111
- Guthrie, B. N. G. 1992, *A&AS*, 93, 255
- Halliday, C., Davies, R. L., Kuntschner, H., et al. 2001, *MNRAS*, 326, 473
- Heavens, A., & Peacock, J. 1988, *MNRAS*, 232, 339
- Heidemann, N. 1969, *Astrophys. Lett.*, 3, 153
- Hernandez, X., Park, C., Cervantes-Sodi, B., & Choi, Y. 2007, *MNRAS*, 375, 163
- Hernquist, L. 1992, *ApJ*, 400, 460
- Hetznecker, H., & Burkert, A. 2006, *MNRAS*, 370, 1905
- Heyl, J. S., Hernquist, L., & Spiegel, D. N. 1996, *ApJ*, 463, 69
- Hopkins, P. F., Cox, T. J., Dutta, S. N., et al. 2009a, *ApJS*, 181, 135
- Hopkins, P. F., Lauer, T. R., Cox, T. J., Hernquist, L., & Kormendy, J. 2009b, *ApJS*, 181, 486
- Hoyle, F. 1951, in *Problems of Cosmical Aerodynamics*, 195
- Hubble, E. P. 1926, *ApJ*, 64, 321
- Hummels, C. B., & Bryan, G. L. 2012, *ApJ*, 749, 140
- Immeli, A., Samland, M., Westera, P., & Gerhard, O. 2004, *ApJ*, 611, 20
- Jesseit, R., Cappellari, M., Naab, T., Emsellem, E., & Burkert, A. 2009, *MNRAS*, 397, 1202
- Johansson, P. H., Naab, T., & Ostriker, J. P. 2012, *ApJ*, in press, arXiv:1202.3441
- Johnston, E. J., Aragón-Salamanca, A., Merrifield, M. R., & Bedregal, A. G. 2012, *MNRAS*, 422, 2590
- Jørgensen, I., & Franx, M. 1994, *ApJ*, 433, 553
- Kashlinsky, A. 1982, *MNRAS*, 200, 585
- Kassin, S. A., Devriendt, J., Fall, S. M., et al. 2012, *MNRAS*, 424, 502
- Katz, N., & Gunn, J. E. 1991, *ApJ*, 377, 365
- Kauffmann, G., & White, S. D. M. 1993, *MNRAS*, 261, 921
- Kent, S. M. 1986, *AJ*, 91, 1301
- . 1987, *AJ*, 93, 816
- . 1988, *AJ*, 96, 514
- Kepner, J. V. 1999, *ApJ*, 520, 59
- Keres, D., Vogelsberger, M., Sijacki, D., Springel, V., & Hernquist, L. 2012, *MNRAS*, submitted, arXiv:1109.4638
- Khochfar, S., Emsellem, E., Serra, P., et al. 2011, *MNRAS*, 417, 845
- Kimm, T., Devriendt, J., Slyz, A., et al. 2012, *MNRAS*, submitted, arXiv:1106.0538
- Kissler-Patig, M., & Gebhardt, K. 1998, *AJ*, 116, 2237
- Komatsu, E., Smith, K. M., Dunkley, J., et al. 2011, *ApJS*, 192, 18
- Kormendy, J. 1982, in *Saas-Fee Advanced Course 12: Morphology and Dynamics of Galaxies*, ed. L. Martinet & M. Mayor, 113
- Kormendy, J., & Bender, R. 1996, *ApJ*, 464, L119
- Kormendy, J., & Bender, R. 2012, *ApJS*, 198, 2
- Kormendy, J., Fisher, D. B., Cornell, M. E., & Bender, R. 2009, *ApJS*, 182, 216
- Kormendy, J., & Illingworth, G. 1982, *ApJ*, 256, 460
- Kormendy, J., & Kennicutt, Jr., R. C. 2004, *ARA&A*, 42, 603
- Krajnović, D., Bacon, R., Cappellari, M., et al. 2008, *MNRAS*, 390, 93
- Krajnović, D., Cappellari, M., de Zeeuw, P. T., & Copin, Y. 2006, *MNRAS*, 366, 787
- Kroupa, P. 2001, *MNRAS*, 322, 231
- Lacey, C., Guiderdoni, B., Rocca-Volmerange, B., & Silk, J. 1993, *ApJ*, 402, 15
- Larson, R. B., Tinsley, B. M., & Caldwell, C. N. 1980, *ApJ*, 237, 692
- Laurikainen, E., Salo, H., Buta, R., & Knapen, J. H. 2007, *MNRAS*, 381, 401
- Laurikainen, E., Salo, H., Buta, R., & Knapen, J. H. 2011, *Advances in Astronomy*, 2011, 516739
- Laurikainen, E., Salo, H., Buta, R., Knapen, J. H., & Comerón, S. 2010, *MNRAS*, 405, 1089
- Law, D. R., Steidel, C. C., Erb, D. K., et al. 2009, *ApJ*, 697, 2057
- Lemson, G., & Kauffmann, G. 1999, *MNRAS*, 302, 111
- MacArthur, L. A., González, J. J., & Courteau, S. 2009, *MNRAS*, 395, 28
- Macciò, A. V., Dutton, A. A., & van den Bosch, F. C. 2008, *MNRAS*, 391, 1940
- Macciò, A. V., Dutton, A. A., van den Bosch, F. C., et al. 2007, *MNRAS*, 378, 55
- Mahdavi, A., Trentham, N., & Tully, R. B. 2005, *AJ*, 130, 1502
- Maller, A. H., Dekel, A., & Somerville, R. 2002, *MNRAS*, 329, 423
- Maltby, D. T., Aragón-Salamanca, A., Gray, M. E., et al. 2010, *MNRAS*, 402, 282
- Marinacci, F., Fraternali, F., Nipoti, C., et al. 2011, *MNRAS*, 415, 1534
- Marinoni, C., & Hudson, M. J. 2002, *ApJ*, 569, 101
- Márquez, I., Lima Neto, G. B., Capelato, H., Durret, F., & Gerbal, D. 2000, *A&A*, 353, 873
- Masters, K. L., Springob, C. M., & Huchra, J. P. 2008, *AJ*, 135, 1738
- McDonald, M., Courteau, S., Tully, R. B., & Roediger, J. 2011, *MNRAS*, 414, 2055

- McNeil, E. K., Arnaboldi, M., Freeman, K. C., et al. 2010, *A&A*, 518, A44
- McNeil-Moylan, E. K., Freeman, K. C., Arnaboldi, M., & Gerhard, O. E. 2012, *A&A*, 539, A11
- Melioli, C., Brighenti, F., D'Ercole, A., & de Gouveia Dal Pino, E. M. 2009, *MNRAS*, 399, 1089
- Méndez-Abreu, J., Aguerra, J. A. L., Corsini, E. M., & Simonneau, E. 2008, *A&A*, 487, 555
- Mo, H. J., Mao, S., & White, S. D. M. 1998, *MNRAS*, 295, 319
- More, S., van den Bosch, F. C., Cacciato, M., et al. 2011, *MNRAS*, 410, 210
- Morelli, L., Pompei, E., Pizzella, A., et al. 2008, *MNRAS*, 389, 341
- Moster, B. P., Somerville, R. S., Maulbetsch, C., et al. 2010, *ApJ*, 710, 903
- Moster, B. P., Naab, T., & White, S. D. M. 2012, *MNRAS*, submitted, arXiv:1205.5807
- Naab, T., Johansson, P. H., & Ostriker, J. P. 2009, *ApJ*, 699, L178
- Napolitano, N. R., Romanowsky, A. J., Coccato, L., et al. 2009, *MNRAS*, 393, 329
- Napolitano, N. R., Romanowsky, A. J., Capaccioli, M., et al. 2011, *MNRAS*, 411, 2035
- Navarro, J. F., & Benz, W. 1991, *ApJ*, 380, 320
- Navarro, J. F., Frenk, C. S., & White, S. D. M. 1995, *MNRAS*, 275, 56
- . 1996, *ApJ*, 462, 563
- Navarro, J. F., & Steinmetz, M. 1997, *ApJ*, 478, 13
- . 2000, *ApJ*, 538, 477
- Navarro, J. F., & White, S. D. M. 1994, *MNRAS*, 267, 401
- Neistein, E., Maoz, D., Rix, H., & Tonry, J. L. 1999, *AJ*, 117, 2666
- Noguchi, M. 1999, *ApJ*, 514, 77
- Noordermeer, E., & Verheijen, M. A. W. 2007, *MNRAS*, 381, 1463
- Nordsieck, K. H. 1973, *ApJ*, 184, 735
- Norris, M. A., Gebhardt, K., Sharples, R. M., et al. 2012, *MNRAS*, 421, 1485
- Oser, L., Ostriker, J. P., Naab, T., Johansson, P. H., & Burkert, A. 2010, *ApJ*, 725, 2312
- Oser, L., Naab, T., Ostriker, J. P., & Johansson, P. H. 2012, *ApJ*, 744, 63
- Parry, O. H., Eke, V. R., & Frenk, C. S. 2009, *MNRAS*, 396, 1972
- Paturel, G., Petit, C., Prugniel, P., et al. 2003, *A&A*, 412, 45
- Peebles, P. J. E. 1969, *ApJ*, 155, 393
- Peirani, S., Mohayaee, R., & de Freitas Pacheco, J. A. 2004, *MNRAS*, 348, 921
- Peletier, R. F., Davies, R. L., Illingworth, G. D., Davis, L. E., & Cawson, M. 1990, *AJ*, 100, 1091
- Peng, E. W., Ford, H. C., & Freeman, K. C. 2004, *ApJ*, 602, 685
- Pinkney, J., Gebhardt, K., Bender, R., et al. 2003, *ApJ*, 596, 903
- Pizzella, A., Corsini, E. M., Vega Beltrán, J. C., & Bertola, F. 2004, *A&A*, 424, 447
- Pota, V., Forbes, D. A., Romanowsky, A. J., et al. 2012, *MNRAS*, submitted
- Primack, J. R. 2005, *New Astronomy Reviews*, 49, 25
- Proctor, R. N., Forbes, D. A., Forestell, A., & Gebhardt, K. 2005, *MNRAS*, 362, 857
- Proctor, R. N., Forbes, D. A., Romanowsky, A. J., et al. 2009, *MNRAS*, 398, 91
- Prugniel, P., & Simien, F. 1997, *A&A*, 321, 111
- Puech, M., Hammer, F., Lehnert, M. D., & Flores, H. 2007, *A&A*, 466, 83
- Reed, D., Governato, F., Quinn, T., et al. 2005, *MNRAS*, 359, 1537
- Rix, H., Carollo, C. M., & Freeman, K. 1999, *ApJ*, 513, L25
- Roediger, J. C., Courteau, S., McDonald, M., & MacArthur, L. A. 2011, *MNRAS*, 416, 1983
- Romanowsky, A. J. 2006, in *Planetary Nebulae Beyond the Milky Way*, ed. L. Stanghellini, J. R. Walsh, & N. G. Douglas, 294
- Romanowsky, A. J., Douglas, N. G., Kuijken, K., et al. 2004, in *Dark Matter in Galaxies*, ed. S. Ryder, D. Pisano, M. Walker, & K. Freeman, 220, 165
- Romanowsky, A. J., & Kochanek, C. S. 1997, *MNRAS*, 287, 35
- Romanowsky, A. J., Strader, J., Brodie, J. P., et al. 2012, *ApJ*, 748, 29
- Romanowsky, A. J., Strader, J., Spitler, L. R., et al. 2009, *AJ*, 137, 4956
- Rothberg, B., & Joseph, R. D. 2006, *AJ*, 132, 976
- Rubin, V. C., Burstein, D., Ford, Jr., W. K., & Thonnard, N. 1985, *ApJ*, 289, 81
- Rubin, V. C., Ford, Jr., W. K., Thonnard, N., & Burstein, D. 1982, *ApJ*, 261, 439
- Rubin, V. C., Ford, W. K. J., & Thonnard, N. 1980, *ApJ*, 238, 471
- Sales, L. V., Navarro, J. F., Theuns, T., et al. 2012, *MNRAS*, 423, 1544
- Salpeter, E. E. 1955, *ApJ*, 121, 161
- Sambhus, N., Gerhard, O., & Méndez, R. H. 2006, *AJ*, 131, 837
- Sánchez-Blázquez, P., Forbes, D. A., Strader, J., Brodie, J., & Proctor, R. 2007, *MNRAS*, 377, 759
- Scannapieco, C., Tissera, P. B., White, S. D. M., & Springel, V. 2008, *MNRAS*, 389, 1137
- Scannapieco, C., Wadepuhl, M., Parry, O. H., et al. 2012, *MNRAS*, 423, 1726
- Schombert, J. 2011, arXiv:1107.1728
- Scorza, C., & Bender, R. 1995, *A&A*, 293, 20
- Sérsic, J. L. 1968, *Atlas de galaxias australes (Cordoba, Argentina: Observatorio Astronomico, 1968)*
- Sharma, S., & Steinmetz, M. 2005, *ApJ*, 628, 21
- Sharma, S., Steinmetz, M., & Bland-Hawthorn, J. 2012, *ApJ*, 750, 107
- Shaya, E. J., & Tully, R. B. 1984, *ApJ*, 281, 56
- Shen, B. S., Mo, H. J., White, S. D. M., et al. 2007, *MNRAS*, 379, 400
- Shen, S., Mo, H. J., White, S. D. M., et al. 2003, *MNRAS*, 343, 978
- Silge, J. D., & Gebhardt, K. 2003, *AJ*, 125, 2809
- Silva, D. R., Kuntschner, H., & Lyubenova, M. 2008, *ApJ*, 674, 194
- Simien, F., & de Vaucouleurs, G. 1986, *ApJ*, 302, 564
- Simien, F., & Prugniel, P. 1997a, *A&AS*, 122, 521
- . 1997b, *A&AS*, 126, 15
- Skrutskie, M. F., Cutri, R. M., Stiening, R., et al. 2006, *AJ*, 131, 1163
- Smith, R. J., Lucey, J. R., & Carter, D. 2012, *MNRAS*, submitted, arXiv:1206.4311
- Somerville, R. S., & Primack, J. R. 1999, *MNRAS*, 310, 1087
- Sommer-Larsen, J., Götz, M., & Portinari, L. 2003, *ApJ*, 596, 47
- Spolaor, M., Hau, G. K. T., Forbes, D. A., & Couch, W. J. 2010, *MNRAS*, 408, 254
- Steinmetz, M., & Bartelmann, M. 1995, *MNRAS*, 272, 570
- Stewart, K. R., Bullock, J. S., Wechsler, R. H., Maller, A. H., & Zentner, A. R. 2008, *ApJ*, 683, 597
- Stewart, K. R., Kaufmann, T., Bullock, J. S., et al. 2011, *ApJ*, 738, 39
- Strader, J., Romanowsky, A. J., Brodie, J. P., et al. 2011, *ApJS*, 197, 33
- Takase, B., & Kinoshita, H. 1967, *PASJ*, 19, 409
- Tempel, E., Stoica, R. S., & Saar, E. 2012, *MNRAS*, submitted, arXiv:1207.0068
- Tonry, J. L., Dressler, A., Blakeslee, J. P., et al. 2001, *ApJ*, 546, 681
- Toomre, A. 1964, *ApJ*, 139, 1217
- Toomre, A. 1977, in *Evolution of Galaxies and Stellar Populations*, ed. B. M. Tinsley & R. B. Larson, 401
- Torrey, P., Vogelsberger, M., Sijacki, D., Springel, V., & Hernquist, L. 2012, *MNRAS*, submitted, arXiv:1110.5635
- Tortora, C., Napolitano, N. R., Romanowsky, A. J., Capaccioli, M., & Covone, G. 2009, *MNRAS*, 396, 1132
- Tortora, C., Napolitano, N. R., Romanowsky, A. J., & Jetzer, P. 2010, *ApJ*, 721, L1
- Tortora, C., Napolitano, N. R., Romanowsky, A. J., et al. 2011, *MNRAS*, 418, 1557
- Treu, T., Auger, M. W., Koopmans, L. V. E., et al. 2010, *ApJ*, 709, 1195
- Trujillo-Gomez, S., Klypin, A., Primack, J., & Romanowsky, A. J. 2011, *ApJ*, 742, 16
- Tully, R. B., & Fisher, J. R. 1977, *A&A*, 54, 661
- van den Bosch, F. C. 1998, *ApJ*, 507, 601
- van den Bosch, F. C., Burkert, A., & Swaters, R. A. 2001, *MNRAS*, 326, 1205
- van Dokkum, P. G., & Conroy, C. 2011, *ApJ*, 735, L13
- van Uiter, E., Hoekstra, H., Velander, M., et al. 2011, *A&A*, 534, A14

- Vanderbeke, J., Baes, M., Romanowsky, A. J., & Schmidtobreick, L. 2011, *MNRAS*, 412, 2017
- Vitvitska, M., Klypin, A. A., Kravtsov, A. V., et al. 2002, *ApJ*, 581, 799
- Weijmans, A.-M., Cappellari, M., Bacon, R., et al. 2009, *MNRAS*, 398, 561
- Weil, M. L., Eke, V. R., & Efstathiou, G. 1998, *MNRAS*, 300, 773
- White, S. D. M., & Rees, M. J. 1978, *MNRAS*, 183, 341
- White, S. D. M., & Frenk, C. S. 1991, *ApJ*, 379, 52
- Whitmore, B. C., Rubin, V. C., & Ford, Jr., W. K. 1984, *ApJ*, 287, 66
- Wilkinson, A., Sharples, R. M., Fosbury, R. A. E., & Wallace, P. T. 1986, *MNRAS*, 218, 297
- Williams, M. J., Bureau, M., & Cappellari, M. 2009, *MNRAS*, 400, 1665
- . 2010, *MNRAS*, 409, 1330
- Yang, X., Mo, H. J., & van den Bosch, F. C. 2003, *MNRAS*, 339, 1057
- Young, P., Lynds, C. R., Sargent, W. L. W., Boksenberg, A., & Hartwick, F. D. A. 1978, *ApJ*, 222, 450
- Zasov, A. V. 1985, *Soviet Astronomy Letters*, 11, 277
- Zavala, J., Okamoto, T., & Frenk, C. S. 2008, *MNRAS*, 387, 364
- Zibetti, S., Charlot, S., & Rix, H. 2009, *MNRAS*, 400, 1181
- Zurek, W. H., Quinn, P. J., & Salmon, J. K. 1988, *ApJ*, 330, 519

APPENDIX

APPENDIX A: ANGULAR MOMENTUM FORMULAE

A.1. General formulae

We begin with the description of a galaxy as the six-dimensional phase-space distribution function of its particles (gas and stars) $f(\mathbf{r}, \mathbf{v})$, where \mathbf{r} and \mathbf{v} are the (vector) position and velocity coordinates relative to the galactic center, and f is normalized to unity when integrated over all positions and velocities. Given a total mass M , the three-dimensional spatial mass density at position \mathbf{r} is

$$\rho(\mathbf{r}) = M \int f(\mathbf{r}, \mathbf{v}) d^3 \mathbf{v}, \quad (\text{A1})$$

and the mean velocity at that position is

$$\bar{\mathbf{v}}(\mathbf{r}) = \frac{M}{\rho(\mathbf{r})} \int \mathbf{v} f(\mathbf{r}, \mathbf{v}) d^3 \mathbf{v}. \quad (\text{A2})$$

The true (i.e., not projected) specific angular momentum is then

$$\mathbf{j}_t \equiv \frac{\mathbf{J}_t}{M} = \frac{\int \mathbf{r} \times \bar{\mathbf{v}}(\mathbf{r}) \rho(\mathbf{r}) d^3 \mathbf{r}}{\int \rho(\mathbf{r}) d^3 \mathbf{r}}. \quad (\text{A3})$$

Given the loss of information in observed galaxies (one positional dimension lost in projection, and two velocity dimensions usually unmeasurable as proper motions), one must adopt some simplifying assumptions in order to recover \mathbf{j}_t from observations. Our main assumptions here are that galaxies are transparent, have *axisymmetric* density distributions, and *rotate on cylinders* that are aligned with the symmetry axis of the density (with no other net velocity component such as expansion or contraction).

Adopting cylindrical galactic coordinates (R, z, ϕ) , our modeling assumptions imply that $\bar{\mathbf{v}}(\mathbf{r})$ becomes a simple rotation-velocity profile $v_{\text{rot},t}(R) \hat{\phi}$, independent of z and ϕ (where $\hat{\phi}$ is the unit vector in the azimuthal direction), and that the density $\rho(R, z)$ is independent of ϕ . Equation (A3) then reduces to a one-dimensional integral:

$$j_t = \frac{\int v_{\text{rot},t}(R) \Sigma(R) R^2 dR}{\int \Sigma(R) R dR}, \quad (\text{A4})$$

where

$$\Sigma(R) = \int \rho(R, z) dz \quad (\text{A5})$$

is the surface mass density when the galaxy is viewed pole-on. With these assumptions, all galaxies with the same $v_{\text{rot},t}(R)$ rotational profile and the same pole-on $\Sigma(R)$ have the same \mathbf{j}_t , e.g., whether they are thin disks or round spheroids.

Even under these fairly restrictive assumptions, recovering the true angular momentum of an observed galaxy is a difficult inverse problem. Fortunately, there is a way to structure the problem that makes it conceptually and computationally simpler. We separate the calculation for j_t into two factors:

$$j_t = C_i j_p. \quad (\text{A6})$$

Here the second factor on the right is the analogue of Equation (A4) constructed *purely from observations* along the projected semi-major axis x :

$$j_p \equiv \frac{\int v_{\text{rot},p}(x) \Sigma(x) x^2 dx}{\int \Sigma(x) x dx}. \quad (\text{A7})$$

Note that this “projected specific angular momentum” is *not* literally the projection of \mathbf{j}_t on the plane of the sky (which we will discuss at the end of this subsection). Also, the two denominators in Equations (A4) and (A7) are closely related. In the case of spherical symmetry for the density, they are identical, and for now we will adopt this assumption for simplicity, returning to the more general axisymmetric case later.

The first factor in Equation (A6), C_i , is a numerical coefficient incorporating all of the additional deprojection effects that depend on inclination and on the shapes (but not the amplitudes) of the surface density profile and of the rotation-velocity curve. Substituting Equations (A4) and (A7) into Equation (A6), we have

$$C_i = \frac{\int v_{\text{rot},t}(R) \Sigma(R) R^2 dR}{\int v_{\text{rot},p}(x) \Sigma(x) x^2 dx}. \quad (\text{A8})$$

Before manipulating Equation (A8) further, we point out that the advantage of this formulation of the angular momentum problem is that the complicated expression C_i need not be evaluated for every individual galaxy—provided that it is not sensitive to the details of the density and rotation-velocity profiles, and instead depends primarily on

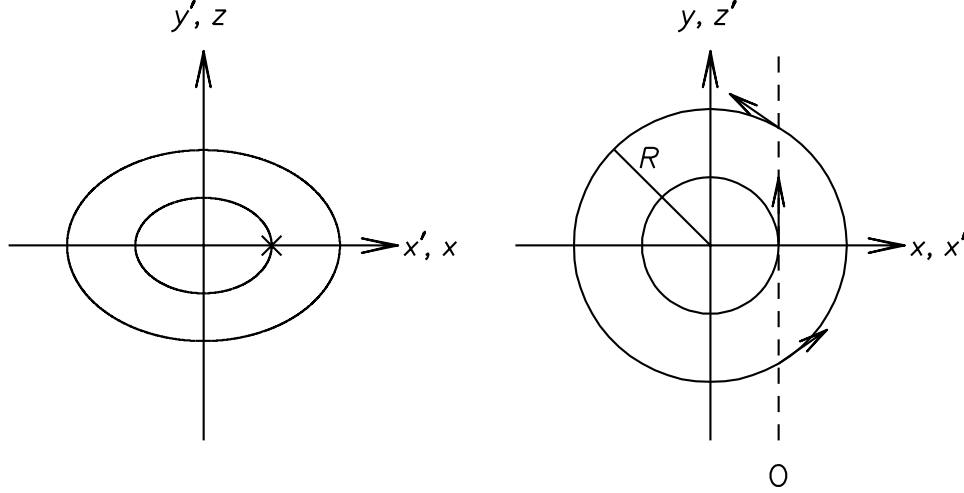


FIG. 23.— Geometry and coordinate systems for the calculation of the deprojection factor C_i . Here the galaxy is spheroidal and axisymmetric, with an inclination of $i = \pi/2$ (edge-on). The left-hand diagram shows the observer reference frame (x', y', z') , while the right-hand diagram shows the galaxy reference frame (x, y, z) . An example line-of-sight observation is illustrated by the \times symbol on the left, and by the dashed line on the right leading to the O symbol. The arrows tangential to the circles show sample rotation-velocity vectors. More general inclinations are similar, but with the line-of-sight components of the rotation reduced by factors of $\sin i$.

the inclination. Using simple models below, we will verify that this is the case, so that we can treat C_i as a numerical coefficient (calibrated by models) that we combine with the observables in Equation (A7), and thereby reconstruct j_t using Equation (A6).

Next, to derive a more specific expression for C_i , we begin by considering a galaxy observed from an arbitrary direction, which we characterize by the usual inclination i , the angle between the rotation axis z and the line-of-sight. The observer's reference frame is (x', y', z') , where z' is the line-of-sight (measured away from the observer), and x' is aligned with x for convenience (see Figure 23). Since we are adopting an approach of modeling rotation-velocity profiles along the observed semi-major axis, we simplify the problem by doing calculations only for the case $y' = 0$. The coordinate transformations between galaxy and observer frames are then

$$x = x' \quad (\text{A9})$$

$$y = -z' \sin i \quad (\text{A10})$$

$$z = z' \cos i \quad (\text{A11})$$

(see Romanowsky & Kochanek 1997 for more general expressions). The azimuthal unit vector in the galaxy frame can be expressed as

$$\hat{\phi} = \sin \phi \hat{x} + \cos \phi \hat{y}, \quad (\text{A12})$$

which after using unit-vector relations analogous to Equations (A9) and (A10), becomes

$$\hat{\phi} = \sin \phi \hat{x}' - \cos \phi \sin i \hat{z}'. \quad (\text{A13})$$

For a given parcel of material, the observer can measure only the projection of the mean velocity vector onto the line-of-sight, which we express as a dot product:

$$v_p = \bar{\mathbf{v}}(\mathbf{r}) \cdot \hat{\mathbf{z}}' = v_{\text{rot,t}}(R) \hat{\phi} \cdot \hat{\mathbf{z}}'. \quad (\text{A14})$$

From Equation (A13), we then find

$$v_p = -v_{\text{rot,t}}(R) \cos \phi \sin i = -v_{\text{rot,t}}(R) \frac{x}{R} \sin i, \quad (\text{A15})$$

where we use Equations (A9) and (A10) to make the substitution $R \equiv (x^2 + z'^2 \sin^2 i)^{1/2}$. We thus define a projected profile of rotation velocity along the semi-major axis:

$$v_{\text{rot,p}}(x) \equiv -v_p(x), \quad (\text{A16})$$

which we calculate by integrating Equation (A15) along the line-of-sight z' while weighting by the density $\rho(\mathbf{r})$. Recalling also that for now, we are assuming spherical symmetry for the density, we find the projected rotation-velocity profile

$$v_{\text{rot,p}}(x) = \frac{x \sin i \int \rho(r) v_{\text{rot,t}}(R) R^{-1} dz'}{\int \rho(r) dz'}, \quad (\text{A17})$$

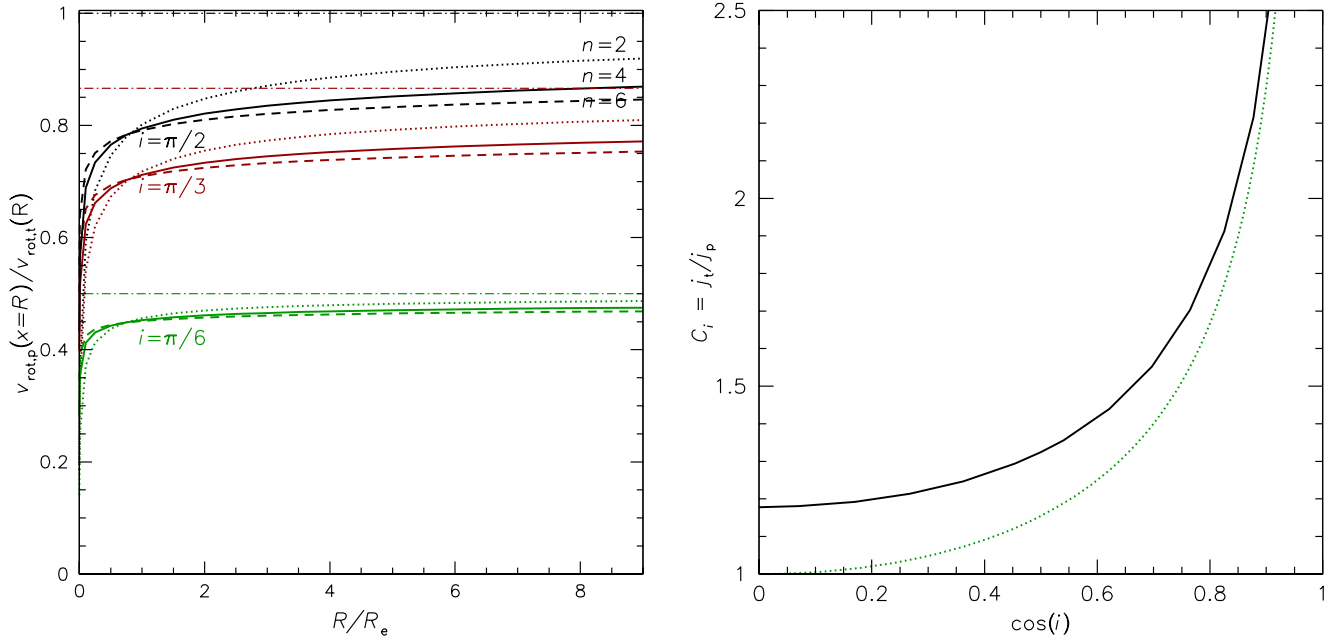


FIG. 24.— Relations between true and observed properties of idealized spherical galaxies with flat intrinsic rotation-velocity profiles. *Left:* Ratio of observed to true rotation velocity, vs. galactocentric distance, in units of the effective radius. Three different density profiles are used, with different line-styles and their Sérsic n indices labeled in the plot. Three inclinations are also used, with different colors, as labeled in the plot. The horizontal dot-dashed lines show the results if the dilution effect is ignored. We have verified that we reproduce related results from the literature (Binney 1978; Young et al. 1978). *Right:* Ratio of the true specific angular momentum to the value estimated by using the observed rotation-velocity profile [Equation (A7)], as a function of the cosine of the inclination. The black solid curve includes the dilution effect, while the green dotted one does not.

where we can also substitute $r = (x^2 + z'^2)^{1/2}$. The denominator is the surface density [Equation (A5)], and we have

$$v_{\text{rot,p}}(x) = \frac{x \sin i}{\Sigma(x)} \int \rho(r) v_{\text{rot,t}}(R) \frac{dz'}{R}. \quad (\text{A18})$$

There are a couple of notable features about Equations (A15) and (A18). One is that the difference between true and observed rotation velocity is more than a simple matter of the “ $\sin i$ ” inclination effect for a galaxy tilted away from edge-on. For a system of finite thickness, there is an additional $\cos \phi$ term that represents a “dilution” effect (cf. Binney 1978; Young et al. 1978; Fillmore et al. 1986; Neistein et al. 1999), corresponding to the projection of a circular orbit seen at varying azimuth ϕ (see Figure 23). Even for an edge-on case, the rotation vector is not in the line-of-sight except at the tangent point for a given semi-major axis distance x . This effect also implies that even if the true rotation velocity ($v_{\text{rot,t}}$) is constant with radius, the projected rotation velocity ($v_{\text{rot,p}}$) is generally *not*, and goes to zero toward the center of the galaxy (see left-hand panel of Figure 24 for examples).

Next, using Equation (A18), we find our final value for the numerical coefficient,

$$C_i = \frac{\int v_{\text{rot,t}}(R) \Sigma(R) R^2 dR}{\sin i \int x^3 dx \int \rho(r) v_{\text{rot,t}}(R) R^{-1} dz'}, \quad (\text{A19})$$

where $\rho(r)$ can in principle also be written in terms of the directly observed profile $\Sigma(x)$ via an Abel integral.

Having arrived at our general expressions for calculating j_t , we note that there is another, related approach found in the literature. This is to construct an observational analogue to \mathbf{j}_t , using the data directly to calculate a two-dimensional cross-product in an expression similar to (A3) (Franx 1988; Emsellem et al. 2007; Jesseit et al. 2009). This technique has the merit of potentially providing a general characterization of the data, including non-axisymmetric rotation fields. We have experimented with this approach and found that the fairly small improvement in accuracy (assuming the availability of full two-dimensional data) comes with the price of added complexity, while it also becomes unclear how to connect the results to the true three-dimensional angular momentum \mathbf{j}_t , which is our concern here.

A.2. Thin disks

Following the general framework above, we continue with more specific galaxy models. For context, we begin with the simple case of an infinitely thin disk that has a constant intrinsic rotation-velocity profile, which is the same as the circular velocity, $v_{\text{rot}}(R) = v_c(R)$. It also has an exponential pole-on surface density profile:

$$\Sigma(R) \propto \exp(-R/R_d), \quad (\text{A20})$$

where R_d is the disk scale-length. Using Equation (A4), we find

$$j_t = 2 v_c R_d = 1.19 v_c R_e, \quad (\text{A21})$$

where R_e is the radius enclosing half of the light of a face-on disk. and we have used the relation $R_e = 1.68 R_d$ for an exponential profile (note that for other disk inclinations, the observed half-light radius is smaller). Because the disk is infinitesimally thick, there is no dilution, except for a perfectly edge-on case, and we have simply $C_i = (\sin i)^{-1}$. This means that the observed (constant) rotation velocity is $v_s = v_c \sin i$, and we can map between observations and true specific angular momentum by the relation

$$j_t = \frac{2 v_s R_d}{\sin i}. \quad (\text{A22})$$

Using the notation of Equation (A6), we may say alternatively that $j_p = 2 v_s R_d$ and $C_i = (\sin i)^{-1}$. The exception is the perfectly edge-on case ($i = \pi/2$), where we find by constructing the appropriate analogues to Equations (A4) and (A7) that $C_i = 2$.

Real disks do have finite thickness and consequently an appreciable amount of observed rotation-velocity dilution toward their centers, even for $i < 90^\circ$. Still, detailed formulae like (A6)–(A19) are not really necessary, and as we verify in the main text, one can instead arrive at a very good approximation to j_t by taking the maximum or asymptotic rotation velocity observed at large radii to be v_s , which is then used in Equation (A22).

For a disk galaxy it is fairly straightforward to estimate the inclination i based on the apparent axial ratio q , using the formula

$$\sin i = \left(\frac{1 - q^2}{1 - q_i^2} \right)^{1/2}, \quad (\text{A23})$$

where we adopt an intrinsic axis ratio of $q_i = 0.11$ (e.g., Guthrie 1992). However, in order to tie in with spheroidal galaxies, we first treat i as an unknown for individual galaxies, so that a “typical” j_t is recovered by statistical deprojection of an ensemble of galaxies. One approach is to consider the *median* case C_{med} , where for randomly oriented galaxies, half of them have $C_i < C_{\text{med}}$; this is equivalent to identifying the median value for i . Since random inclinations in an axisymmetric geometry are distributed uniformly in $\cos i$, the median is $i = \pi/3$, which corresponds to $C_{\text{med}} = 2/\sqrt{3} \simeq 1.15$.

One may ask instead what is the *average* inclination correction, C_{avg} , which if applied uniformly to all observed galaxies would provide the correct ensemble average for j_t . Interestingly, the answer appears to depend on the exact question being posed. One may start in the reference frame of a galaxy (or planetary system) and ask what the average projection is (cf. Cumming et al. 2008; Law et al. 2009). Or one may start with the *observations* and estimate the average *deprojection* (e.g., Erb et al. 2006). In the spirit of mapping from projected to intrinsic quantities, we take the latter approach as follows.

The average value of j_t is calculated as an expectation value of a probability distribution:

$$\langle j_t \rangle = \int j_t \frac{dP}{dj_t} dj_t. \quad (\text{A24})$$

We consider a single observation j_p with infinitesimally small uncertainties, and since the probability P is uniform in $\cos i$, we recast this equation (see Equation (A6)) as

$$\langle C_i \rangle = \int C_i \sin i di. \quad (\text{A25})$$

Given $C_i = (\sin i)^{-1}$ for a thin disk, we then find $C_{\text{avg}} = \langle C_i \rangle = \pi/2 \simeq 1.57$. The equivalent calculation using the average *projection* yields $C_{\text{avg}} = \langle C_i^{-1} \rangle^{-1} = 4/\pi \simeq 1.27$. These two alternative correction factors differ by 23% or 0.09 dex, which will be a relatively minor concern in our overall j_t analysis. In the main text, we analyze a sample of spiral galaxies where the deprojections are known; because this sample is chosen to be avoid galaxies that are near face-on, the different options for averaging or medianing imply very similar values for C , and we cannot distinguish a best choice. In any case, the important point is to carry out *relative* comparisons of disk and spheroidal galaxies using the *same* deprojection approach, which we choose to do using median inclinations.

A.3. Spheroids

We next consider rotating spheroids, with the goals of (1) calculating the coefficient C_i to be used in combination with observational estimates of j_p in Equation (A6); (2) deriving an even simpler, more approximate expression for j_p that avoids the detailed calculation of Equation (A7). We assume spherical symmetry for now, and adopt the general Sérsic (1968) law for surface density profiles,

$$\Sigma(R) \propto \exp \left[-b_n (R/R_e)^{1/n} \right], \quad (\text{A26})$$

where the shape index n determines the steepness of the outer density profile (higher values are shallower: $n = 1$ is an exponential profile, $n = 4$ is a de Vaucouleurs law), and the numerical coefficient is

$$b_n \simeq 2n - 1/3 + 0.009876/n \quad (\text{A27})$$

(Márquez et al. 2000). Approximate analytical deprojection formulae for $\rho(r)$ are also provided in the preceding reference.

If we somehow knew the intrinsic rotation-velocity profile $v_{\text{rot,t}}(R)$, it would be straightforward to evaluate Equation (A4) and find j_t . For example, a de Vaucouleurs ($n = 4$) model with constant intrinsic rotation velocity v_t would yield:

$$j_t = 2.29 v_t R_e \quad (\text{A28})$$

(cf. Zasov 1985). To deal with the projection effects, we begin by adopting a constant intrinsic rotation velocity, and calculate C_i using Equation (A19). We find that C_i depends only on i , and not on n (Figure 24, right). The inclination dependence is weaker than $C_i \propto (\sin i)^{-1}$, which means it is partially counteracted by the dilution effect. An example is the edge-on case ($i = \pi/2$), for which we find $C_i = 1.18$, as compared with $C_i = 1$ if dilution were neglected.²⁶ We performed the same tests for rotation-velocity profiles that vary smoothly with radius and found very similar results. For example, C_i has only a $\sim 10\%$ dependence on the details of the rotation-velocity profile in Equation (A19).

The implication is that given observations of spherical galaxies, we can recover an accurate estimate of j_t using Equation (A6) and (A7), where C_i is a numerical factor that depends only on inclination. A simple expression for C_i that is accurate to better than 3% everywhere is:

$$C_i \simeq \frac{0.99 + 0.14 i}{\sin i}, \quad (\text{A29})$$

where i in the numerator is in radians. Note that this expression for C_i differs from the undiluted value by no more than 20%, which might suggest that we ignore the dilution effect in our studies of j_t , but we include it because we want to avoid collecting multiple systematic errors of this level.

In practice, we do not usually know the individual inclinations of spheroidal galaxies, and instead need to do a statistical deprojection as introduced above for disk galaxies. Considering the median case ($i = \pi/3$), we find $C_{\text{med}} = 1.32$. For the inclination averaged value, we again use Equation (A25) but with the spheroidal expression for C_i [Equation (A19), where in practice only the denominator is affected by the inclination averaging]. We find $C_{\text{avg}} = \langle C_i^{-1} \rangle^{-1} = 1.45$; the alternative value is $C_{\text{avg}} = \langle C_i \rangle = 1.73$.

When modeling real early-type galaxies as in the main part of this paper, we do not use any of these choices for C . This is because our galaxy sample is not randomly selected in sub-type (E or S0), and these sub-types are known to have a systematic connection with inclination. Lenticular galaxies are difficult to identify when close to face-on, so the samples of lenticular and elliptical galaxies will be biased to high and low inclinations, respectively. To correct for this bias, we adopt a simplified picture where there is only *one* species of early-galaxy, which gets classified as E or S0 depending on whether its inclination is below or above a boundary of $i = \pi/3$ (cf. Jørgensen & Franx 1994). Therefore we apply median deprojection factors of $C_{\text{med}} = 1.21$ ($i = 1.32$) for the lenticulars, and $C_{\text{med}} = 1.65$ ($i = 0.72$) for the ellipticals.

When applying this approach for j_t estimation to real data, one has to make allowances for the limited radial extent of the available $v_{\text{rot,p}}(R)$ profiles. One can still use Equation (A7) and extrapolate beyond the data, while taking care to quantify the uncertainties that this entails. We will provide examples of this procedure in the main text. However, a much easier approach is also possible—sacrificing some accuracy for the sake of speed and simplicity—which we outline below and test with detailed calculations.

A.4. Simple angular momentum estimator

The general idea for simple j_p estimation is that every galaxy can be characterized by a single observed rotation velocity v_s , which if substituted as a constant value in Equation (A7) would give the same answer as using the full $v_{\text{rot,p}}(x)$ profile. The rotation-velocity and surface brightness components in Equation (A7) are then separable, and we can reduce the calculation to a product of a numerical coefficient, a velocity scale, and a scale-length

$$\tilde{j}_p = k_n v_s R_e, \quad (\text{A30})$$

which is analogous to Equation (A22). Here \tilde{j}_p is a general approximation of j_p , and the coefficient k_n is a spatial weighting factor calculated using Equation (A7) with $v_{\text{rot,p}}(x)$ set to unity (i.e., corresponding to a weighting derived from the stellar density profile combined with a radius x lever-arm). k_n is a function of n , with the following handy approximation, accurate to better than 4%:

$$k_n \simeq 1.15 + 0.029 n + 0.062 n^2. \quad (\text{A31})$$

Thus, $k_1 = 1.19$ and $k_4 = 2.29$, as in Equations (A21) and (A28).

The crux of this approach is estimating v_s from observations without having to evaluate the full integral in Equation (A7), nor requiring that the rotation-velocity profile be known to the outermost radii. The trick comes from realizing that every galaxy has at least one radius x_s where the local projected rotation velocity is equal to v_s . This

²⁶ That is, given an observed rotation velocity v_s , we would have $j_t = 2.70 v_s R_e$, which may be contrasted with the expression

$j_t = 1.03 v_s R_e$ from Scorza & Bender (1995), who took dilution and non-cylindrical rotation into account but neglected all of the angular momentum outside of $5 R_e$.

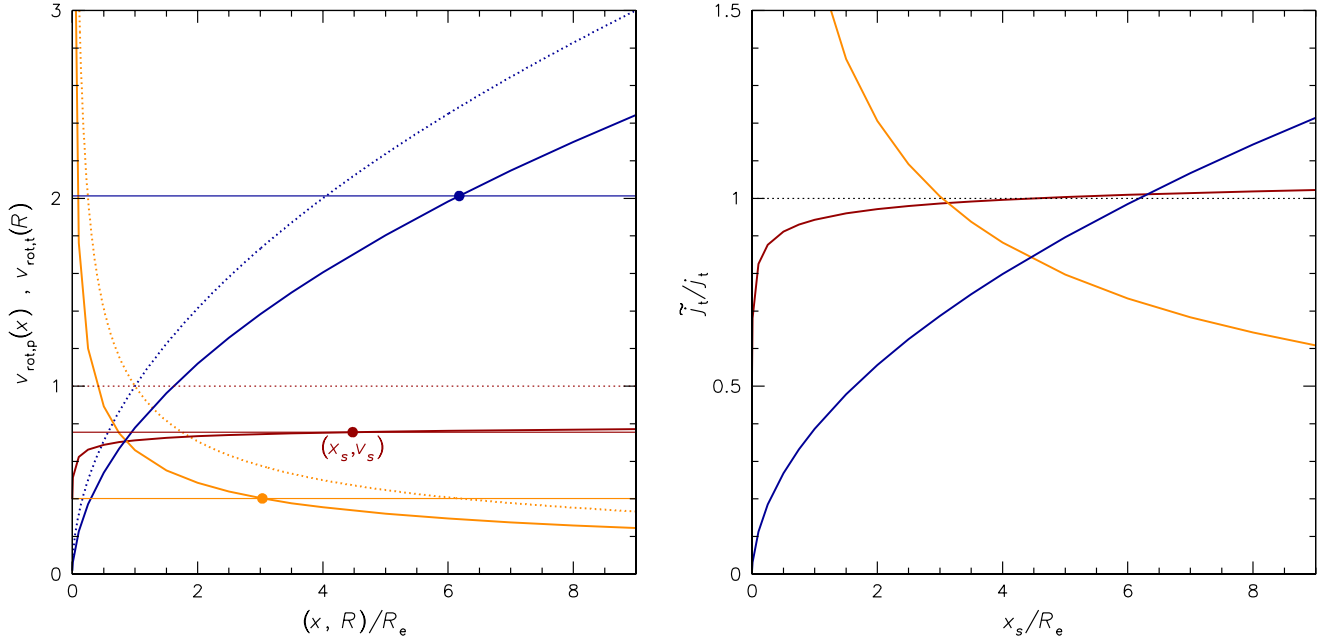


FIG. 25.— Relations between true and observed properties of idealized spherical galaxies with de Vaucouleurs profiles ($n = 4$) and inclination $i = \pi/3$. Different colors indicate models with distinct rotation-velocity profiles (red: constant; blue: $v_{\text{rot,t}}(R) \propto R^{1/2}$, orange: $v_{\text{rot,t}}(R) \propto R^{-1/2}$). *Left*: True (dotted curves) and projected (solid curves) rotation velocities vs. galactocentric distance, in units of the effective radius. The horizontal dashed lines show the characteristic global rotation velocities v_s , with the large dots marking the radii x_s where $v_s = v_{\text{rot,p}}(x_s)$. *Right*: Ratio of estimated to true specific angular momentum, vs. the chosen measurement location x_s (see text for details).

radius varies from one galaxy to another, but we might expect the variation to be modest if real galaxies have rotation-velocity profiles that are not too dissimilar. The implication then is that we can simply measure the rotation velocity at the same radius x_s/R_e for all galaxies and adopt $v_s = v_{\text{rot,p}}(x_s)$ for use in Equation (A30).

There are two potentially different goals here: one is to pick the radius x_s that yields *on average* the correct answer for j_p for a variety of galaxies; the other is to pick a radius where the *scatter* in the j_p approximation is minimized. The anticipated origin of this scatter is the variety of radial behaviors of early-type galaxy rotation-velocity profiles, e.g., rising or falling from central to outer regions, such that the radius x_s which applies to one galaxy might not work well for another. It is the issue of scatter that is most important, since a systematic offset in \tilde{j}_p can be calibrated out and subsumed in the value of k_n .

We test this heuristic concept via some simple model galaxies below and via some real observations in the main text. We find that x_s values anywhere in the range of $\sim (2-5) R_e$ appear to work reasonably well, and in order to maximize the number of suitable galaxies, we adopt $x_s \simeq 2 R_e$.

To arrive at this point, we first experiment with galaxy models having simple power-law rotation-velocity profiles $v_{\text{rot,t}}(R)$ that range between $\propto R^{-1/2}$ and $\propto R^{+1/2}$. For each Sérsic index n , and rotation-velocity profile, we compute \tilde{j}_p via Equation (A7), next determine the equivalent v_s value, and then find the radial location x_s where the local projected rotation velocity is equal to v_s . Finally, we examine the ratio \tilde{j}_t/j_t , [where j_t is known exactly from Equation (A4)] for a range of x_s , which allows us to diagnose the best values of x_s to use in general. We make \tilde{j}_t and j_t comparisons here, rather than \tilde{j}_p and j_p , in order to incorporate the impact of neglecting the mild dependence of C_i on rotation-velocity profile [Equation (A19)].

This procedure is illustrated for one case ($n = 4$, $i = \pi/3$) in Figure 25. The left-hand panel shows the intrinsic and projected rotation-velocity profiles for three different models. The horizontal lines show the values of v_s which would yield the correct $\tilde{j}_p = j_p$ when substituting $k_4 = 2.29$ in Equation (A30). The intercept of the value with the corresponding $v_{\text{rot,p}}(x)$ profile gives the appropriate radius x_s . In the right-hand panel, the accuracy of \tilde{j}_t is plotted versus the chosen x_s for each model. For the constant-rotation-velocity model, $\tilde{j}_t \simeq j_t$ for a wide range of x_s , i.e., the results are insensitive to x_s . For the other rotation-velocity models, the choice of x_s is more critical and ranges from $\simeq 3R_e$ to $\simeq 6R_e$. A compromise radius that works reasonably well is $x_s \simeq 4.5 R_e$, which provides accurate \tilde{j}_t estimates at the 15% level or better for all three models.

Exploring other values of n and i , we find that inclination is not important, and that some aspects of the $n = 4$ example are generally true for other n . For each n , the radius x_s that minimizes the errors in \tilde{j}_t among the different rotation-velocity profiles is close to the exact value of x_s for the constant rotation velocity case. This “sweet spot”

also depends systematically on the density profile: for $n = 2, 4$, and 6 , it occurs at $x_s \sim 2 R_e, 4.5 R_e$, and $10 R_e$ ²⁷.

This x_s trend demonstrates that the extended envelopes of higher- n galaxies contribute relatively more to j_t , and require correspondingly extended kinematics observations. Given that the R_e values for high- n galaxies are already large, the observations to $\sim 10 R_e$ become extremely challenging, and we will in general omit such galaxies from our current analysis. Observations at $x_s \sim 4.5 R_e$ as needed for $n \sim 4$ galaxies are also relatively rare, but fortunately the systematic bias in \tilde{j}_t when using smaller x_s is small, and the scatter is still only $\sim \pm 0.1$ dex when $x_s \sim 2.5 R_e$.

The foregoing tests involve model galaxies whose intrinsic properties we fully understand, but we also need to carry out checks with real galaxies. In the main text (Section 3), we present more detailed models of a half-dozen real galaxies, using Equation (A7) along with the full observed rotation-velocity profiles to estimate j_p . There we show that the constant v_s approach works fairly well for a broad range of radii, and we adopt $x_s \simeq 2 R_e$; at this radius, the systematic offset in \tilde{j}_p appears to be small, and the galaxy-to-galaxy scatter is $\sim \pm 0.1$ dex.²⁸

We have thus arrived at our adopted procedure for simplified j_p estimation using Equation (A30). This \tilde{j}_p is then multiplied by the deprojection factor C_i to yield an estimate of the intrinsic \tilde{j}_t . Of special interest is the de Vaucouleurs profile ($n = 4$), with the approximate result for a median inclination

$$\tilde{j}_t = 3.03 v_s R_e, \quad (\text{A32})$$

which is related to Equation (A28) by a factor of C_{med} in order to account for the rotation-velocity dilution ($v_s < v_t$; note that as discussed in the previous subsection, in practice, C_{med} may need to be corrected for additional inclination-selection effects). This can be compared to the expression used by F83:

$$j_t = 2.5 v_m R_e, \quad (\text{A33})$$

where v_m was the maximum value of the projected rotation velocity within the (central) observed region. This formula is now superseded by the more accurate expressions above.

A.5. Flattening corrections

Real galaxies of course are not spheres. We could in principle set up a standard axisymmetric density model by making an ellipsoidal substitution for r as needed with $\rho(r)$:

$$m^2 = R^2 + \frac{z^2}{q^2} = x'^2 + z'^2 \sin^2 i + \frac{z'^2 \cos^2 i}{q^2}, \quad (\text{A34})$$

where q is the intrinsic axis ratio, and again we are measuring rotation velocity only along the projected semi-major axis ($y' = 0$). Substituting this expression into Equation (A17) along with additional modifications of Equation (A19), we find from some test calculations that even strong flattening makes only a very small difference to $v_{\text{rot,p}}$ and to C_i , which typically increase and decrease (respectively) by ~ 5 – 10% relative to the spherical case for $q = 0.3$. Given the mildness of these effects, and the unknown systematics of the cylindrical-rotation assumption, we will not attempt to make any correction based on the flattening. The extrapolation of the kinematic data to larger radii is in any case probably the dominant uncertainty for our final results.

The other potential concern here is the effective radius. We have already mentioned for disk galaxies that the value of R_d used in Equation (A21) is not the observed but instead the deprojected value. Similarly, for flattened spheroidal galaxies, we should not use in Equation (A30) the circularized value R_e normally tabulated in catalogs, but the equivalent distance along the semi-major axis, $a_e \equiv R_e/\sqrt{q'}$, where q' is the observed axis ratio (in the rest of the paper we simplify this to q). This is because even though we may not know the inclination of a galaxy, we do know (for an axisymmetric case) that if it were face-on, the true R_e needed to calculate j_t would be roughly the same as a_e . Since early-type galaxies can be as flattened as $q' \sim 0.3$, this is a significant correction.

A caveat here is that the observed flattening is correlated with the inclination: e.g., a galaxy with $q' = 0.3$ is probably nearly edge-on, and adopting the median inclination for random orientations would then cause us to overestimate its j_t . Also, the intrinsic R_e value for a spheroidal galaxy is slightly smaller than $a_e/\sqrt{q'}$ (see also Williams et al. 2009). However, these two effects are much weaker in general than neglecting the q' correction entirely. Therefore in the main text we carry out all of the calculations using densities and kinematics along the semi-major axis: e.g., $\Sigma(x)$ and a_e rather than $\Sigma(R)$ and R_e .

²⁷ These locations are very similar to the corresponding radius of gyration (where a point mass would have the same moment of inertia as the full mass profile; see Coccato et al. 2009).

²⁸ For the real galaxies, we do not attempt a full \tilde{j}_t and j_t

comparison because we do not know the detailed intrinsic rotation-velocity profiles needed to calculate C_i exactly.

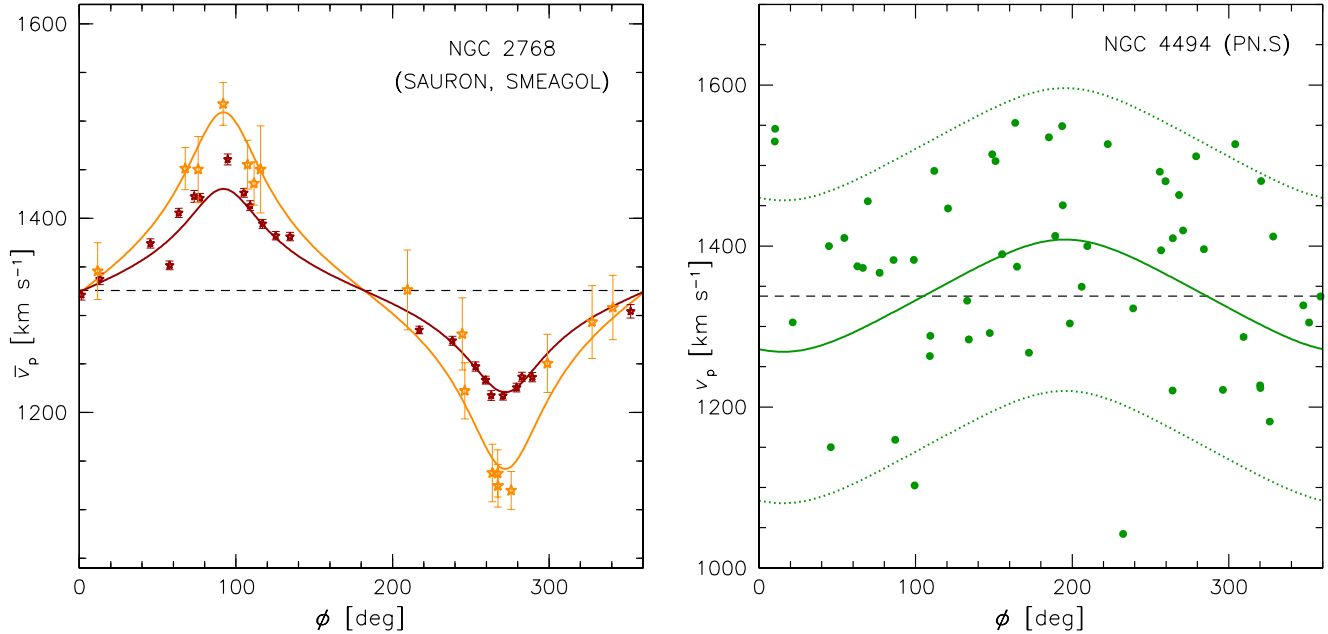


FIG. 26.— Examples of kinematic model fits to two-dimensional velocity data in early-type galaxies. On the *left* are subsets of stellar kinematics measurements in the galaxy NGC 2768 from SAURON using integral field spectroscopy (Emsellem et al. 2004) and from SMEAGOL using the SKiMS technique (Proctor et al. 2009). These data sets are marked with small and large points, respectively, and are taken from radii $x \sim 35''$ ($\sim 0.3 a_e$) and $x \sim 125''$ ($\sim 1.3 a_e$), respectively. The horizontal dashed line marks the systemic velocity (the SAURON data have been offset to match up with SMEAGOL), and the curves show flattened sinusoidal model fits to the data [see Equation (B1)]. The increase of rotation velocity with radius is apparent here by eye. The *right* panel shows PN data for NGC 4494 (Napolitano et al. 2009) at a radius of $x \sim 60''$ ($\sim 1.3 a_e$). The solid curve shows the mean velocity model fit, while dotted curves show the intrinsic dispersion σ of the model, marking $\pm 2\sigma$ boundaries. For clarity, the measurement uncertainties of the individual data points (typically 20 km s^{-1}) are not shown.

APPENDIX B: DETAILED OBSERVATIONAL RESULTS FOR INDIVIDUAL GALAXIES

Here we present in some detail the data and methods used to derive angular momentum profiles for individual early-type galaxies. Our general approach is to map all of the data to an equivalent semi-major axis rotation-velocity profile, as though making a standard long-slit observation. In some cases, the data are already available in this format while in others that involve discrete and semi-discrete data at various position angles, we must fit a two-dimensional kinematic model before mapping onto the semi-major axis.

Our modeling method was recently developed for use with sparsely sampled two-dimensional data (Proctor et al. 2009; Arnold et al. 2011; Foster et al. 2011; Strader et al. 2011; Pota et al. 2012). It is based on flattened sinusoidal curves of mean line-of-sight velocity versus azimuth ϕ :

$$\bar{v}_p(\phi, x) = \pm v_{\text{rot,p}}(x) \left[1 + \frac{\tan^2(\phi - \phi_0)}{q^2} \right]^{-1/2}, \quad (\text{B1})$$

where $v_{\text{rot,p}}(x)$ is the rotation velocity versus the semi-major axis distance x , and \bar{v}_p is evaluated along an ellipse with axis ratio q . The on-sky coordinates are the same as introduced in Appendix A, but without primes ($'$) for the sake of simplicity; the position angle of maximum receding rotation velocity is at $\phi = \phi_0$. This model is exactly equivalent both to a $\cos \phi$ rotation velocity multiplied by the equation for an ellipse in polar coordinates, and to the classic tilted-ring approach used for gas disks (e.g., Guhathakurta et al. 1988; Begeman 1989). Therefore it is a natural observational model to use in conjunction with our j_t modeling scheme, which assumes a cylindrical rotation field in the reference frame of the galaxy (Appendix A). There is also a connection here to the “kinematic” methods of modeling data from integral-field spectrographs, where the two-dimensional kinematics are expanded in a Fourier series (Krajnović et al. 2006; Krajnović et al. 2008). Our model is equivalent to the first-order term of this expansion.

In principle, the parameters q and ϕ_0 should be determined by fitting to the kinematic data, but in practice, the azimuthal sampling is often too sparse for such constraints. For the sake of a uniform treatment of the data, we adopt the *photometric* values for q and ϕ_0 in every case; these are generally held constant at a global value, e.g., neglecting kinematic twists with radius. The errors introduced through these simplifications are generally much smaller than the uncertainties in extrapolating $v_{\text{rot,p}}(x)$ outwards to radii beyond the data.

Figure 26 illustrates the kinematic fitting procedure for several types of data. One type that may be unfamiliar is the “stellar kinematics with multiple slits” (SKiMS) technique from the SMEAGOL project (Proctor et al. 2009; Arnold et al. 2011; Foster et al. 2011; Forbes et al. 2012), which uses a wide-field multi-slit spectrograph to provide sparse sampling of a two-dimensional field as needed for reconstructing the basic kinematical structure. Equation (B1)

is fitted to the data (left-hand panel), while occasionally disregarding outlying data points so as not to skew the results. The uncertainties on the rotation velocities are estimated via Monte Carlo simulations of mock data sets.

This procedure is modified slightly for discrete velocity data such as from PNe and GCs, which are sparsely sampled not only in position but also in velocity. Here, each data point is not a measure of the local mean velocity, but is a random *discrete* velocity drawn from an underlying distribution. The kinematic modeling of rotation therefore involves simultaneous fitting for the velocity *dispersion* using a maximum likelihood method (which represents a refinement, along with the rotation-field flattening, of the commonly-used least-squares method; e.g., Cohen & Ryzhov 1997). Note also that when using data from the PN.Spectrograph (Napolitano et al. 2009, 2011; Coccato et al. 2009), we ignore the results inside $\sim R_e$ since there are known systematic biases that can occur in the central regions, where PN detection may be velocity-dependent.

To combine different data sets on the same galaxy, we could in principle fit them all simultaneously to a single kinematic model. However, for the sake of simplicity and transparency, we create separate one-dimensional rotation-velocity profiles from each data set separately, and then combine these into a single profile. For this final combination, we set up a new grid of data bins that are smoothly distributed in radius, and in each bin average the weighted contribution of each data point according to its uncertainties and its fractional overlap with that bin. The price of generating these well-behaved profiles is that the values in each bin are not fully independent of those in adjacent bins.

A significant complication in our analysis comes in extrapolating the rotation-velocity profile beyond the outermost measured data points. In a spiral galaxy, this can be done assuming a profile that becomes asymptotically constant, but we cannot assume any such model for an elliptical or lenticular. Instead, we fit a power-law model of rotation velocity with radius to the final few data points: $v_{\text{rot,p}}(x) \propto x^\gamma$.

The optimum range of points to use in this fit is not straightforward to determine: use too few, and the extrapolation becomes merely an amplification of noise in the outermost measurements; use too many, and the inner measurements with their small uncertainties dominate the fit, which may not even agree with the outer measurements. Therefore some degree of subjectivity is involved, where the radial region used in the fit is determined by the widest range that still appears consistent with a smooth power-law trend, which typically occurs outside $\sim 2.5 R_e$ for our sample. The permitted range of power-law exponents γ is then determined by a $\Delta\chi^2 = 1$ criterion. In some cases the formal range of γ is large and we adopt a plausibility prior that the rotation velocity increases no more rapidly than linearly with radius (i.e. $\gamma < 1$). Note that although there may be lingering concerns about the robustness of these extrapolation procedures, half of the galaxies in our detailed sample have data out to $\sim 8\text{--}10 R_e$, in which case the extrapolation is relatively unimportant for the j_* calculation.

The kinematic data for the eight early-type galaxies that we model in detail are described in the remainder of this section, followed by plots of the kinematic profiles in the left panels of Figures 28–31. Here the velocity dispersion profiles are included for comparison with the rotation-velocity profiles, but are not otherwise used in this paper. For completeness, we also include the two spiral galaxies that we model in detail as described in Section 3.1 (Figure 27).

We convert the rotation velocity data into profiles of projected specific angular momentum j_p using the methods of Section 2 and Appendix A. These are also presented in Figures 27–31 (right-hand panels). We summarize the relevant observational and modeling parameters for these galaxies in Table B3. Note that in many cases from this sample, new GC kinematics data were recently obtained by Pota et al. (2012), but are not incorporated here.

NGC 821—Isolated, disk elliptical. Stellar kinematics data to $\sim 4 a_e$ are combined in a single kinematic model, drawing on a number of sources including SAURON, SMEAGOL, HET, GMOS and MDM (Pinkney et al. 2003; Proctor et al. 2005; Weijmans et al. 2009; Proctor et al. 2009; Forestell & Gebhardt 2010). PN data are taken from Coccato et al. (2009), who used non-parametric kinematic mapping techniques and found a strong kinematic misalignment relative to the stellar kinematics. We find the same result, such that the PNe between ~ 1 and $2 a_e$ are strongly *counter*-rotating with respect to the stars. At larger radii, the PNe and stars agree, and we suspect some kind of contamination in the intermediate-radius PN sample (cf. Sambhus et al. 2006). However, the PN rotation velocity along the major axis is still marginally consistent (given the errors) with the stellar rotation velocity outside $1 a_e$, so we include these PN data anyway since the overall results are dominated by the stellar data in these regions. The final composite profile has a remarkably low outer rotation velocity, as emphasized by Proctor et al. (2009).

NGC 1400—Apparently round early-type galaxy, probably a member of the NGC 1407 group. It may be a lenticular seen near face-on. The data include major-axis long-slit spectra out to $\sim 1 a_e$, and SKiMS covering $\sim 1\text{--}3 a_e$ from SMEAGOL (Proctor et al. 2009). As Proctor et al. discussed, there is an unexplained velocity dispersion discrepancy between these two stellar-light data sets, but the rotation-velocity profiles are consistent.

NGC 1407—Bright, round elliptical at the center of the Eridanus A group. Stellar kinematics data out to $\sim 3 a_e$ come from major-axis long-slit spectra and from SMEAGOL (Proctor et al. 2009). Kinematics data for 55 metal-rich GCs extend to $\sim 12 a_e$ (Romanowsky et al. 2009), where we have removed objects brighter than $i = 21.3$ owing to their peculiar kinematics, which may imply contamination by ultra compact dwarfs (cf. Brodie et al. 2011). There is also a mismatch between the stellar and GC velocity dispersions around $\sim 1 a_e$ that could be caused by additional contamination from substructure or from the metal-poor GC subpopulation, but the overall rotation-velocity profile is not affected. We adopt $q = 1$ and a fixed $\phi_0 = 250^\circ$ for all of the kinematic modeling.

NGC 2768—Flattened E/S0 in the field; we have overruled the RC3 classification of E6 in favor of other classifications from the literature, including the RSA, as S0. Stellar kinematics data out to $\sim 2 a_e$ are drawn from SAURON and

SMEAGOL (see left-hand panel of Figure 26). From our detailed early-type galaxy sample, this is the case with the most strongly increasing $v_{\text{rot,p}}(x)$ profile. However, the kinematic data are still somewhat limited, and there are preliminary indications from more radially extended data for a decreasing rotation-velocity profile (A. Romanowsky et al., in preparation). Note that the extrapolation of the data outwards can reach an unphysical rotation velocity, exceeding a plausible circular velocity of $\sim 300 \text{ km s}^{-1}$, but restricting the maximum rotation velocity does not substantially alter the permitted range of j_{p} .

NGC 3377—Disky, low-luminosity elliptical in a loose group (Leo I). The kinematic data are from SAURON inside $0.7 a_e$, deep long-slit VLT/FORS2 major axis spectra to $3.4 a_e$ (Coccatto et al. 2009), and 112 PN velocities between 1 and $12 a_e$ (Coccatto et al. 2009). In comparing data-sets in their overlap regions (including other long-slit kinematics from the literature: Bender et al. 1994; Kormendy et al. 1998; Halliday et al. 2001; Prugniel & Simien 2002) we discovered some fairly large discrepancies, particularly in the velocity dispersion. Assuming that the higher spectral resolution of the FORS2 results makes them more reliable, we therefore subtract 59 km s^{-1} in quadrature from the SAURON dispersions, and multiply the SAURON rotation velocities by a factor of 1.13. The impact of this issue on rotation velocity and j_{p} is not large, but we note that characterizations of low-mass galaxies in general using quantities such as $v_{\text{rot}}/\sigma_{\text{p}}$ should be viewed with caution since they could be strongly affected by systematic problems, as in NGC 3377. There is some indication of a $\sim 20^\circ$ kinematic twist in the outer parts of this galaxy, where the true rotation velocity could be $\sim 60 \text{ km s}^{-1}$ rather than $\sim 20 \text{ km s}^{-1}$.

NGC 4374 (M84)—Bright, slow-rotator elliptical, apparently in a subgroup along with M86 falling in to the Virgo cluster. The kinematic data include SAURON inside $0.2 a_e$, deep long-slit VLT/FORS2 major and minor axis spectra to $0.8 a_e$ (Coccatto et al. 2009), and 450 PN velocities between 0.1 and $2.3 a_e$ (Napolitano et al. 2011). As with NGC 3377 (above), we found discrepancies between the SAURON and FORS2 data, and subtracted 85 km s^{-1} in quadrature from the SAURON velocity dispersions. Both the FORS2 and PN data show a sudden kinematic twist from near major axis alignment inside $65''$ to near minor axis alignment at larger radii. (We recovered this information from the FORS2 data by fitting a two-dimensional kinematic model to the major and minor axis data.) This minor-axis rotation was also apparent in the PN analysis of Coccatto et al. (2009), although the isophotes also twist so that by $\sim 200''$, the rotation is actually along the major axis. There may be further kinematic twisting outside $\sim 250''$ such that the rotation is again along the minor axis, with a velocity of $\sim 40 \text{ km s}^{-1}$. Because of the strong twisting in this triaxial galaxy, and the fact that $q = 0.9\text{--}1.0$ in the outer regions, we adopt the circularized $R_e = 176''$ value for a_e . There is one other complication with a high- n galaxy like NGC 4374, as discussed in Section 3.2: the cumulative j_{p} converges slowly with radius, and so we choose the virial radius $r_{\text{vir}} \sim 6095''$ of the galaxy as the boundary for defining “total” enclosed j_{p} .

NGC 4494—Round elliptical in the Coma I cloud. The kinematic data include stellar long-slit spectroscopy to $\sim 2 a_e$ (Napolitano et al. 2009), stellar kinematics with multiple slits (SKiMS) to $\sim 4 a_e$ (Proctor et al. 2009), and PN velocities to $\sim 9 a_e$ (Napolitano et al. 2009; Coccatto et al. 2009). The newest SKiMS dataset from Foster et al. (2011) was not used, but would yield essentially the same rotation-velocity profile; note that this paper provided an inclination estimate of $i \sim \pi/4$. An example of the PN data is shown in the right-hand panel of Figure 26.

NGC 5128—Peculiar early-type galaxy at only 4 Mpc distance. The kinematic data include pioneering two-dimensional spectroscopy out to $\sim 0.5 a_e$ from Wilkinson et al. (1986) and 780 PN velocities to $\sim 15 a_e$ from Peng et al. (2004). Analysis of the PN data does not show any strong kinematic twists with radius, so for simplicity we use a fixed $\phi_0 = 259^\circ$ for the entire galaxy. Also, because of the lack of detailed photometry for the galaxy, we set $q = 1$.

TABLE 3
ANGULAR MOMENTA OF GALAXIES MODELED IN DETAIL.

NGC	Type	D (Mpc)	n	a_e (kpc)	a_{\max} (a_e)	q	v_s (km s^{-1})	j_p ($\text{km s}^{-1} \text{ kpc}$)	$\log\left(\frac{M_*}{M_\odot}\right)$	Tracers	Ref.
3054	Sb	34.4	1	7.8	2.3	0.62	177	1670^{+110}_{-100}	11.12	H α	P+04a
3200	Sc	52.2	1	15.3	1.8	0.28	261	4750^{+330}_{-280}	11.37	H α	P+04a
821	E6	23.4	3.4	4.5	10.7	0.60	23	210^{+160}_{-100}	11.02	IFU, LS, MS, PN	E+04, C+09, P+09, W+09a, FG10
1400	S0	25.7	1.9	2.7	4.4	0.89	48	190^{+40}_{-20}	11.05	LS, MS	P+09
1407	E0	28.1	4.3	7.8	11.7	1.0	39	750^{+760}_{-560}	11.66	LS, MS, GC	P+09, R+09
2768	S0	21.8	2.6	10.7	2.3	0.40	169	3060^{+410}_{-640}	11.33	IFU, MS	E+04, P+09
3377	E5	10.9	2.0	2.5	10.5	0.67	56	200 ± 30	10.50	IFU, LS, PN	E+04, C+09
4374	E1	18.5	8.3	15.8	2.3	1.0	32	1610^{+3860}_{-1000}	11.68	IFU, LS, PN	E+04, C+09
4494	E1	16.6	3.2	4.5	8.5	0.84	58	430^{+190}_{-110}	11.08	LS, MS, PN	N+09, C+09, P+09
5128	S0	4.1	4	6.0	15.3	1.0	61	840^{+140}_{-120}	11.28	MS, PN	W+86, P+04b

NOTE. — Morphological Types are generally taken from the RC3 catalog (de Vaucouleurs et al. 1991). v_s and j_p are calculated from the full, detailed treatment of Equations (3) and (4). The distances D are taken from surface brightness fluctuation analyses (Tonry et al. 2001; Blakeslee et al. 2009) where available, and otherwise from redshifts. The Sérsic parameters n and a_e are taken from various literature sources. The tracers include H α gas-emission rotation-velocity curves; long-slit stellar kinematics (LS); multi-slit stellar kinematics (MS); integral-field stellar kinematics (IFU); planetary nebulae (PN); and metal-rich globular clusters (GC). The references are Wilkinson et al. 1986 (W+86); Emsellem et al. 2004 (E+04); Pizzella et al. 2004 (P+04a); Peng et al. 2004 (P+04b); Coccato et al. 2009 (C+09); Napolitano et al. 2009 (N+09); Proctor et al. 2009 (P+09); Romanowsky et al. 2009 (R+09); Weijmans et al. 2009 (W+09a); Forestell & Gebhardt 2010 (FG10).

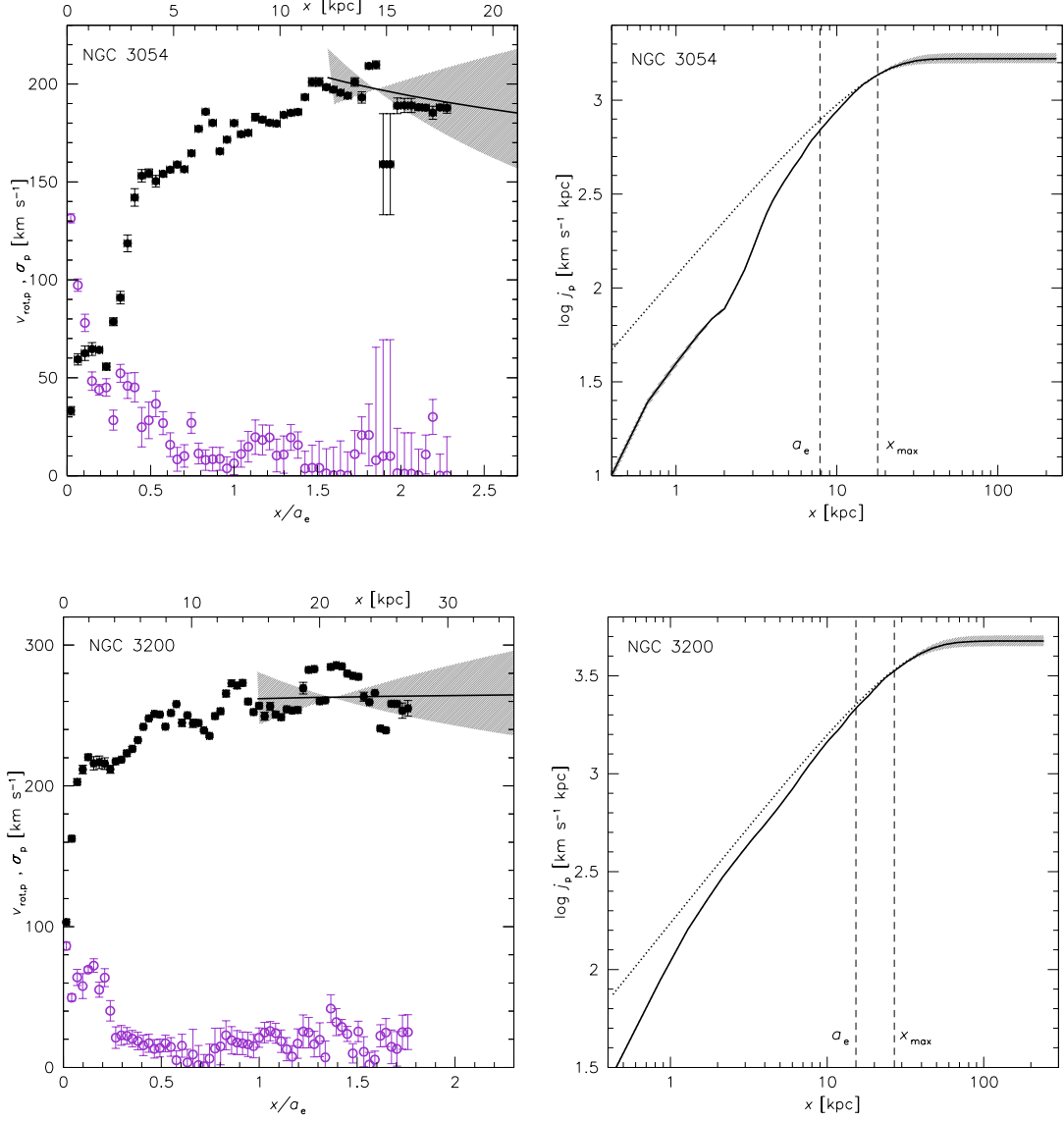


FIG. 27.— Kinematic results for the spiral galaxies NGC 3054 (*top panels*) and NGC 3200 (*bottom panels*). The *left-hand panels* show data for the profiles of projected rotation velocity (black filled circles) and velocity dispersion (purple open circles) vs. semi-major axis radius. The black curve with shaded region shows the outer power-law extrapolation of the rotation velocity and its estimated uncertainty. The *right-hand panels* show the data converted into a profile of cumulative projected specific angular momentum vs. radius (solid curve), with the shaded regions showing the uncertainties (barely visible for this galaxy). The dotted curve shows the expected distribution of $j_p(< x)$ for a constant rotation-velocity profile. Vertical dashed lines show the effective radius of the galaxy and the maximum extent probed by the kinematic data.

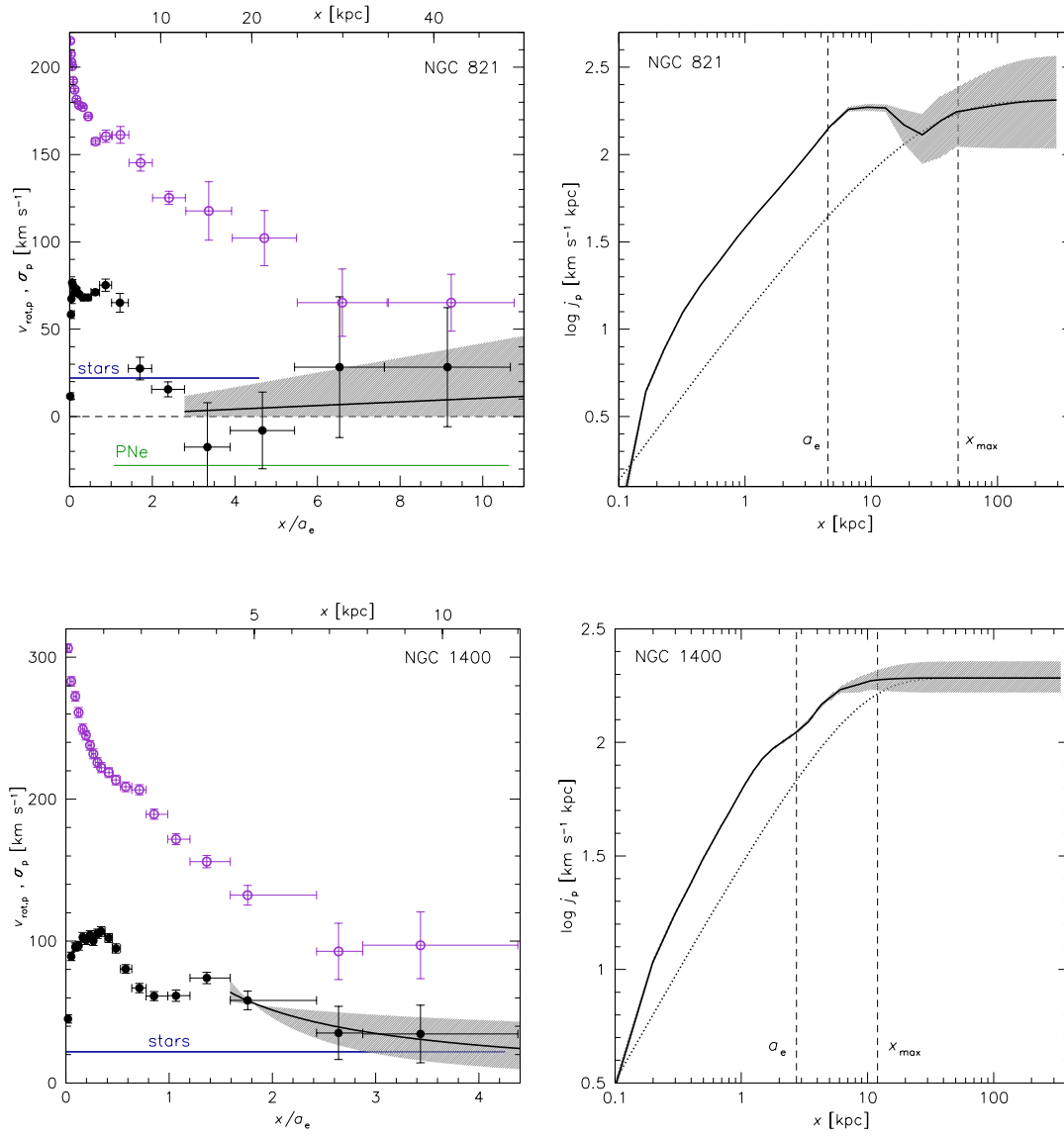


FIG. 28.— Kinematic results for the early-type galaxies NGC 821 (*top panels*) and NGC 1400 (*bottom panels*). See Figure 27 for explanations. In addition, horizontal lines in the left-hand panels indicate the radial ranges spanned by the different data sets. Note also the dashed line at zero rotation velocity in the case of NGC 821.

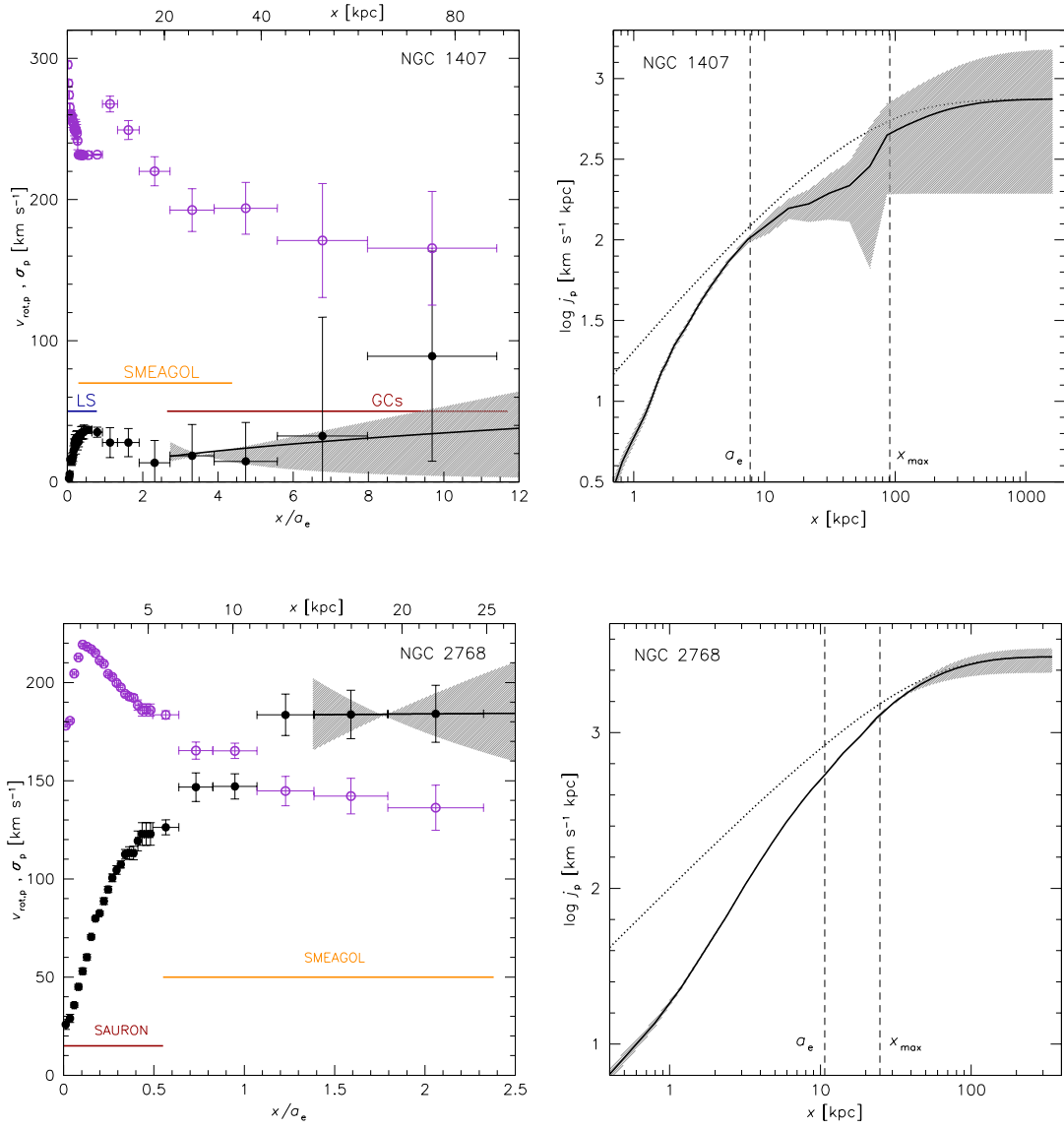


FIG. 29.— Kinematic results for the early-type galaxies NGC 1407 (*top panels*) and NGC 2768 (*bottom panels*). See Figures 27 and 28 for explanations.

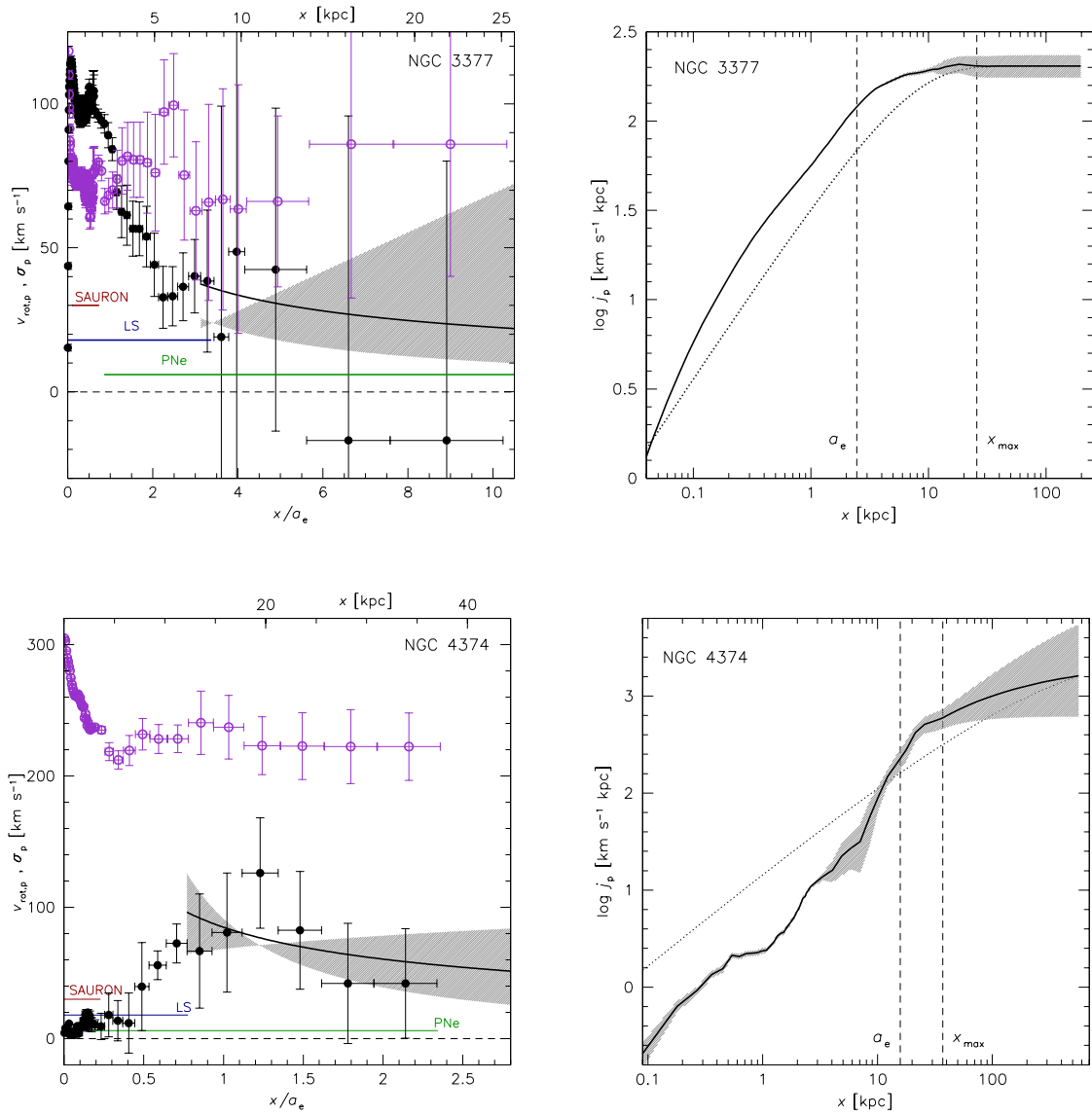


FIG. 30.— Kinematic results for the early-type galaxies NGC 3377 (*top panels*) and NGC 4374 (M84; *bottom panels*). See Figures 27 and 28 for explanations.

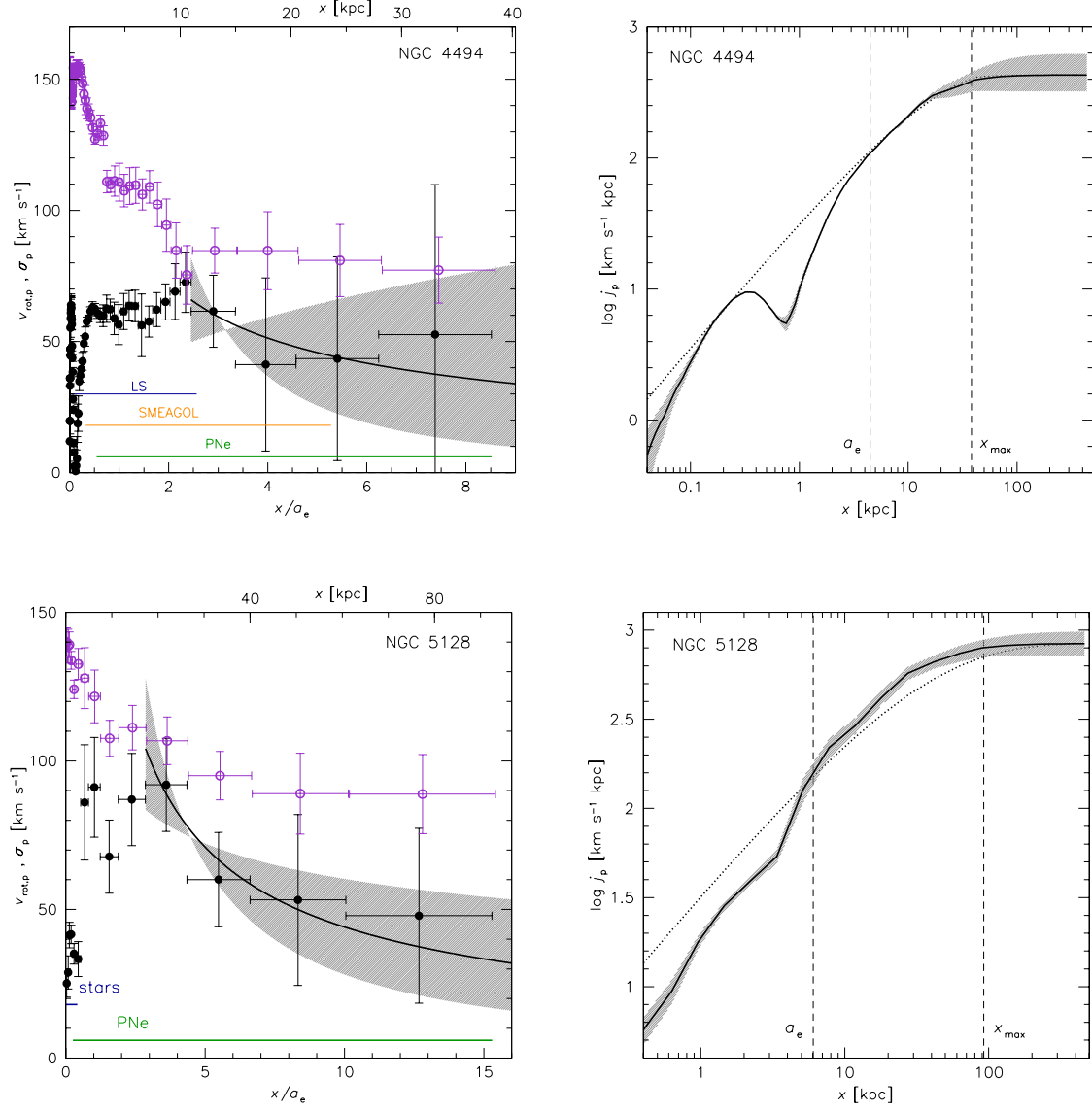


FIG. 31.— Kinematic results for the early-type galaxies NGC 4494 (*top panels*) and NGC 5128 (*bottom panels*). See Figures 27 and 28 for explanations.

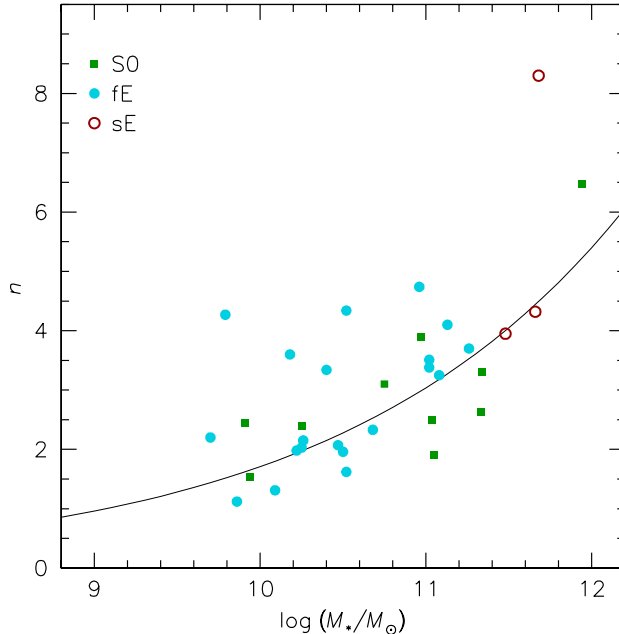


FIG. 32.— Relation between Sérsic index n and stellar mass M_* for early-type galaxies. Points show results from the literature for individual galaxies in our sample. Symbol and colors indicate different galaxy types as in the legend; fE and sE mean ‘fast rotator’ and ‘slow rotator’ ellipticals based on their central properties (see text for details). The black curve shows our adopted mean relation, Equation (C1).

APPENDIX C: SUPPLEMENTAL OBSERVATIONAL INFORMATION FOR FULL SAMPLE

Here we describe some details of the full sample of observational data, with results reported in Tables C4 and C5. The methods for the spiral galaxies are described in Section 4.1 and do not require further elaboration. For the early-types, in addition to the generalities in Section 4.2, here we discuss details including estimates of the Sérsic index n , an evaluation of bias in our galaxy sample selection, and some nuances of the size–mass relation.

The issue with n is that, as discussed in the main text, its value is a significant factor in accurate j calculation, but is not available for some of the galaxies in our sample. Instead, we use a statistical estimate based on trends among other galaxies. Figure 32 shows the n – M_* correlation for the early-type galaxies in our sample that *do* have Sérsic fits available. There is a correlation between M_* and n that echos other trends in the literature, and in particular matches the power-law slope of ~ 0.3 found by Graham & Guzmán (2003). The mean relation that we adopt is

$$n = 5.4 \times 10^{-3} \times (M_*/M_\odot)^{0.25}. \quad (\text{C1})$$

There is a scatter of $\sigma_n \sim 1$ about this relation, which is also similar to variations found in the literature for different Sérsic fits of the same galaxies. This uncertainty in n translates to an uncertainty of $\sim 25\%$ in k_n [see Equation (A31)], and thus ~ 0.1 dex uncertainty in j [Equation (6)].

Next, to investigate whether or not our galaxy sample provides an unbiased, fair representation of the nearby universe, we could check a variety of different galaxy parameters, but given our focus on angular momentum, the most relevant parameter is the readily-measured central stellar rotation velocity.

Our point of comparison is the ATLAS^{3D} survey, which presented photometric and kinematic properties for a complete, volume-limited sample of 260 nearby early-type galaxies, selected only by K -band luminosity (Cappellari et al. 2011a). We use their tabulated central rotation metric, $(v/\sigma)_{e/2}$, which is flux-weighted in two dimensions within an aperture of $R_e/2$ (Emsellem et al. 2011). From the galaxies in common between our samples, we calibrate this metric to our own major-axis kinematic data measured locally at $a_e/2$. We find that the ATLAS^{3D} values of $(v/\sigma)_{e/2}$ should be multiplied by a factor of ~ 2.2 to match our data (which, as expected, is a large difference because of the two-dimensional versus major-axis measurement locations).

We next divide (v/σ) from both data sets by a factor of $[\epsilon/(1-\epsilon)]^{1/2}$ to derive a rotation-dominance parameter $(v/\sigma)^*$. This is analogous to the standard parameter in Equation (8), but is constructed differently for the sake of convenient comparisons between the two data sets, and should not be used to make detailed inferences about the properties of these galaxies.

We plot $(v/\sigma)^*$ versus stellar mass in Figure 33. Our sample follows a similar trend to the unbiased sample, with central rotation becoming systematically less important for the more massive galaxies. Both samples span a similar range in mass.

Another important issue here is the inclusion of different sub-classes of early-type galaxies. Our sample consists of 15 lenticulars and 25 ellipticals, which implies a strong selection bias for ellipticals, since $\sim 75\%$ of nearby early-types

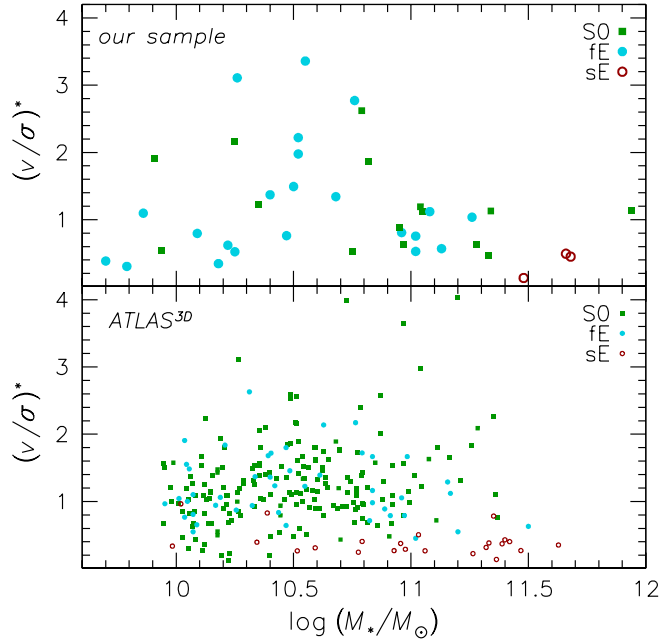


FIG. 33.— Rotation dominance parameter vs. stellar mass for early-type galaxies (see text for details). Our galaxy sample is shown in the top panel, and the ATLAS^{3D} sample in the bottom panel. Symbols show different galaxy types as in the legend. Our sample is biased toward ellipticals and more massive galaxies but otherwise appears to provide a fair representation of the central kinematics of nearby early-types. Note that the fraction of “slow rotators” is highest for the most massive systems.

are S0s (Cappellari et al. 2011a).

In Section 4.3 we compare the size–mass relation of our sample (both the early- and late-types) with the ATLAS^{3D} results. For ATLAS^{3D}, we adopt the power-law relations provided by Cappellari et al. (2011a), after adapting them to the parameters that we plot for our sample. For the spirals, we convert from circularized R_e to a_e by assuming a median inclination of 60° . For the fast-rotator E/S0s, we use a median axis ratio of $q = 0.63$.

Comparison with our sample (in Figure 11) is not straightforward since we have used *disk* sizes rather than total galaxy sizes (bulge+disk) for the spirals. In any case, we find that our results are consistent overall with ATLAS^{3D} but there appears to be a difference for the lower-mass ellipticals; at $\log(M_*/M_\odot) \sim 10\text{--}10.5$, these galaxies are $\sim 30\%$ more compact in our sample than the trend found by ATLAS^{3D}. Examining several galaxies in common between the samples, we find that the discrepancy persists for cases where we have made use of high-quality photometric analyses (Kormendy et al. 2009). Figure 8 of Cappellari et al. (2011a) suggests that for the smaller galaxies, the ATLAS^{3D} sizes, which are partially based on NIR measurements, are overestimated relative to optically-based sizes. This illustrates the type of systematic uncertainties remaining in our analysis, and also of the comfortably low impact that they have on our $j_\star\text{--}M_\star$ analyses (only $\sim \pm 0.05$ dex or $\sim \pm 15\%$ in j_\star).

One additional issue is that our sample of spirals was selected to avoid strong bars which might in principle introduce a bias in j_\star . Inclusion of barred spirals could be an improvement made in a next generation, volume-limited $j_\star\text{--}M_\star$ survey.

TABLE 5
APPROXIMATE ANGULAR MOMENTA OF EARLY-TYPE GALAXIES

Name	Type	T_{Hubble}	D (Mpc)	n	a_e (kpc)	q	v_s (km s $^{-1}$)	\tilde{j}_p (km s $^{-1}$ kpc)	$\log\left(\frac{M_*}{M_\odot}\right)$	Tracers	Ref.
NGC 821	E6	-4.8	23.4	3.4	4.5	0.60	20	180	11.02	LS, MS, PN	C+09, P+09, W+09a, FG10
NGC 1023	S0	-2.7	11.1	3.9	3.2	0.34	175	1270	10.97	LS, PN	C+09
NGC 1316	S0	-1.8	21.0	6.5	13.5	0.68	70	3640	11.94	PN	M+12
NGC 1339	E3	-4.3	19.7	4.3	1.5	0.71	105	400	10.52	LS	G+98
NGC 1344	E4	-4.0	20.9	4.1	5.1	0.58	20	240	11.13	PN	C+09
NGC 1373	E2	-3.9	19.3	4.3	1.0	0.77	10	25	9.79	LS	G+98
NGC 1379	E0	-4.8	19.5	2.3	2.3	0.97	20	70	10.68	LS	G+98
NGC 1380	S0	-2.3	21.2	3.3	5.4	0.51	220	2330	11.34	LS	B+06
NGC 1381	S0	-2.2	21.9	3.1	3.6	0.26	155	1040	10.75	LS	W+09b
NGC 1400	S0	-3.7	25.7	1.9	2.7	0.89	50	3100	11.05	LS, MS	P+09
NGC 1404	E1	-4.8	20.2	3.7	2.6	0.88	115	630	11.26	LS	G+98
NGC 1407	E0	-4.5	28.1	4.3	7.8	1.0	20	680	11.66	MS	P+09
NGC 1419	E0	-4.8	22.9	3.6	1.1	0.99	3	7	10.18	LS	G+98
NGC 1428	S0	-3.0	20.7	1.5	1.4	0.63	65	130	9.97	LS	G+98
NGC 2310	S0	-2.0	14.9	2.1*	3.4	0.19	135	680	10.35	LS	W+09b
NGC 2577	S0	-3.0	31.7	2.7*	2.8	0.62	210	1000	10.79	LS	R+99
NGC 2592	E2	-4.8	31.7	2.6*	2.2	0.83	160	610	10.76	LS	R+99
NGC 2699	E1	-5.0	27.9	2.4*	1.7	0.93	90	240	10.55	LS	R+99
NGC 2768	S0	-4.4	21.8	2.6	10.7	0.40	185	3360	11.33	MS	P+09
NGC 2778	E2	-4.8	22.3	2.2	1.5	0.80	120	270	10.26	LS	R+99, H+01
NGC 3115	S0	-2.9	9.4	2.5	3.7	0.50	190	1150	11.04	LS, MS, GC	A+11
NGC 3156	S0	-2.5	21.8	2.4	2.0	0.58	75	240	10.24	LS	R+99
NGC 3203	S0	-1.2	34.0	2.9	5.7	0.20	165	1700	10.95	LS	W+09b
NGC 3377	E5	-4.8	10.9	2.0	2.5	0.67	45	160	10.50	LS, PN	C+09
NGC 3379	E2	-4.8	10.3	4.7	2.6	0.84	30	210	10.96	SA, LS, PN	D+07, C+09, W+09a
NGC 3605	E3	-4.5	20.1	1.3	1.4	0.66	65	110	10.09	LS	R+99
NGC 4318	E3	-5.0	22.0	1.1	0.8	0.66	85	80	9.86	LS	S+10
NGC 4374	E1	-4.3	18.5	8.3	15.8	1.0	40	2040	11.68	PN	C+09
NGC 4387	E4	-4.9	18.0	2.0	1.3	0.57	50	90	10.25	LS	H+01
NGC 4434	E1	-4.8	22.5	3.3	1.2	0.92	45	110	10.40	LS	S+10
NGC 4464	S0	-2.1	15.8	2.5	0.6	0.70	50	50	9.91	LS	SP97b, S+97, H+01, S+10
NGC 4478	E2	-4.8	17.1	2.1	1.1	0.81	65	110	10.47	LS	D+83, SP97a, H+01
NGC 4486B	E4	-5.0	16.3	2.2	0.2	0.60	35	10	9.70	LS	S+10
NGC 4494	E1	-4.8	16.6	3.2	4.5	0.84	65	570	11.08	LS, MS, PN	N+09, C+09, P+09
NGC 4551	E3	-4.9	16.2	2.0	1.2	0.68	45	80	10.22	LS	S+07, S+10
NGC 4564	E5	-4.8	14.6	1.6	2.2	0.55	120	370	10.52	LS, PN	C+09
NGC 4697	E4	-4.4	11.4	3.5	4.4	0.59	35	320	11.02	PN	C+09
NGC 5128	S0	-2.1	4.1	4.0*	6.0	1.0	80	1110	11.28	PN	P+04b
NGC 5846	E1	-4.7	24.2	4.0	8.4	0.93	25	480	11.48	PN	M+05, C+09
NGC 7617	S0	-1.9	57.1	2.7*	3.3	0.78	80	470	10.82	LS	R+99

NOTE. — Morphological Types are generally taken from the RC3 catalog (de Vaucouleurs et al. 1991). The Hubble stage T_{Hubble} is from HyperLeda (Paturel et al. 2003). The distances D are taken from the surface brightness fluctuation analyses (Tonry et al. 2001; Blakeslee et al. 2009) where available, and otherwise from redshifts. The parameters of the stellar mass profile (n, a_e, q) are taken from various literature sources as described in Section 4.2. Galaxies with a ‘*’ by their Sérsic index n have this value predicted from their stellar masses, rather than being measured directly (see text for details). v_s is estimated from the observations at $x_s = 2a_e$, and \tilde{j}_p is calculated using Equation (6). For the subset of 8 galaxies with detailed j_p calculations listed in Table 3, the \tilde{j}_p values are listed here for reference, but are not used in our main analyses. The observational tracers are: long-slit stellar kinematics (LS); multi-slit stellar kinematics (MS); integral-field stellar kinematics (IFU); planetary nebulae (PN); and metal-rich globular clusters (GC). The references are: Davies et al. 1983 (D+83); Simien & Prugniel 1997a,b (SP97a,b); Sánchez-Blázquez et al. 2007 (S+97); Graham et al. 1998 (G+98); Rix et al. 1999 (R+99); Halliday et al. 2001 (H+01); Peng et al. 2004 (P+04b); Bedregal et al. 2006 (B+06); Douglas et al. 2007 (D+07); Napolitano et al. 2009 (N+09); Coccato et al. 2009 (C+09); Proctor et al. 2009 (P+09); Weijmans et al. 2009 (W+09a); Williams et al. 2009 (W+09b); Forestell & Gebhardt 2010 (FG10); Spolaor et al. 2010 (S+10); Arnold et al. 2011 (A+11); McNeil-Moylan et al. 2012 (M+12). Other photometric references are: Mahdavi et al. 2005 (M+05).

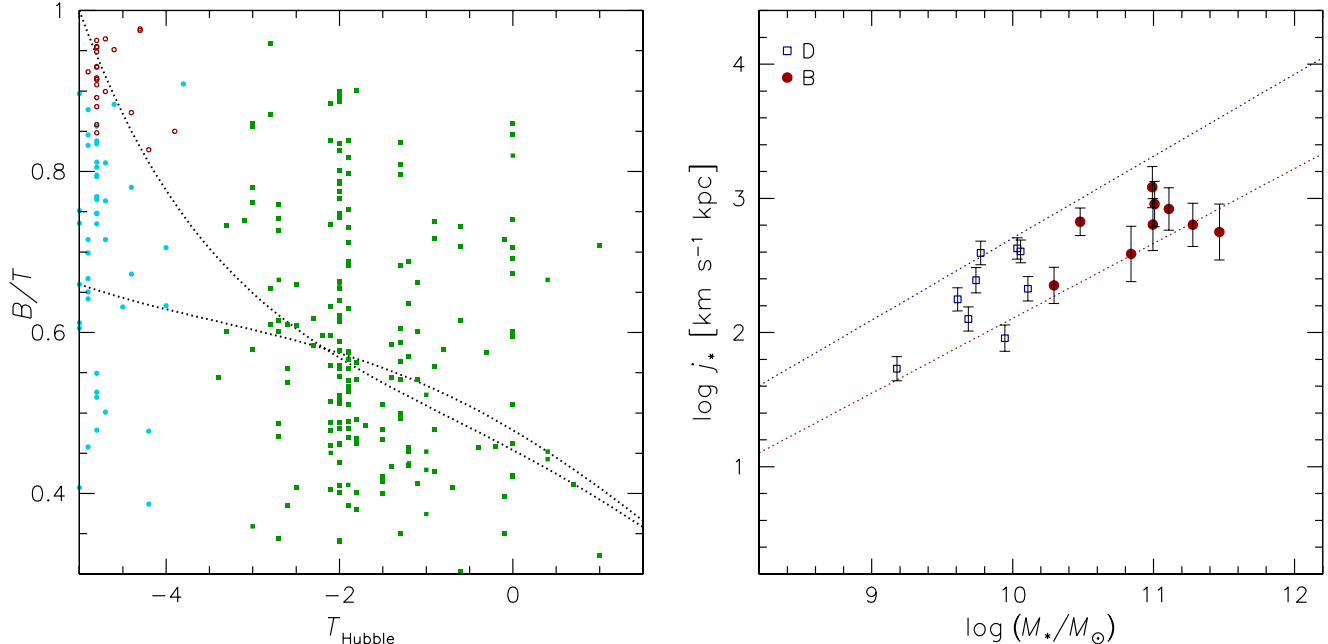


FIG. 34.— Bulge-fraction vs. morphological type for early-type galaxies (*left panel*), and specific angular momentum vs. stellar mass for the disk and bulge components of disky ellipticals (*right panel*). On the left, dotted curves show two alternative observational trends from Simien & de Vaucouleurs (1986). The points show data from ATLAS^{3D} galaxies, using Equation (D1) to estimate B/T with $C' = 1.35$. The symbol types are as in Figure 33. The dotted lines at right show the best-fit relations for spiral disks and ellipticals from the right-hand panel of Figure 14.

APPENDIX D: DECOMPOSING EARLY-TYPE GALAXIES

In Section 5.2, we sought to understand the j_*-M_* trends for spiral galaxies by considering their bulge and disk components separately. Many early-type galaxies (both lenticulars and fast-rotating ellipticals) are also thought to consist of such subcomponents, but the decompositions tend to be more difficult. Here we develop a novel method to estimate the bulge fraction, $f_b = B/T$, in order to study correlations involving this parameter, while we also analyze a small set of ellipticals with decompositions from the literature.

First, we suppose for simplicity that the relative dominance of rotation observed in an early-type galaxy indicates the disk fraction, i.e., the bulge is assumed to be non-rotating, with all of the observed rotation attributable to the disk. This disk is assumed to rotate at the circular velocity v_c , which we relate to the stellar rotation velocity and velocity dispersion, v and σ , by $v_c \simeq [v^2 + 2\sigma^2]^{1/2}$. The observed rotation is then $v = C'(1 - f_b) \times v_c$, where the parameter C' accounts for projection and aperture effects (e.g., a central aperture probably encloses a larger disk fraction than the global value). After rearranging terms, we can solve for the bulge fraction based on the observed (v/σ) parameter:

$$f_b \simeq 1 - \frac{C'(v/\sigma)}{\left[2 + C'^2(v/\sigma)^2\right]^{1/2}} \quad (\text{D1})$$

Next, to estimate the numerical factor C' , we calibrate against the relation between morphology and bulge fraction derived from photometric data by Simien & de Vaucouleurs (1986). As shown in the left-hand panel of Figure 34, these authors derived two alternative relations with different extrapolations for the elliptical galaxies, and we select the version that extends to $B/T = 1$, i.e., with some ellipticals being truly disk-less. We then plot the ATLAS^{3D} data set, using their morphological types and $(v/\sigma)_e$ values, and estimating B/T using Equation (D1). Based on the lenticular galaxy data ($T_{\text{Hubble}} \sim -2$), we judge $C' \simeq 1.35$ to provide a reasonably good match; this is similar to our adopted model of $C_{\text{med}} = 1.21$ for these galaxies (Appendix A.3).²⁹ As in Appendix C, there is then an additional factor (of $1/2.4$ at $1 a_e$) to convert our (v/σ) observations to the ATLAS^{3D} values when those are not available. We estimate our final B/T values to be generally accurate at the $\sim \pm 0.2$ level.

Next we investigate the bulge and disk j_*-M_* trends for a small sample of elliptical galaxies, making use of the pioneering work of Scorza & Bender (1995), who carried out decompositions *including the kinematics of the bulge and disk subcomponents*. These authors reported j_* for the subcomponents, and concluded that while the surface brightnesses and scale-lengths of these disks were consistent with an extension of scaling relations for lenticular and

²⁹ Khochfar et al. (2011) adopted a similar convention for connecting early-type galaxy rotation with B/T but did not quantify a relation except to estimate $f_b \sim 0.85-0.9$ as the division between fast- and slow-rotators, based on semi-analytical modeling

of galaxy formation. This is consistent with our relation, since the slow/fast boundary is typically at $(v/\sigma)_e \sim 0.15$, which our relation translates to $f_b \sim 0.85$. On the other hand, the observational study of Laurikainen et al. (2011) does *not* support a strong correlation between $(v/\sigma)_e$ and B/T .

spiral galaxies, the same may not be true for the disk j_* values, with those of the ellipticals systematically lower than those of the disk galaxies. These data were further used by van den Bosch (1998) to support a scenario where disks in ellipticals are not related to spiral disks, but such conclusions neglected the mass dependence naturally expected for j_* .

Revisiting the Scorza & Bender (1995) data set, we take their size and rotation decompositions as given, and update the distances, stellar masses, and j_* calculations according to our current methodology. From a few galaxies in common, we find that these j_* values tend to be higher than what we would derive from scratch (e.g., because of decreasing rotation velocity outside the central regions). Nevertheless, we plot the results in Figure 34 (right-hand panel), comparing them to the j_*-M_* relations that we have found for spiral disks, and for ellipticals overall (which we recall is roughly similar to the trend for the massive bulges of spirals).

There does appear to be a systematic separation between the relations for the bulges and disks of these ellipticals, but not as large as we would expect based on the results for spirals. Given the uncertainties in these decompositions, we conclude that it is not yet clear whether or not the disk and bulge subcomponents of ellipticals follow the same j_*-M_* relations as in spirals. If they do, it would be natural to expect the total trend for ellipticals to be offset to slightly higher j_* values from the bulge trend (owing to the disk contributions), which from inspection of Figure 14 (right-hand panel) may indeed be true.